Wave Patterns in Networks of Coupled Oscillators

by

Yujie Ding

B.S. Mathematics, Southern University of Science and Technology, 2017

Submitted to the Graduate Faculty of

the Dietrich School of Arts and Sciences in partial fulfillment

of the requirements for the degree of

Doctor of Philosophy

University of Pittsburgh

2022

UNIVERSITY OF PITTSBURGH

DIETRICH SCHOOL OF ARTS AND SCIENCES

This dissertation was presented

by

Yujie Ding

It was defended on

October 17, 2022

and approved by

Bard Ermentrout, Distinguished University Professor

Jonathan Rubin, Professor and Department Chair

David Swigon, Associate Professor

Andrew Mugler, Associate Professor

Wave Patterns in Networks of Coupled Oscillators

Yujie Ding, PhD

University of Pittsburgh, 2022

Recent advances in brain recording techniques have demonstrated that neuronal oscillations are not always synchronized, but rather, organized into spatio-temporal patterns such as traveling and rotating waves. This thesis is an investigation of wave patterns in a network of identically coupled phase oscillators. We demonstrate the existence and stability of traveling waves and rotating waves on a variety of domains with a combination of analytical and numerical methods, and also discuss the relationships between various types of coupling.

In Chapter 1, we bring in the concepts of neural oscillators as well as the phase reduction method.

In Chapter 2, we analyze a one-dimensional network of phase oscillators that are non-locally coupled via the phase response curve (PRC) and the Dirac delta function. The existence of waves is proven and the dispersion relation is computed. Using the theory of distributions enables us to write and solve an associated stability problem.

We next extend this model from one-dimensional ring domains to two-dimensional annulus domains, and derive an integro-differential equation of the form commonly used to model two-dimensional neural fields. In Chapter 3, under the “weaker” weakly coupling setting, this network can be averaged into a diffusive phase coupling model.

In Chapter 4, we examine the existence, stability, and form of rigid rotating waves in a non-locally coupled phase model on the annulus. We show that as the hole in the annulus decreases, the waves lose stability. Through numerical simulations, we suggest that the bifurcation that occurs with the shrinking hole is a saddle-node infinite cycle and gives rise to so-called spiral chimeras.

In Chapter 5, rotating waves in a system of locally coupled phase oscillators on a $N \times N$ lattice grid are studied. We show that as $N \to \infty$ that the dynamics can be understood by a Bessel equation on an annulus with inner radius proportional to $1/N$. We find similar rotating wave patterns through simulations from both square lattice and hexagonal lattice.

A general discussion and an outlook of future work are provided in the final Chapter 6.

Table of Contents

List of Tables

List of Figures

Preface

I would like to thank to my PhD advisor, Prof. Bard Ermentrout, for supporting me during these past five years. Bard is someone you will instantly love and never forget once you meet him. He is energetic and enthusiastic about math, birds and dogs. He likes talking with students, let his door open thus his office has the biggest "passenger traffic" in the department. I really appreciated his scientific advice and knowledge and many insightful discussions and suggestions. This thesis would not be possible without his expertise.

Besides my advisor, I would also like to thank the rest of my thesis committee: Prof. Andrew Mugler, Prof. Jonathan Rubin and Prof. David Swigon. I took the ordinary differential equation course with Prof. Swigon and Prof. Rubin; and it was the best and the hardest course I ever had in graduate school. They challenged my mathematical skills, and helped me gain a closer understanding of scientific concepts in mathematics. At that time, Prof. Rubin's every single office hour was taken up by me, while I still got the most patient explanations for homework questions.

Also, I extend my thanks to all of the faculty, staff, postdocs and fellow graduate students in the Department of Mathematics for their kind support during my PhD study. Many thanks to Math Biology group, we had a lot of great talks, insightful conversations (and pizzas) in the seminar.

Last but not least, I would like to thank my parents for always being there for me.

1.0 Introduction

1.1 Background

The human brain contains over 100 billion neurons. These neurons are wired together, generate and propagate information to lead to all kinds of behavior for everyday tasks. Neuroscientists have spent decades conducting experiments at different levels to understand the mechanism of brain functions. Large-scale neural recording methods now allow us to observe large populations of identified single neurons simultaneously[60]. Their neural activities are measured as electrical waves from electroencephalogram (EEG), electrocorticogram (ECoG), and local field potential (LFP).

In order to understand the experimentally observed data, many mathematical approaches and tools are developed to model biological neural networks. Spatial and temporal features of neural activities are considered and interpreted by differential equations from the point of view of dynamical system theory. Now there are numerous models at different scales ranging from single neuron activities to collective dynamics among neural populations.

However, it is still challenging to build biologically realistic and computationally tractable models. Especially for a biological neural network, one must take into account the types of neurons and synapses in the system, as well as the structural topology. Synapses are classified into excitatory or inhibitory depending on the mechanism that the neuron uses for the transmission of the signal, and the synaptic transmission can be either electrical or chemical. The coupled system may be evolved in a high-dimensional variable space, and therefore hard to simulate and get any analytical results. Hence, a common approach is to reduce systems of coupled oscillatory neurons to simple phase models through the phase reduction method.

In this study, we develop coupled phase models and investigate the induced spatial-temporal patterns such as traveling waves and rotating waves, thus providing new insights into understanding the working mechanisms of nervous systems.

1.2 Phase Reduction

Many biological systems with periodic behaviors are usually modeled in terms of oscillators. Neurons act as oscillators in the way that their activities have been characterized by amplitude, frequency, and shape of action potentials.

For intrinsic mechanisms within individual neurons, this can be done using a single equation or a system of differential equations. The simplest one-dimensional system is the Integrate-and-fire model assuming that the spike process is governed by a voltage threshold. Whereas Hodgkin-Huxley model explained the formation and propagation of action potentials in the squid giant axon with four differential equations including channel gating variables. Ultimately, scientists try to understand the operations of the nervous system and the functions of the human brain. Instead of modeling a single neuron, we need to work with models of coupled oscillators to explain responses from the neuronal population. When more neurons get involved, these models are usually difficult to analyze and are computationally expensive in numerical implementations.

Phase-reduction techniques of complex oscillatory systems can be applied to reduce a multi-dimensional variable to a one-dimensional phase variable. To reduce a system with amplitude dynamics, it is usually assumed that there exists a stable limit cycle where any perturbed oscillator will eventually go back. Neural populations in the same area of the brain have similar shapes and frequency of action potentials, moreover, interactions among oscillators within the same group only change their spiking timing which causes the phase lag or phase difference. Based on the approach of isochron and phase coordinate, a general coupled oscillator system is transformed into an autonomous system in which mathematicians are able to track the phase portrait and analyze properties like stability and bifurcation.

1.2.1 Single oscillator

We start with a simpler system with one single oscillator to illustrate the phase reduction theory from [43].

A dynamical system for one single oscillator can be described by an ordinary differential equation

$$\frac{d\mathbf{X}}{dt} = F(\mathbf{X}), \tag{1}$$

where $\mathbf{X} = \mathbf{X}(t) \in M \subset \mathbb{R}^n$ is a n-dimensional states vector. Consider a small perturbation being added to the system Equation (1), then we can write the dynamics of $\mathbf{X}$ as

$$\frac{d\mathbf{X}}{dt} = F(\mathbf{X}) + \epsilon G(t), \tag{2}$$

where G is an external perturbation, and it is scaled by a small parameter ϵ $(0 < \epsilon \ll 1)$.

Let $\mathbf{X}(t)$ be linearly stable T-periodic solution that describes the oscillatory dynamics of the unperturbed system Equation (1), i.e. $\mathbf{X}(t+T) = \mathbf{X}(t)$. One can associate the vector field Equation (2) with a **flow** $\Phi(t;\mathbf{X})$ starting at some initial state $\mathbf{X}_0 \in M$, then $\mathbf{X}(t) = \Phi(t;\mathbf{X}_0)$. The stable, T-periodic solution of an oscillator in the unperturbed system follows a trajectory along a close periodic orbit $\Lambda \in M$, which is the limit cycle of the oscillator. When the limit cycle is asymptotically stable, it attracts all solutions with initial conditions in a small neighborhood of Λ, which is the limit cycle's **basin of attraction**, or

$$\mathcal{B}(\Lambda) := \{\mathbf{X}_0 \in M | \lim_{t\to\infty} \Phi(t;\mathbf{X}_0) \in \Lambda\}.$$

Since the limit cycle Λ is homeomorphic to the unit cycle, it can be parametrized by a **phase variable** $\Theta(\mathbf{X}) := u(t)$, where $\Theta : \Lambda \to \mathbb{S}^1$ is a **phase map** and $t \in [0, T)$. The phase grows monotonically with time, using the chain rule,

$$\frac{d}{dt}\Theta = \nabla\Theta(\mathbf{X}(t)) \cdot \dot{\mathbf{X}}(t) = \nabla\Theta(\mathbf{X}(t)) \cdot F(\mathbf{X}(t)) = 1.$$

This concept of phase can be extended to the basin of attraction $\mathcal{B}$. When the perturbation term is considered (Equation (2)), a state variable $\mathbf{X}_p$ is kicked off from the limit cycle Λ but staying close to it. Assuming $\mathbf{X}_p \in \mathcal{B}(\Lambda)$, there exists a unique phase θ such that $\lim_{t\to\infty} |\Phi(t;\mathbf{X}_p) - u(t+\theta)| = 0$. Without loss of generality, we consider that point on the limit cycle as a reference point of phase zero, and define the **asymptotic phase** as $\Theta(\mathbf{X}_p) := \theta$. The set of points which are mapped to the same phase variable θ is called an **isochron** of the limit cycle. Isochrons are locally invariant, and the existence of isochrons is proved in [30].

If $\mathbf{X}_p$ is a solution to the weakly perturbed system Equation (2), the phase along this orbit Λ evolves according to

$$\begin{aligned} \frac{d}{dt}\Theta(\mathbf{X}_p(t)) &= \nabla\Theta(\mathbf{X}_p(t)) \cdot F(\mathbf{X}_p(t)) + \epsilon\nabla\Theta(\mathbf{X}_p(t)) \cdot G(t), \\ &= 1 + \epsilon\nabla\Theta(\mathbf{X}_p(t)) \cdot G(t), \end{aligned} \tag{3}$$

This is an exact equation, but we do not know about $\mathbf{X}_p(t)$.

However, the gradient of asymptotic phase map Θ evaluated on the limit cycle Λ can serve to determine the phase response from weak perturbation, which is defined as an **adjoint**:

$$Z(\theta) = \nabla(\Theta(\mathbf{X}))\big|_{\mathbf{X}=u(\theta)}.$$

Since $Z(\theta) \approx \nabla\Theta(\mathbf{X}_p(t))$, Equation (3) is closed to the following autonomous system if $G(t)$ is T-periodic,

$$\frac{d\theta}{dt} = 1 + \epsilon Z(\theta) \cdot G(t). \tag{4}$$

With one change of variable that $\theta = t + \psi$, Equation (4) becomes

$$\frac{d\psi}{dt} = \epsilon Z(t+\psi) \cdot G(t). \tag{5}$$

We integrate Equation (5) and find by **averaging** that:

$$\frac{d\psi}{dt} = \frac{1}{T}\int_0^T \epsilon Z(t+\psi) \cdot G(t)\ dt := \epsilon H(\psi), \tag{6}$$

where the function H is called the **phase response curve (PRC)**.

1.3 Coupled Oscillators

Using the phase reduction theory of single oscillators as a building block, networks of coupled oscillators can often be reduced (e.g. when there is weak coupling between them) to similar networks of phase models [22, 65, 5] which are usually much easier to analyze. In this section, we review several classic coupled oscillator models, and discuss different types of coupling. Depending on connectivity among oscillator population, there are global (all-to-all) coupling, local (nearest-neighbor) coupling and non-local (neither all-to-all nor nearest-neighbor) coupling.

Coupling functions describing the underlying interactions found in nature are mostly nonlinear. We discuss how phase reduction is applied to a general nonlinear network in the limit of a large number of coupled oscillators. The resulting phase model can be defined discretely on any abstract domain with coupled differential equations or continuously as an integro-differential equation if a continuous spatial domain is specified.

It is modeled in two slightly different ways providing how the interaction occurs. Coupling occurs continuously due to interactions among oscillators is called **phase-difference coupling** or diffusive coupling (many studies also use this term for local coupling therefore the previous one is preferred to avoid any confusion). A more intuitive way to model neural networks is via pulse interaction where an individual oscillator gets a stimulus at a discrete time instance. The **pulse coupling** models are usually equipped with Dirac delta type influence functions which represent input spike timing. These two models are closely related in systems of weakly coupled oscillators, and the phase-difference coupling can be derived from pulse coupling with the averaging method applied.

1.3.1 General coupling

We can derive phase equations for a system of a chain of N limit-cycle oscillators weakly coupled in a network as:

$$\frac{d\mathbf{X}_j(t)}{dt} = F(\mathbf{X}_j) + \epsilon c_j F(\mathbf{X}_j) + \epsilon \sum_{k=1}^{N} G_{jk}(\mathbf{X}_j, \mathbf{X}_k), \quad j = 1 \ldots N, \tag{7}$$

where $\mathbf{X}_j$ is the state vector of the oscillator j, $F(\mathbf{X}_j)$ is the unperturbed dynamics of the oscillator, $G_{jk}(\mathbf{X}_j, \mathbf{X}_k)$ is the input from oscillator k to oscillator j, c_j is a constant, and ϵ is characterized as the coupling strength, which is a small parameter under weak coupling assumption.

For a general network without perturbation, there is a stable limit cycle to $\dot{\mathbf{X}} = F(\mathbf{X})$. Suppose the solution $\mathbf{X}$ lies on the limit cycle has period T and natural frequency $\omega = 1/T$. Define the phase map $\Theta(\mathbf{X})$ as previous section, state variable $\mathbf{X}$ is projected to the limit cycle, which gives the phase of the oscillator j, that is $\theta_j(t) = \Theta(\mathbf{X}_j) \in [0, 2\pi)$. The intrinsic frequency of oscillator j without perturbation is $d\Theta(\mathbf{X}_j)/dt = 1$. Similar to the derivation of Equation (4), the phase equation of oscillator j in the perturbed system Equation (7) is written as

$$\begin{aligned} \frac{d}{dt}\theta_j &= 1 + \epsilon Z(\theta_j) \cdot \left[c_j F(\theta_j) + \sum_{k=1}^{N} G_{jk}(\theta_j, \theta_k) \right], \\ &= (1 + \epsilon c_j) + \epsilon Z(\theta_j) \cdot \sum_{k=1}^{N} G_{jk}(\theta_j, \theta_k), \end{aligned} \tag{8}$$

where $Z(\theta_j)$ is the phase response function (PRC) of the limit cycle.

This kind of network was first introduced by Winfree [71] to understand biological rhythms from experimental observations including neurons, fireflies, and circadian rhythms. Those population dynamics were modeled by autonomous differential equations with separate periods and non-linear coupling. The **Winfree model** is described as

$$\frac{d}{dt}\theta_j = \omega_j + \frac{K}{N}\Delta(\theta_j) \sum_{k=1}^{N} R(\theta_k), \tag{9}$$

where oscillators are globally coupled, subject to biologically realistic PRC Δ and pulsatile interaction function R. Parameter $K > 0$ is the coupling strength which is not necessary small. Phase variable θ_j is varying from 0 to 2π. The function R specifies the form of the pulses, and satisfies the following properties: (1) R is unimodal and symmetric around $\theta = 0$; (2) R vanishes at $\theta = \pi$; (3) R is normalized on one period: $\int_0^{2\pi} R(\theta)\, d\theta = 1$.

Under the weak coupling assumption, if the heterogeneity of the oscillators is sufficiently small, the averaging method can be performed to further reduce Equation (8). Let us introduce a new relative phase variable $\phi_j(t) = \theta_j(t) - t$ by subtracting the unperturbed increasing component t from the individual phase $\theta_j(t)$. Then Equation (8) is written as,

$$\frac{d}{dt}\phi_j(t) = \epsilon c_j + \epsilon Z(\phi_j + t) \cdot \sum_{k=1}^{N} G_{jk}(\phi_j + t, \phi_k + t). \tag{10}$$

Notice that functions on the right hand sides are T-periodic, we have a system of the form

$$y' = \epsilon M(y, t), \quad 0 < \epsilon \ll 1, \tag{11}$$

where M is T-periodic. By averaging the fast oscillation given by M over one period of oscillation, Equation (11) is approximated a system close to y, which is

$$\bar{y}' = \epsilon \frac{1}{T} \int_0^T M(\bar{y}, t) dt. \tag{12}$$

The averaging method is applied to Equation (10), and we obtain a dynamical system involved with the phase differences between two coupled oscillators,

$$\frac{d}{dt}\phi_j(t) = \epsilon c_j + \epsilon \sum_{k=1}^{N} H_{jk}(\phi_j - \phi_k), \quad j = 1 \ldots N, \tag{13}$$

where

$$H_{jk}(\phi) = \frac{1}{T} \int_0^T Z(t) \cdot G_{jk}(t, t + \phi) dt, \tag{14}$$

is called the phase coupling function, which represents the effect of oscillator k on oscillator j over one period of the limit cycle oscillation.

Kuramoto took this path and simplied the Winfree model. He assumed that oscillators are nearly identical and very weakly coupled. In that situation, the averaging approximation is valid, and the rate of change of an oscillator's phase depends only on the difference between its phase and those of all oscillators that influence it. The **Kuramoto model** consists of N limit-cycle oscillators, and the interactions depend sinusoidally on the phase difference between each pair of objects:

$$\frac{d}{dt}\theta_j(t) = \omega_j + \frac{K}{N} \sum_{k=1}^{N} \sin(\theta_k - \theta_j), \quad j = 1 \ldots N, \tag{15}$$

where K is the coupling strength.

Kuramoto also introduced the order parameter and derived critical coupling strength corresponding to the transition to synchrony solution by mean-field analysis. It is one of the most fundamental models showing phase synchronization and has found widespread applications in neuroscience[5].

1.3.2 All-to-all coupling and local coupling

Kuramoto model was originally considered with all-to-all (global) coupling, while it can be generalized to any connectivity structure. Variations of the Kuramoto model have been used to represent systems with alternative topologies, such as lattice[62] and regular graphs[15]. When oscillators are equipped with networks of different structures, instead of all-to-all (globally) coupling, a lot of progress has been made in the system of locally coupling or nearest neighbor coupling. For a d-dimensional lattice, a locally coupled model where each oscillator interacts with its nearest neighbors only can be written as

$$\frac{d}{dt}\theta_j(t) = \omega_j + K\sum_{k\sim j}\sin(\theta_k - \theta_j), \tag{16}$$

where $k \sim j$ represents the nearest neighbor. In the presence of local coupling, the existence of traveling waves in one dimension[58], target and spiral waves in two dimension[56, 48] can be realized, which is induced by the boundary conditions. In the spatially continuous case this generally involves systems of reaction diffusion equations [42].

1.3.3 Non-local coupling

Non-local coupling lies in the middle of the spectrum of coupling schemes in terms of connectivity, which describes interactions with distant oscillators. By introducing the coupling matrix W_{jk} to the corresponding coupling function G_{jk}, we can write $G_{jk} = W_{jk}G(\theta_j, \theta_k)$ and also $H_{jk} = W_{jk}H$ according to Equation (14), so that each entry accounting for the interaction between oscillator j and k is assigned a different weight. In the continuum limit, a non-locally coupled system can be rewritten as,

$$\frac{d}{dt}u(x,t) = \omega(x) + \int_A W(|x-y|)H(u(y,t) - u(x,t))\ dy. \tag{17}$$

where $u(x,t)$ is the phase of oscillator at spatial location x at time t, A is a one-dimension or two-dimension domain. It is an extension of the original all-to-all coupled Kuramoto model, the connection strength between any two oscillators is indicated by the coupling kernel $W(|x|)$. One commonly used function for non-negative W is the Gaussian kernel when the interaction between oscillators decays with their distance, $W(|x|) = e^{-|x|^2}$. It is a symmetric kernel, normalized to have the unit integral. One can also think of it as Greens' function associated with the differential operator $(1 - \nabla^2)$, depending on the space difference, therefore the corresponding coupling is reduced to coupling through a diffusive agent. The interaction function H can represent not only sinusoidal interactions but also more generalized interactions, i.e. $H(u(y) - u(x)) = \sin(u(y) - u(x) + d)$, which is known as the Sakaguchi–Kuramoto model, and d is a phase-lag parameter.

In addition to the **phase-difference coupling** that was previously explored in Kuramoto-like models, **pulse coupling** is another type of nonlocal coupling in a population of oscillators. If the interaction is the product of the phase response function $\Delta(u)$ and the influence function $R(u)$, the spatially continuous version of Equation (8) is defined as an integral differential equation,

$$\frac{d}{dt}u(x,t) = \omega + \Delta(u(x)) \int_A W(|x-y|)R(u(y))\ dy. \tag{18}$$

which is a continuum limit of the non-locally coupled Winfree model. If the influence function is a Dirac function $R(u) = \delta(u)$, oscillator x is assumed to receive a signal from oscillator y which occurs precisely at the moment of resetting of oscillator y. Winfree oscillators can accurately model pulsatile interactions thus are more realistic than Kuramoto oscillators in biological systems.

Non-local phase models have been studied in the past, mainly in one-dimensional domains such as the infinite line [14], and in the study of so-called *chimeras* [2]. Our study starts with a non-local pulse coupling model (Equation (18)) on one-dimensional ring domains. We find the results can be extended to two-dimensional space. However, in order to get more analytical results on annulus domains, we have to reduce the pulse coupling model to a phase-difference coupling model (Equation (17)) in the weak coupling limit. We also show the relationship between the two systems by implementing simulations with a pulse-like coupling function in Chapter 3.

1.4 Waves

In this section, we focus on the spatio-temporal patterns that emerged from a system of coupled oscillators. These patterns can, in their simplest form, be traveling waves of various shapes (including plane, radial, and spiral waves). Many of them have been discovered extensively in biological neural networks at multiple spatial scales [60, 52, 28, 24, 67, 59, 36, 37]. Because so much of the experimental analysis of spatio-temporal patterns in the brain is based on the phase analysis of the filtered local field potential (LFP), it is natural to regard the neural activity in these regions to be intrinsically oscillatory allowing phase representation of the system. For example, a recent paper [73] used a simple coupled oscillator model to explain plane waves in human LFP. In typical experiments, the LFP is filtered and a Hilbert transform is applied to extract the local phase whereby a spatio-temporal map of the phases is displayed.

We start our investigation with the traveling wave patterns from non-locally coupled oscillators on a ring model of one-dimensional spatial domain with a periodic boundary condition. It can be extended to a two-dimensional annulus model considered as many concentric rings of increasing radius. A spiral wave is defined through a path from the inside ring to the outside ring with fixed angular speed on the annulus. The annulus domain can be utilized to reduce the dimensionality of the equation and make it mathematically tractable.

Consider a chain of N non-locally coupled oscillators on a periodic domain, equations that govern the dynamics of the phases of networks of oscillators are:

$$\frac{d\theta_j}{dt} = \omega_j + \sum_{k=1}^{N} W_{jk} H(\theta_j - \theta_k), \qquad j = 1 \dots N, \tag{19}$$

where $\theta_j \in S^1$, a unit circle, ω_j is the natural (uncoupled) frequency, and W_{jk} is the coupling strength between oscillator j and k.

The ring model is a continuous limit of Equation (19) in the following form:

$$\frac{du(\mathbf{x})}{dt} = \omega(x) + \int_0^L W(|x-y|)H(u(x)-u(y))\ dy, \tag{20}$$

where L is the length of the ring, $x \in [0, L)$ indicates each oscillator's location.

The best way to extend Equation (20) to an annulus model is to let $\mathbf{x} \in \mathbb{R}^2$, and write the integral in a polar coordinate as an iterated integral in the following manner:

$$\frac{du(\mathbf{x})}{dt} = \omega(\mathbf{x}) + \int_0^{2\pi}\int_a^b W(|\mathbf{x}-\mathbf{x}'|)H(u(\mathbf{x})-u(\mathbf{x}'))\ d\mathbf{x}', \tag{21}$$

where a, and b are the inner radius and outer radius of the annulus domain, respectively.

1.4.1 Synchronization and phase-locking

Synchronization in the activity of neural populations is one of the most important brain mechanisms including memory keeping, cognitive processing, and information transmission. When neurons begin to act in synchrony, their action potentials (spikes) are aligned perfectly in time.

If the interaction function H in Equation (19) satisfies $H(0) = 0$, therefore synaptic coupling dose not affect the oscillatory dynamics when there is no phase difference. The phase model with identical intrinsic frequency ω always has a stable synchronous state, given by

$$\theta_j(t) = \omega t, \quad j = 1 \ldots N, \tag{22}$$

which is called a **synchrony**. Thus individual oscillator phase θ_j increases with a constant collective frequency ω to show the synchronous activity.

Even if the oscillators have non-identical intrinsic frequencies ω_j, and they are started non-synchronously, coherence or synchrony may arise with weak interactions. Kuramoto model as a simplified model showed the mathematic perspective to understand this synchronization phenomenon. The model can be solved exactly as $N \to \infty$ using transformation. Define a complex order parameters as following

$$re^{i\varphi} = \frac{1}{N}\sum_{k=1}^{N} e^{i\theta_k}. \tag{23}$$

where r represents the phase-coherence of the population of oscillators and φ indicates the average phase. The Kuramoto model is transformed to

$$\dot{\theta}_j = \omega_j + Kr\sin(\varphi - \theta_j), \quad j = 1 \dots N. \tag{24}$$

One can set average phase $\varphi = 0$ by moving the coordinate, then the ode is further reduced to:

$$\dot{\theta}_j = \omega_j - Kr\sin(\theta_j), \quad j = 1 \dots N. \tag{25}$$

Oscillators are no longer coupled to each other after transformation. The behavior of individual oscillator is governed by the intrinsic frequency ω_j, the product of coupling strength K and phase-coherence r. When $\omega_j > Kr$, the oscillators will converge to a fixed point satisfying $\omega_j = Kr := \omega$. There is a fully synchronized **phase-locked** solution,

$$\theta_j = \omega t + \phi_j. \tag{26}$$

All the oscillators share the same common frequency ω, and their phase differences are fixed.

1.4.2 Traveling waves

Multi-electrode arrays and imaging methods have established that what was once believed to be synchronous activity actually takes the form of propagating phase-waves [73, 33, 59]. Figure 1 shows the evidence for traveling waves in the human neocortex.

Traveling waves are now known to be a ubiquitous property of rhythmic neural networks [52] in the cerebral cortex. They are commonly observed in recordings of the cerebral cortex and are believed to organize behavior across different areas of the brain [24, 68, 67, 52, 59]. Instead of precise synchrony, there is a relative timing of oscillatory activity which changes constantly.

Consider Equation (19) with identical intrinsic frequency ω, let $\phi_j = \theta_j - \omega t$ as the relative phase, the phase-locked solution is a fixed points in the system,

$$\frac{d\phi_j}{dt} = \epsilon \sum_{k=1}^{N} W_{jk} H(\phi_j - \phi_k) \qquad j = 1 \dots N. \tag{27}$$

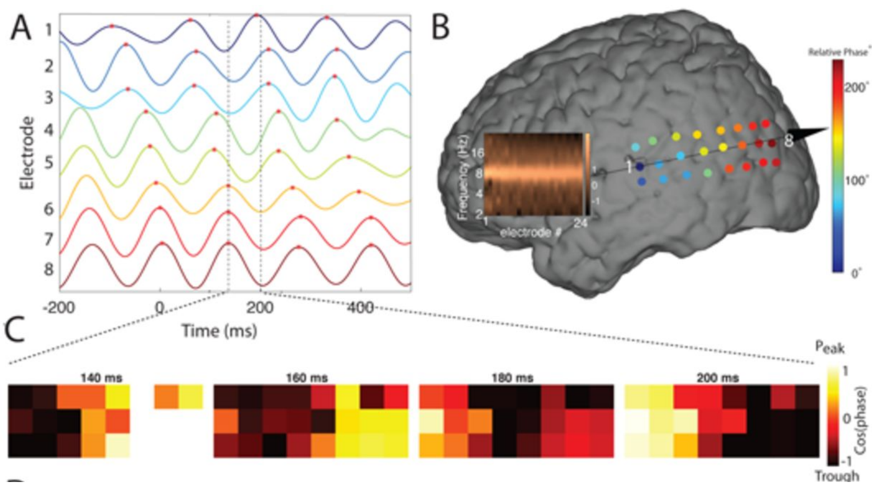

Figure 1: Traveling wave in one trial on electrodes in human cortex ordered from anterior (top) to posterior (bottom). Panel C is the temporal evolution of the phase pattern for the trial from Panels A & B. Adapted from [73].

This phase-locked solution has constant phase differences and a non-vanishing mean velocity between the oscillators, which in a dynamical system corresponding to a traveling wave.

Similarly, oscillators in one-dimensional domain can be described by a function of time and space, $u(x,t) = F(ct - x)$, where $F(\xi)$ is a periodic function of a single parameter $\xi = ct - x$, that describes the shape of the wave. This is a plane wave that travels along the positive direction of x with velocity c, and the parameter $\xi = ct - x$ is called the moving coordinate.

1.4.3 Rotating waves

Waves in two-dimensional space take various forms, including target waves, planar waves, and rotating waves. Among the types of patterns seen in both normal and pharmacologically altered neural tissues are rotating or spiral waves (Figure 2). The earliest recordings of rotating waves were found in the electrocorticogram (ECoG) of rabbit occipital lobe treated with penicillin [57]. More recently [36, 63, 37] studied spiral waves in a tangential slice of rat cortex where the inhibition was blocked. In the modeling of this phenomena [36], the authors

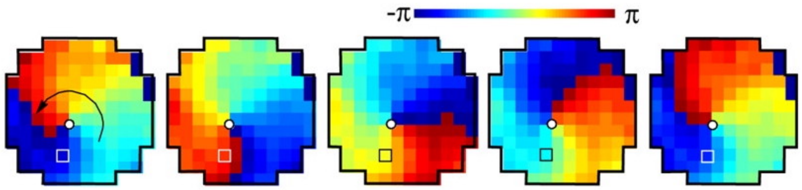

Figure 2: Rotating spiral wave patterns seen in neural tissue in a tangential disinhibited cortical slice from [36].

used Wilson-Cowan type equations and regarded the space-clamped system as an excitable medium. Muller et al [53] have recently reported that oscillatory sleep spindles in humans are organized into large-scale rotating waves. Rotating waves have also been reported in the motor cortex of monkeys [61] and the temporal cortex of marmosets [68].

Rotating waves have previously been found in discrete nearest neighbor coupled $N \times N$ arrays [55] and studied in the limit as $N \to \infty$ in [8, 9]. Since we are interested in the rotating waves in a continuum of non-local phase oscillators, we can take the advantage of the annulus domain and use its symmetry to reduce the dimensionality of the problem. N-armed rotating waves in polar coordinate in this case are defined as $u(\theta, r, t) = U(r, \xi) = \omega t + N\theta + f(r)$, where $\xi = \omega t + N\theta$ is the moving coordinate, $f(r)$ is a periodic function indicating phase difference along a ray of fixed angle.

Spiral Chimera Chimera is a mixture state of the regular rotating wave and the irregular behavior near the center of the spiral. Spiral waves in non-locally coupled oscillatory media were studied in [43, 66] where coupled Fitzhugh-Nagumo oscillators were simulated in a two-dimensional domain. The authors found that for strong coupling rigid, rotating waves occurred. However, for weaker coupling, the "core" of the spiral became phase-randomized so that rigid rotating waves no longer existed. This phenomenon was called a *chimera* by [2] and led to a large number of studies, particularly of phase models in two spatial dimensions. Laing [46] used the Ott-Antonsen reduction to numerically continue spiral waves on a sphere. Notably, the underlying local dynamics are two-dimensional and he finds solutions like [43] representing rigid rotating waves. By varying the spatial coupling radius and a parameter related to the interaction between local oscillators, he shows that the spiral wave loses stability through a Hopf bifurcation which leads eventually to the phase randomized core; the defining feature of spiral chimeras. Omel'chenko [54] presents a comprehensive review of chimeras and includes a short section on spiral chimeras.

2.0 Pulse Coupling on Ring

2.1 Model

We suppose that there is a one population network of nearly identical coupled neurons driven so that in absence of coupling they are firing rhythmically. Such networks of conductance-based neurons [22] are generally coupled by chemical synapses and the voltage of neuron i satisfies the differential equation:

$$C_m \frac{dV_i}{dt} = I_i - I_{ion}(V_i, \ldots) + \sum_{j=1}^{N} g_{ij} s_j (E - V_i), \quad , i = 1, \ldots, N,$$

where I_i is the injected current, $I_{ion}(V_i, \ldots)$ are the active currents that allow the neurons to fire, and g_{ij} are the synaptic conductances that specify the connectivity between neurons. The variables $s_j(t)$ are the synapses and may satisfy differential equations themselves, but are dependent *only on* $V_i(t)$. In absence of coupling ($g_{ij} = 0$), if the neurons fire repetitively, then, we can regard each neuron as an asymptotically stable limit cycle oscillator.

Let X_i denote the vector of the voltage, conductance, and synapse variables for each neuron. Then we can write the dynamics of X_i as

$$\frac{dX_i}{dt} = F(X_i) + \sum_{j=1}^{N} G_{ij}(X_i, X_j), \quad j = 1, \ldots, N. \tag{28}$$

The $s_i(t) = \sum_{j=1}^{N} G_{ij}(X_i, X_j)$ is the weakly coupled synaptic input. The unperturbed system $\dot{X}_i = F(X_i)$ has a stable limit cycle where X_i can be projected to a periodic phase variable $u_i \in \mathbf{S}^1$. Now the dynamical system Equation (28) is transformed into a phase model

$$\frac{du_i}{dt} = \omega_i + \Delta(u_i) \sum_{j=1}^{N} G_{ij}(u_i, u_j), \tag{29}$$

where ω_i is the natural frequency of oscillator i, $\Delta(u_i)$ is the iPRC.

Many people have studied variations of Equation (29) in various geometries and limits (such as $N \to \infty$). In particular, with pulse coupling, $G_{ij}(u_i, u_j) = \sum_{j=1}^{N} k_{ij} R(u_j)$ [71], where k_{ij} are the coupling strengths and we have:

$$\frac{du_i}{dt} = \omega_i + \Delta(u_i) \sum_j k_{ij} R(u_j) \quad i = 1, \ldots, N. \tag{30}$$

Dror et al sought traveling wave solutions to Equation (30) in a nearest neighbor ring of oscillators with identical frequencies [18]. Goel and Ermentrout analyzed the stability of waves for Equation (30) for nearest-neighbor coupling and $R(u) = \delta(u)$ [29]. Much more has been done in the case where $k_{ij} = K/N$ and $N \to \infty$, for example, Ariaratnam and Strogatz [4] determined the complete phase diagram for $R(u) = 1 + \cos u$ and $\Delta(u) = -\sin u$ whereas Luke et al [50] studied the theta model where $\Delta(u) = 1 + \cos u$. These authors all take advantage of the special form of the equations to significantly reduce the dimensionality of the problem [7].

We suppose that the oscillators are arranged uniformly on a ring of circumference, L, the frequencies, ω_j are identical (with $\omega_j = 1$, without loss of generality) and that k_{ij} depends only on the distance (modulo L) on the ring. We let $\Delta x = L/N$ and then take the formal limit as $N \to \infty$ and obtain:

$$\frac{\partial u}{\partial t} = 1 + K \left[\int_0^L k_L(x-y) R(u(y,t)) \; dy \right] \Delta(u(x,t)) \tag{31}$$

where K is the overall coupling strength, $k_L(x)$ is an $L-$periodic even kernel that gives the interaction strength with distance. We assume that it has unit integral. Given a symmetric kernel function $k(x)$ with $\int_{\mathbf{R}} k(x) \; dx = 1$, we can construct a periodic kernel by setting

$$k_L(x) = \sum_{m=-\infty}^{\infty} k(x + mL).$$

Note that $k_L(x)$ is $L-$periodic and is also normalized when integrated over $[0, L]$. For example, if $k(x) = \exp(-|x|)/2$, then

$$k_L(x) = \frac{e^x + e^{L-x}}{2(e^L - 1)}. \tag{32}$$

If $k(x)$ is a Gaussian, then the corresponding kernel, $k_L(x)$ is often called a wrapped Gaussian.

Equation (31) was first studied by Ermentrout [26] in the weak coupling limit,

$$\frac{\partial u}{\partial t} = 1 + K \int_0^L k_L(x-y) H(u(y,t) - u(x,t))\, dy,$$

where $H(v) = (1/2\pi)\int_0^{2\pi} R(v-u)\Delta(u)du$ is the averaged interaction function. Here, we assume that the coupling is sufficiently weak that reduction to a phase-model is justified. However, we do not perform averaging which leads to *phase-difference* models as above and which are easier to analyze as there is an exact expression for the waves [26].

2.2 Traveling Waves and Dispersion Relation

2.2.1 Synchrony

Let us turn now to the analysis of Equation (31). We first lay out a few assumptions that make biological sense as well as make the analysis simpler. We assume that $u(x,t)$ lies on $[0, 2\pi)$ (with 0 and 2π identified) and that both Δ and R are $2\pi-$periodic functions. We assume that $R(u)$ is peaked at $u = 0$, the phase at which the neuron produces the coupling pulse, thus fixing the zero phase. We will assume no delays in communication from one neuron to the others. For many real neurons and models, the phase resetting curve, $\Delta(u)$ satisfies $\Delta(0) = 0$; that is, the neuron does not respond to any inputs when it is itself spiking. Thus, we will assume this condition as well. One solution to Equation (31) is the synchronous one, where $u(x,t) = U(t)$ independent of x. This satisfies:

$$\frac{dU}{dt} = 1 + KR(U)\Delta(U) \tag{33}$$

As long as the right-hand side of this equation is positive, there is a periodic solution, $U(t+T) = U(t) + 2\pi$ where the period

$$T = \int_0^{2\pi} \frac{du}{1 + KR(u)\Delta(u)}.$$

We can readily determine the stability of the synchronous state. We let

$$k_n = \int_0^L k_L(x) e^{-2\pi i n x/L}\, dx.$$

Plugging in $u(x,t) = U(t) + v(x,t)$, the linearization for Equation (31) around the synchronous solution is

$$\frac{\partial v}{\partial t} = K \int_0^L k_L(x-y) \left[R'(U(t))v(y,t)\Delta(U(t)) + R(U(t))\Delta'(U(t))v(x,t)\right] \; dy$$

where $\Delta'(U), R'(U)$ are the derivatives of $\Delta(u), R(u)$ with respect to u evaluated at $U(t)$. Let $v(x,t) = w_n(t)\exp(2\pi i n x/L)$. Then we have

$$\frac{dw_n}{dt} = K[k_n R'(U(t))\Delta(U(t)) + R(U(t))\Delta'(U(t))]w_n(t).$$

With $w_n(0) = 1$, we see that

$$w_n(T) = \exp\left(K \int_0^T [k_n R'(U(t))\Delta(U(t)) + R(U(t))\Delta'(U(t))] \; dt\right). \tag{34}$$

Synchrony is stable as long as $w_n(T) < 1$ for $n > 0$ or, equivalently, the integral is negative. Since $U(t)$ satisfies Equation (33), if we differentiate with respect to t, we have

$$\frac{dQ}{dt} = K[R'(U(t))\Delta(U) + \Delta'(U(t))R(U(t))]Q$$

where $Q = dU/dt$. As $Q(t)$ is T-periodic, it follows that we must have

$$\exp\left(K \int_0^T [R'(U(t))\Delta(U) + \Delta'(U(t))R(U(t))] \; dt\right) = 1.$$

Thus, the integral inside the exponential vanishes and

$$\int_0^T [R'(U(t))\Delta(U) \; dt = -\int_0^T \Delta'(U(t))R(U(t))] \; dt. \tag{35}$$

Thus, using this equality, we see that synchrony is stable if and only if

$$\kappa_n \equiv (1-k_n)\int_0^T \Delta'(U(t))R(U(t)) \; dt < 0 \tag{36}$$

for $n > 0$. For example, if $R(u)$ is concentrated near $u = 0$ and $\Delta'(0) < 0$, then we obtain stability of synchrony, as long as $k_n < 1$, such as for a Gaussian or exponential kernels (cf Equation (32)). Throughout the remainder of this chaper, we will work in regimes where there is a stable synchronous solution. In most of this chaper, we will be considering the limiting case where $R(U)$ is the Dirac delta function. In this case, synchrony is stable if $\Delta'(0) < 0$ and $k_n < 1$.

2.2.2 Traveling waves

Henceforth, we confine our attention to the case in which $R(u) = \sum_{m=-\infty}^{\infty} \delta(u + 2\pi m)$, the "periodized" Dirac function. We additionally assume, $\Delta(0) = 0$ and $\Delta'(0) < 0$, assuring that synchrony is stable for non-negative kernels. We seek solutions, $u(x, t) = U(\xi)$ with $\xi = ct - x$:

$$c\frac{dU(\xi)}{d\xi} = 1 + K\Delta(U(\xi)) \int_0^L k_L(\xi - y)R(U(y))\, dy \tag{37}$$

with the condition that $U(\xi + L) = U(\xi) + 2\pi$. Since the wave is translation invariant, we fix the position by setting $U(0) = 0$. Thus, $U'(0) = 1/c$, so the equation for the traveling wave is just:

$$\frac{dU}{d\xi} = \frac{1}{c} + K\Delta(U)k_L(\xi) \tag{38}$$

where $U(0) = 0$ and $U(L^-) = 2\pi$, by L^- we mean the limit from below. We now prove there is a unique solution.

Lemma 1. Suppose $\Delta(0) = 0$ and $\Delta(u), k_L(\xi)$ are bounded and continuous. Then there is a unique solution to Equation (37) with $U(0) = 0, U(L^-) = 2\pi$.

Proof. Let $\beta = 1/c$ and $w(\xi, \beta)$ be solution to the initial value problem

$$\frac{dw(\xi, \beta)}{d\xi} = \beta + K\Delta(w(\xi, \beta))k_L(\xi)$$

with $w(0, \beta) = 0$. By a simple comparison argument, let $\beta_1 > \beta_2$, if $w(\xi, \beta_1) = w(\xi, \beta_2)$ for some ξ, then $dw(\xi, \beta_1)/d\xi > dw(\xi, \beta_2)/d\xi$. Therefore $w(L, \beta_1) > w(L, \beta_2)$ since $dw(\xi, \beta)/d\xi|_{\xi=0} = \beta$. Clearly, $w(L, 0) = 0$. Furthermore, since $\Delta(w)k_L(\xi)$ is bounded, for β large enough, $w(L, \beta) > 2\pi$. The monotonicity of $w(L, \beta)$ with respect to β guarantees that there is a unique β_L so that $w(L, \beta_L) = 2\pi$. We thus take $U(\xi) = w(\xi, \beta_L)$. $\square$

With existence established, we can numerically compute the period, $P = L/c$ of the wave as a function of L for different types of PRCs. Figure 3 shows the period $P = L/c$ of the traveling wave as a function of L for the exponential kernel (where $G_e = \exp(-|x|)/2$) and $\Delta(u) = \sin(d) - \sin(u + d)$ for different pairs, (K, d). We also show one example with a Gaussian kernel (G). (That is, $k_L(x) = \sum_{n=-\infty}^{\infty} G_0(x + nL)$, where $G_0(x) = \exp(-x^2)/\sqrt{\pi}$.)

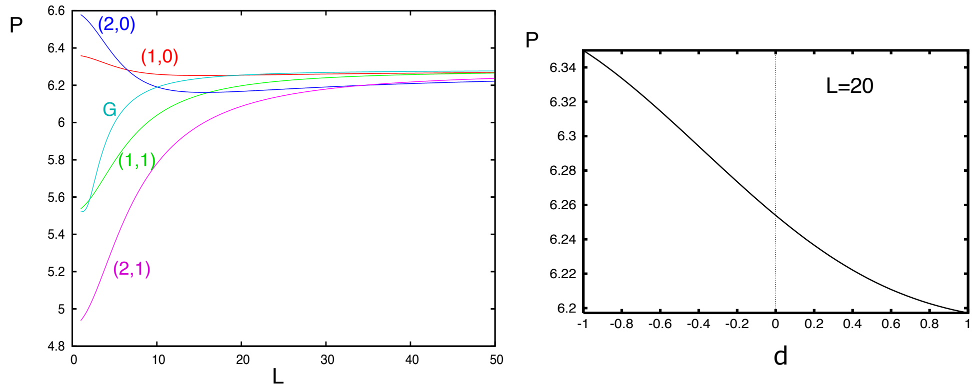

Figure 3: Period of the wave as a function of the length L of the ring for the exponential kernel and $\Delta(u) = \sin(d) - \sin(u + d))$ for pairs (K, d). Curve labeled G is for a Gaussian with $(K, d) = (1, 1)$. Right panel shows $P(d)$ for $K = 1, L = 20$.

In all cases, as L increases all curves converge to 2π, the period of the synchronous oscillation. Note that $c = L/P$, so c increases roughly linearly with L unlike the waves in an excitable medium. On the right panel of the figure, we show the period as d changes for $K = 1, L = 20$.

2.2.3 Stability of traveling waves

We now turn to the formal stability of the traveling waves. We replace x by the moving coordinate, $\xi = ct - x$ so that we have:

$$\frac{\partial u}{\partial t} + c\frac{\partial u}{\partial \xi} = 1 + K\Delta(u(\xi, t)) \int_0^L k_L(\xi - y)R(u(y, t))\, dy. \tag{39}$$

The traveling wave solution, $U(\xi)$ is a stationary solution to this evolution equation. We write $u(\xi, t) = U(\xi) + \zeta(\xi, t)$ where ζ is small and take only the terms linear to ζ to get the formal linearization of Equation (39):

$$\begin{aligned}\frac{\partial \zeta}{\partial t} + c\frac{\partial \zeta}{\partial \xi} =& K\left(\Delta(U(\xi)) \int_0^L k_L(\xi - y)R'(U(y))\zeta(y, t)\, dy\right.\\ &\left. + \Delta'(U(\xi))\zeta(\xi, t) \int_0^L k_L(\xi - y)R(U(y))\right)\, dy.\end{aligned} \tag{40}$$

Letting $\zeta(\xi,t) = e^{\lambda t}v(\xi)$, we obtain the formal linear eigenvalue problem:

$$\begin{aligned}\lambda v(\xi) + c\frac{dv}{d\xi} =& K\left(\Delta(U)\int_0^L k_L(\xi-\eta)R'(U(\eta))v(\eta)\ d\eta\right.\\ &\left.+\Delta'(U)v(\xi)\int_0^L k_L(\xi-\eta)R(U(\eta))\ d\eta.\right.\end{aligned} \tag{41}$$

This eigenvalue problem includes the term $R'(U(\eta))$ which is thus the formal derivative of the delta function applied to the solution $U(\eta)$. We will interpret these formal terms in the sense of distributions and, thus, to use them in the stability equation, we must compute their meaning in terms of elementary distributions such as the Dirac δ function, the dipole function (negative "derivative" of the δ function) and others [41]

Lemma 2. Suppose $u(0) = 0$, $u'(0) > 0$, and $u''(0)$ exists, then for any test function $f(x)$ (C^∞ functions with compact support):

$$\begin{aligned}\int f(\eta)\delta(u(\eta))\ d\eta &= \frac{f(0)}{|u'(0)|},\\ \int f(\eta)\delta'(u(\eta))\ d\eta &= -\left(\frac{f'(0)u'(0)-f(0)u''(0)}{u'(0)^3}\right).\end{aligned} \tag{42}$$

Proof. Proof of the first statement:

$$\int f(\eta)\delta(u(\eta))\ d\eta = \int \frac{f(u^{-1}(v))\delta(v)}{u'(u^{-1}(\eta))}\ dv = \frac{f(u^{-1}(0))}{|u'(u^{-1}(0))|} = \frac{f(0)}{|u'(0)|} \qquad \square$$

Proof of the second statement:

$$\begin{aligned}\int f(\eta)\delta'(u(\eta))d\eta &= \int \frac{f(u^{-1}(z))\delta'(z)}{u'(u^{-1}(z))}dz\\ &= -\frac{d}{dz}\left[\frac{f(u^{-1}(z))}{u'(u^{-1}(z))}\right]\Bigg|_{z=0}\\ &= -\left\{f(u^{-1}(z)\cdot\frac{-u''(u^{-1}(z))}{u'(u^{-1}(z))^2}\cdot\frac{d}{dz}u^{-1}(z)+\frac{f'(u^{-1}(z))\cdot\frac{d}{dz}u^{-1}(z)}{u'(u^{-1}(z))}\right\}\Bigg|_{z=0}\\ &= -\left\{f(0)\cdot\left(\frac{-u''(0)}{u'(0)^3}\right)+\frac{f'(0)}{u'(0)^2}\right\}\\ &= -\frac{f'(0)u'(0)-f(0)u''(0)}{u'(0)^3} \qquad \square\end{aligned}$$

$\square$

In order to use Section 2.2.3 in Equation (41), we need to evaluate, $v'(0)$ using the fact that $U(0) = 0$ and $\Delta(0) = 0$. Substituting $\xi = 0$ in Equation (41), we get:

$$\lambda v(0) + cv'(0) = cK\Delta'(0)v(0)k_L(0)$$

so that

$$v'(0) = (K\Delta'(0)k_L(0) - \frac{\lambda}{c})v(0).$$

Together with Section 2.2.3, the eigenvalue equation Equation (41) becomes:

$$\frac{\lambda}{c}v(\xi) + v'(\xi) = K\left(\Delta'(U(\xi))v(\xi)k_L(\xi) + c\Delta(U(\xi))k_L'(\xi)v(0) + \lambda\Delta(U(\xi))k_L(\xi)v(0)\right), \quad (43)$$

along with the periodic boundary conditions $v(0) = v(L)$. As it is a good "reality check", we show that $\lambda = 0$ is an eigenvalue and $V(\xi) = dU/d\xi$ is an eigenfunction. To see this, note from Equation (38) that $V(0) = \beta = 1/c$. Differentiate Equation (38) with respect to ξ to obtain that

$$\frac{dV}{d\xi} = K\left(\Delta'(U(\xi))k_L(\xi)V + c\Delta(U(\xi))k_L'(\xi)V(0)\right)$$

as desired where we use the fact that $cV(0) = 1$. We can write down an explicit solution to the equation by solving the linear ODE, but this involves integrals of $\Delta(U(\xi))$ multiplied by exponentials of integrals also involving $U(\xi)$, ultimately leading to:

$$V(\xi) = V(0)M(\xi, \lambda),$$

where M is a 2π-periodic function with eigenvalue λ. Setting $\xi = L$ and using periodicity, we get $M(L, \lambda) = 0$. Solving this, generally transcendental, equation for λ yields the eigenvalues and thus the stability. As this approach is not particularly fruitful, we numerically solve Equation (43) as a linear boundary value problem along with the simultaneous solution to Equation (38). Before doing so, we provide some intuition about the expected behavior. If we set $\Delta = 0$, we see immediately that $v(\xi) = \exp(2\pi in\xi/L)$ and $\lambda = -2\pi inc/L$ is imaginary for $n \neq 0$. Thus, we expect that there will be complex eigenvalues and we need to determine when the real part is positive. Clearly if $v(0) = 0$, then $v(\xi) = 0$, so we can take $v(0) = 1$. We scale $s = \xi/L$ and write λ, v in terms of real and imaginary parts, $\lambda = \lambda_r + i\lambda_m$, $v = v_r + iv_m$ and solve:

$$\begin{cases} \dfrac{\lambda_r v_r - \lambda_m v_m}{c} + \dfrac{v_r'}{L} = K\Delta'(u) v_r k_L(s) + \lambda_r K\Delta(u) k_L(s) + cK\Delta(u) k_L'(s) \\ \dfrac{\lambda_m v_r + \lambda_r v_m}{c} + \dfrac{v_m'}{L} = K\Delta'(u) v_m k_L(s) + \lambda_m K\Delta(u) k_L(s) \\ v_r(0) = v_r(1) = 1 \\ v_m(0) = v_m(1) = 0. \end{cases} \tag{44}$$

We numerically solve this boundary value problem for the free parameters λ_r, λ_m starting with $\lambda_m = n$, for $n = 1, 2, \ldots$. Figure 4A shows an example calculation or the exponential kernel ($k_L(x) = [\exp(x) + \exp(L - x)]/[2(\exp(L) - 1)]$), $\Delta(u) = -\sin(u)$ for $n = 1, 2$. For $n = 1$, if L is smaller than about 9.2, then the wave is unstable to perturbations with $\lambda_m \approx 1$, but is stable to higher modes until L gets very close to 0. For modes $n > 2$, we find that the wave is also stable. Thus, if the domain size is too small, even though the wave exists, it is unstable. We next track the value L^* at which the wave loses stability at the $n = 1$ mode (the most unstable mode) as we vary the coupling strength K and shape of $\Delta(u) = \sin(d) - \sin(d + u)$. This is shown in Figure 4B. For $d = 0$, the larger coupling strength K causes a loss of stability for slightly larger values of L. For $d < 0$ the wave is destabilized at larger L while for $d > 0$, it is destabilized at smaller L.

2.2.4 Other shapes of PRCs

In [11], the authors measured the PRCs in mitral cells (a type of neuron that responds to different odors) and found that we could parameterize their shape with a function that has the form:

$$\Delta_M(u) = (\sin(d) - \sin(u + d)) \exp(\kappa(u - 2\pi)). \tag{45}$$

This function vanishes at $u = 0, 2\pi$. (Note that $\kappa = 0$ recovers our standard PRC.) Figure 5A shows example Δ_M which are PRCs for different values of the shaping parameter κ. This parameter determines how flat the PRC is in the early part of the cycle, with the flatter PRCs occurring when κ is larger. Typical values for neurons had values of K, d, κ between 0 and 1. Thus, we take $K = 1, d = 0.5$ and let κ range over several values. Panels B,

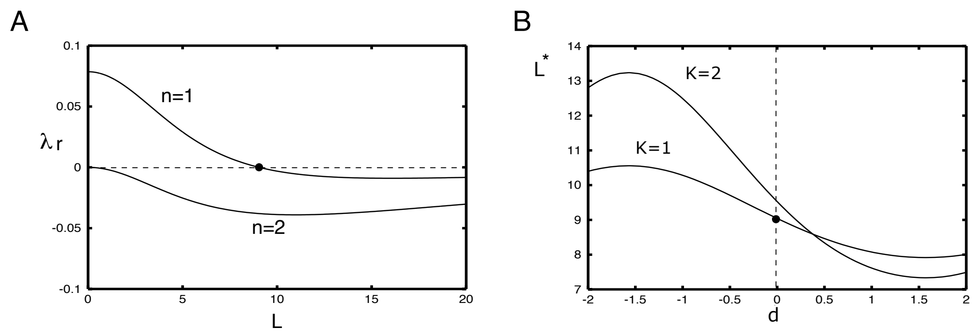

Figure 4: Numerically determined solutions to the eigenvalue problem (Equation (44)) for $\Delta(u) = \sin(d) - \sin(u + d)$. (A) Real part of the eigenvalue as L varies for $\lambda_m \approx n$. Solid dot shows the value of L at which the λ_r changes sign. (B) The critical value L^* at which $\lambda_r = 0$ when $n = 1$ as d varies for $K = 1, 2$. Solid dot corresponds to the dot in panel A.

C show the dispersion rate and the real part of the most unstable eigenvalue at the same values of κ. Qualitatively, κ does not have much effect on the dispersion; the shallowing is a consequence of the fact that the average amplitude of the PRC decreases with increasing κ. Even with that difference, the dependence on the length is less sensitive with larger κ. In general, flattening of the PRC has the effect of destabilizing waves in the sense that as κ increases, the waves are destabilized at longer values of L.

2.3 Perturbation Approximations

Our results in the preceding section are all numerical, so it is natural to ask whether there any analytic approaches where we can obtain approximations to the dispersion and stability of the traveling waves. Looking at Equation (31), when $R(u) \equiv 0$ (zero effect of other oscillators) we see that $u(x, t) = t + 2\pi x/L$ is a traveling wave solution with winding number 1. This suggests that we might be able to compute traveling wave solutions if the interaction coupling function $R(u)$ is small in magnitude, say, $R(u) = O(\epsilon)$, where $0 < \epsilon \ll 1$, then we should be able to develop an approximation for the dispersion and stability. We will

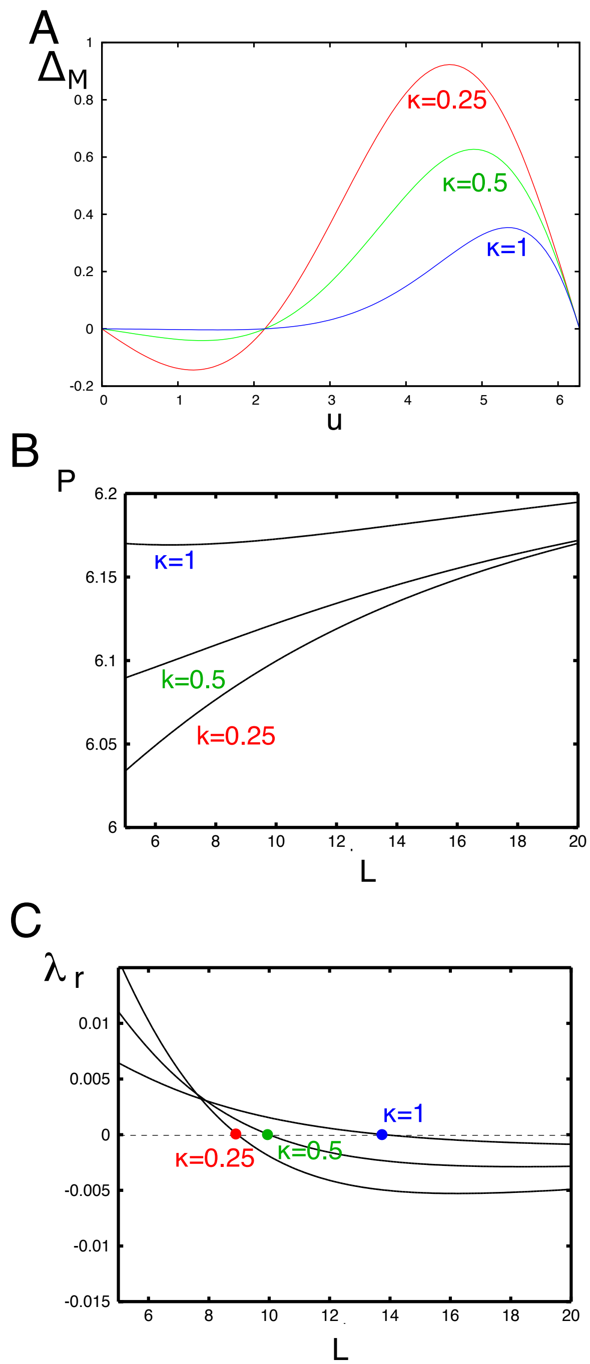

Figure 5: Dispersion relation (period, P) and stability of waves as the ring length, L varies for approximations (Equation (45)) of the PRC for a mitral cell, coupling strength $K = 1$. (A) PRC with $d = 0.5$ and $\kappa = 0.25, 0.5, 1.0$. (B) Dispersion relation corresponding to the PRCs in A. (C) Stability of waves (dots indicate the critical ring length where stability is lost).

first compute first and second order approximations for the dispersion relation. We follow for a first order approximation for the stability.

2.3.1 Perturbation and dispersion

We first compute the dispersion relation, $P(L)$ by assuming the amplitude that $R(u) = \epsilon\delta(u)$ where $0 < \epsilon \ll 1$. We rewrite Equation (38) as

$$\frac{dU}{ds} = P + \epsilon K L k_L(Ls)\Delta(U) \tag{46}$$

where $s = \xi/L$, $P = L/c$, and we have explicitly included the amplitude of $R(u)$ in the parameter ϵ. We write the solution to Equation (46) as a function $U(s,\epsilon)$ where we explicitly include the ϵ and assume that we can expand $U(s,\epsilon)$ in a power series in ϵ. Solutions to Equation (46) must be periodic in s in the sense of phase, so that $U(s+1,\epsilon) = U(s,\epsilon) + 2\pi$. We can fix the 0 phase, by requiring $U(0,\epsilon) = 0$. Thus, we seek solutions to Equation (46) such that $U(0,\epsilon) = 0$ and $U(1,\epsilon) = 2\pi$. We expand U and P in ϵ, $U(s,\epsilon) = u_0(s) + \epsilon u_1(s) + \dots$ and $P(\epsilon) = P_0 + \epsilon P_1 + \dots$ obtaining the series of equations:

$$u_0' = P_0 \quad u_0(0) = 0,\ u_0(1) = 2\pi \tag{47}$$

$$\begin{aligned} u_1' &= P_1 + K L k_L(Ls)\Delta(u_0) \quad u_1(0) = 0,\ u_1(1) = 0 & (48)\\ u_2' &= P_2 + K L k_L(Ls)\Delta'(u_0)u_1 \quad u_2(0) = 0,\ u_2(1) = 0 & (49)\end{aligned}$$

Clearly, the solution to Equation (47) is $P_0 = 2\pi$ and $u_0 = 2\pi s$. Integrating the second equation from 0 to 1 and using the boundary conditions, we get

$$P_1 = -KL\int_0^1 k_L(Ls)\Delta(2\pi s)\ ds$$

and

$$u_1(s) = P_1 s + KL\int_0^s k_L(Ls')\Delta(2\pi s')\ ds'.$$

Similarly, we obtain:

$$P_2 = -KL\int_0^1 k_L(Ls)\Delta'(2\pi s)u_1(s)\ ds.$$

As an example, if we take $K = 1$, $\Delta(u) = \sin(d) - \sin(d+u)$ and $k_L(Ls)$ the exponential and find:

$$P_1 = -\sin(d)\frac{4\pi^2}{L^2 + 4\pi^2}. \tag{50}$$

We see that if $d = 0$, that is $\Delta(u)$ is an odd periodic function, then, $P_1 = 0$ and the period is independent of L to order ϵ. As Figure 3 shows, there is a dependence of the period on L when $d = 0$, so to explain this dependence, we go to a higher order. Evaluating the integrals when $d = 0$, we obtain:

$$P_2(d=0) = \frac{\pi L}{4}\left(\frac{[L^2 - 4\pi^2][1 - \exp(2L)] + 2L\exp(L)[L^2 + 4\pi^2]}{[L^2 + 4\pi^2]^2[\exp(L) - 1]^2}\right). \tag{51}$$

Figure 6 show some comparisons of the perturbation expansions with the numerically determined dispersion relation for $\epsilon = 1$. In panel A, we show the comparison for $d = 1$ over a range of L. Even though $\epsilon = 1$, the approximation is pretty good with a small deviation for L near 0. Panel B fixes $L = 20$ and varies d between -1 and 1. There is a small error. In panel C, we set $d = 0$ which to order ϵ yields $P = 2\pi$ (shown as the dotted line). But, including the higher order terms, we obtain results indistinguishable from the numerical calculations. In sum, the perturbation theory works quite well even for reasonably large ϵ.

2.3.2 Perturbation and stability

We begin with Equation (43) which we rewrite to include ϵ:

$$\frac{\lambda}{c}v(\xi) + v'(\xi) = \epsilon K\left(\Delta'(U(\xi))v(\xi)k_L(\xi) + c\Delta(U(\xi))k_L'(\xi)v(0) + \lambda\Delta(U(\xi))k_L(\xi)v(0)\right)$$

subject to the boundary conditions, $v(0) = v(L) = 1$. (Note that we could enforce some other type of normalization on the eigenfunction; this is just convenient and will not change λ. Indeed, if we choose $v(0) = 0$, then by uniqueness, $v(\xi) = 0$ for all ξ, so any eigenfunction must have $v(0) \neq 0$.) We recall from the previous section that $c \equiv L/P = L/(2\pi) + O(\epsilon)$ and $U(\xi) = 2\pi\xi/L + O(\epsilon)$. We write $v = v_0 + \epsilon v_1 + \ldots$ and $\lambda = \lambda_0 + \epsilon\lambda_1 + \ldots$. Plugging in this perturbation series, we obtain zero order:

$$\frac{\lambda_0}{c}v_0 + v_0' = 0$$

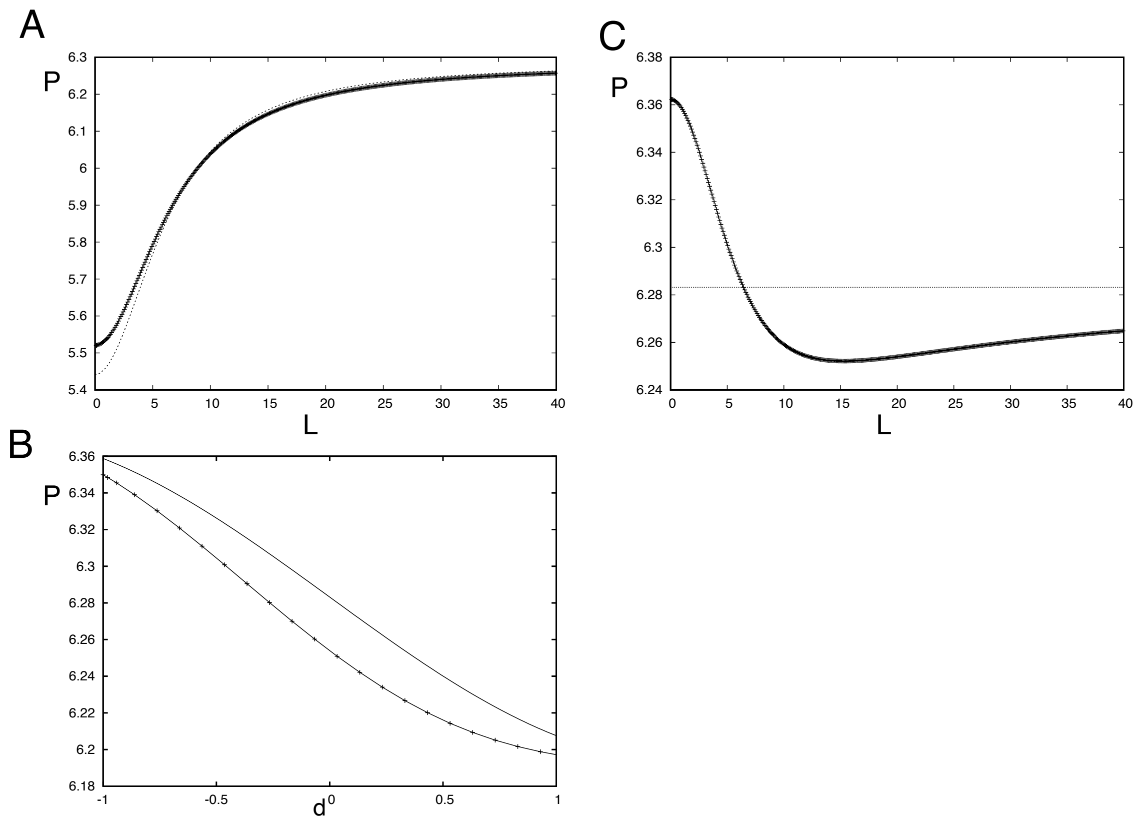

Figure 6: Comparison of the perturbation expansion with the numerically determined dispersion relations. (A) $2\pi + \epsilon P_1$ Equation (50) for $\epsilon = 1, d = 1$ (thin dotted line) compared to the numerical calculation (crosses); (B) For $L = 20, \epsilon = 1$ perturbation (solid line, Equation (50)) compared to numerical results (line points); (C) For $\epsilon = 1, d = 0$, second order $2\pi + \epsilon^2 P_2$ (solid line, Equation (51)) compared to numerical results (curves indistinguishable).

with $v_0(0) = v_0(L) = 1$. We immediately find, $\lambda_0 = 2\pi inc/L$ and $v_0(\xi) = \exp(-2\pi ni\xi/L)$ where n is an integer. The next order equation is

$$\frac{2\pi in}{L}v_1 + v_1' = -\frac{\lambda_1}{c}v_0(\xi) + K\left(\Delta'(u_0)v_0(\xi)k_L(\xi)\right. \qquad (52)$$
$$\left. + \lambda_0\Delta(u_0)k_L(\xi) + c\Delta(u_0)k_L'(\xi)v_0(0)\right) := S(\xi,\lambda_1)$$

With the inner product,

$$\langle u(\xi), v(\xi)\rangle = \int_0^L \bar{u}(\xi)v(\xi)\ d\xi$$

The linear operator on the left-hand side is self-adjoint in the space of $L-$periodic functions and has a one-dimensional nullspace, $v_0(\xi)$ Thus, to obtain a periodic solution, we must have that, $\langle v_0(\xi), S(\xi,\lambda_1)\rangle = 0$. With this, we obtain:

$$\Re\lambda_1 = \frac{KL}{2\pi}\int_0^1 \left(\Delta'(2\pi s)k_L(Ls) - n\sin(2\pi ns)\Delta(2\pi s)k_L(Ls)\right.$$
$$\left. + \frac{KL}{2\pi}\ k_L'(Ls)\Delta(2\pi s)\cos(2\pi ns)\right)\ ds.$$

where we have substituted $c_0 = L/(2\pi)$ where it appears. This expression is a bit unwieldy, but we note that $dk_L(Ls)/ds = Lk_L'(Ls)$, so that we can write

$$-n\sin(2\pi ns)\Delta(2\pi s)k_L(Ls) + \frac{L}{2\pi}k_L'(Ls)\Delta(2\pi s)\cos(2\pi ns)$$

as

$$\frac{1}{2\pi}\frac{d}{ds}(\cos(2\pi ns)k_L(Ls))\Delta(2\pi s)$$

and then integrate by parts to get a much more compact expression:

$$\Re\lambda_1 = \frac{kL}{2\pi}\int_0^1 k_L(Ls)\Delta'(2\pi s)[1-\cos(2\pi ns)]\ ds. \qquad (53)$$

Note that for $n = 0$, $\Re\lambda_1 = 0$ as expected. We write $\Delta(u) = \sum_{m=0}^{\infty} a_m\sin(mu) + b_m\cos(mu)$. Since $k_L(Ls)$ and $\cos(2\pi ns)$ are even functions, we see that $\Re\lambda_1$ is independent of b_m to this order. Recall that $k_L(Ls)$ is the periodized version of some connectivity kernel, $K(x)$. Let

$\hat{K}(\nu)$ be the Fourier transform of $K(x)$. Then, using trigonometric identities and the Fourier expansion of $\Delta(u)$, we obtain:

$$\begin{aligned} \Re\lambda_1 &= KL \sum_{m>0} m a_m \Big[\hat{K}(2\pi m/L) - (1/2)(\hat{K}(2\pi(m-n)/L) \\ &+ \hat{K}(2\pi(m+n)/L))\Big]. \end{aligned} \tag{54}$$

Setting $n = \pm m$ and letting $L \to 0$, we see that

$$\frac{\Re\lambda_1}{KL} \to -n a_n \hat{K}(0)/2.$$

Recall in the remarks after Equation (36), that we showed that synchrony was stable if $\Delta'(0) < 0$. This implies $\sum_m m a_m < 0$. Thus, there must be some n such that $n a_n < 0$. Thus, for short waves (L small), we find that $\Re\lambda_1 > 0$ for some n and these waves are unstable. For long waves, $L \to \infty$, we see that

$$L\Re\lambda_1 \to -(K/2)\hat{K}''(0) n^2 \sum_{m>0} m a_m.$$

For kernels like the exponential and the Gaussian, 0 is a local maximum for $\hat{K}$, so $\hat{K}''(0) < 0$ and so with the hypothesis that $\Delta'(0) < 0$ (synchrony is stable), we see that waves that are sufficiently long are stable.

If we suppose $a_1 < 0$ and $m = 1$ is the dominant mode in $\Delta(u)$, then we can solve Section 2.3.2 for the critical value of L, L_c by solving

$$\hat{K}(\nu) - (1 + \hat{K}(2\nu))/2 = 0 \tag{55}$$

for $\nu > 0$ and then $L_c = 2\pi/\nu$ is the minimal stable wave-length.

Example. For our present model (sinusoidal PRC and exponential kernel, coupling strength $K = 1$), we find that

$$\Re\lambda_1 = -2n^2 L^2 \pi \cos(b) \frac{L^2 + \pi^2(4n^2 - 12)}{(L^2 + 4\pi^2)(4(n+1)^2\pi^2 + L^2)(4(n-1)^2\pi^2 + L^2)}.$$

For $n > 1$ and $b \in (-\pi/2, \pi/2)$, $\Re\lambda_1 < 0$, so that all lengths are stable to these modes independent of L. However, for $n = 1$, we see that $\Re\lambda_1$ is positive for $L < 2\pi\sqrt{2} \approx 8.88$, so that waves on short rings are unstable. We note that the Fourier transform of the exponential is $1/(1+\nu^2)$ so that solving Equation (55) we find $\nu = \sqrt{2}/2$ and get the same value for the critical L. This value of L is pretty close to the value of 9.2 that we saw in Figure 15A where $\epsilon = 1$. For a Gaussian kernel, the Fourier transform is $\exp(-n^2/4)$, the solution to Equation (55) is $\nu \approx 1.559$ and the critical value of L is approximately 4.03. So Gaussian kernels tolerate much smaller values of L than exponentials.

Finally, turning to the "mitral cell" PRC (Equation (45)), we can obtain an expression for the real part of the eigenvalue (although it is very cumbersome). We find, just as in Figure 5C, that for $b = 0.5$, the critical length for stability increases with d; specifically, $L_c = 8.96, 9.79, 13.26$ for $d = 0, 25, 0.5, 1.0$ respectively. These are very close matches with the filled circles in Figure 5C, even though $\epsilon = 1$.

2.4 Smooth Coupling

In the previous sections, we have focused on the coupling that is via a Dirac delta function. Thus, it would be interesting to check if the qualitative behavior such as the dispersion relation and stability persists for smooth functions. For this reason, we return to Equation (31) and numerically analyze the behavior for the case in $R(u) = N(\gamma)\exp(-\gamma(1-\cos u))$ where $N(\gamma)$ is chosen so that the integral of $R(u)$ is 1. A qualitatively similar form of pulse coupling, $R(u) = A(\gamma)(1+\cos u)^\gamma$, was used in [50]; both approach a periodic Dirac delta function as the parameter $\gamma \to \infty$. For purposes of illustration, we take $\gamma = 20, 50$ so that the pulse is fairly sharp (Figure 7A) and choose $\Delta(u) = \sin(d) - \sin(u+d)$ with $d = 0.5$, the coupling strength $K = 1$. We use the periodized exponential kernel so that we can convert the existence of a pulse into a simple boundary value problem. If we write

$$V(x,t) = \int_0^L k_L(x-y)R(u(y,t))\, dy$$

with $k_L(x)$, exponential, then

$$\frac{\partial^2 V(x,t)}{\partial x^2} = V(x,t) - R(u(x,t)). \tag{56}$$

Traveling waves satisfy:

$$\begin{aligned} c\frac{du}{d\xi} &= 1 + \Delta(u)V \\ \frac{d^2V}{d\xi^2} &= V - R(u) \end{aligned}$$

with $V(0) = V(l), V_\xi(0) = V_\xi(L)$. Figure 7B shows the period, $P = L/c$ as a function of L for the smooth model for the two values of γ along with the same for the delta function. The shapes are qualitatively the same and the $\gamma = 50$ case sits between the $\gamma = 20$ case and the delta function as is expected. Finally, we can also numerically determine the stability of the pulse by linearizing about the traveling wave. We solve the eigenvalue problem:

$$\begin{aligned} \lambda v + c\frac{dv}{d\xi} &= \Delta(u)w + \Delta'(u)Vv \\ \frac{d^2w}{d\xi^2} &= w - R'(u)v \end{aligned}$$

for (v, w, λ). By starting with $\Im\lambda = n$ we can examine the stability of different modes. We find numerically that $n > 1$ always leads to $\Re\lambda < 0$, but $n = 1$ induces an instability, just as in the delta-function case. Figure 7C shows $\Re\lambda$ as a function of L for $\gamma = 20, 50$ and the delta function case. The curves are nearly indistinguishable and cross zero at nearly the same value of L. Thus, just as in previous sections, we see that waves on short rings are unstable.

2.5 Discussion

In this chapter, we have analyzed the existence and stability of traveling waves for a continuum network on a one-dimensional ring of non-locally coupled oscillators where the phase-resetting curve allows for stable synchrony. We have shown that if synchrony is stable then, traveling waves on sufficiently long rings are also stable. We also showed that if the ring length is too short, then the waves are unstable. We have focused on homogeneous networks in this study since we are able to reduce the existence and stability to the study of two-point boundary value problems (BVP). One obvious extension of this work would be to

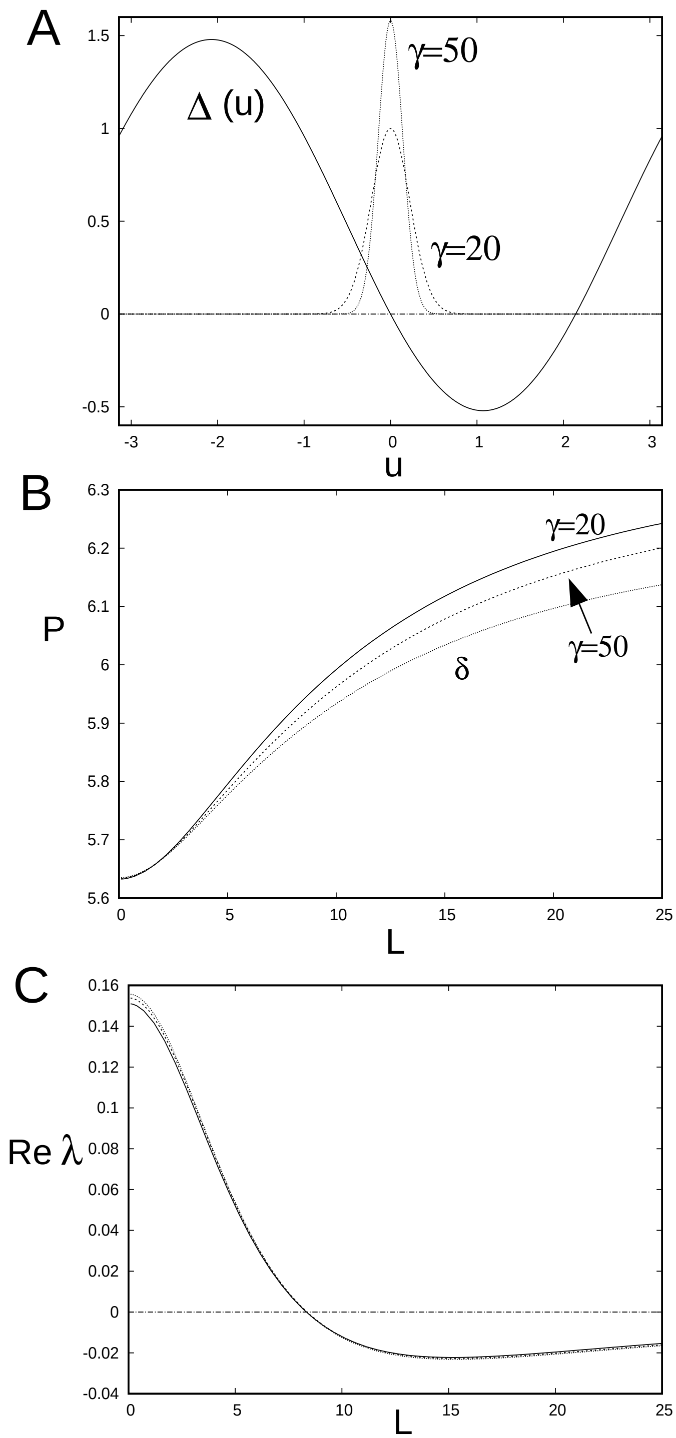

Figure 7: Behavior of Equation (37) when the kernel $R(u) = N(\gamma)\exp(-\gamma(1-\cos(u)))$ for $\Delta(u) = \sin(0.5) - \sin(u+0.5)$. (A) The PRC, $\Delta(u)$ along with $R(u)$ for $\gamma = 20, 50$ (all scaled to fit in the figure); (B) Period (P) as a function of ring-length, L for the smooth kernel and the Dirac delta function for comparison; (C) Stability ($\Re\lambda$) to $n = 1$ mode perturbations as a function of ring-length for the smooth functions and the Dirac delta function.

explore the susceptibility to noise or heterogeneity. For sinusoidal PRCs and delta function coupling, it is possible to extend the Ott-Antonsen approach [44, 45, 72] to incorporate spatially distributed networks. The advantage of this formulation is that one can still find the wave via a BVP. The approach we have taken here is reminiscent of that used in [12] for the existence of pulses in a non-locally coupled excitable medium. In that paper, the authors analyzed a solitary pulse on the infinite line and did not compute the dispersion relation or the stability of the waves. In general, stability is difficult to compute except in cases where the dynamics is governed by non-smooth systems such as the present delta-function approach and the work of Coombes and collaborators [13] where the step function figures prominently.

We found a close connection between the present work and that of [26] which studied the case non-local coupling in *phase-difference* oscillators. Indeed, the first order perturbation agrees with that paper and the stability calculation. Interestingly, the dispersion relation is flat to lowest order when the PRC is a pure sinusoid, as also predicted by weak coupling analysis. However, here we are able to compute higher order terms in the pure sine case that show dispersive behavior seen in the finite amplitude simulations.

We have focused exclusively on waves with *winding number 1*, that is $u(x,t)$ advances by 2π as x goes from 0 to L. Waves with winding number $m > 1$ are equivalent to waves of winding number 1 on a ring of length L/m. In our case, a wave with winding number 0 is just synchrony. However, an interesting question is whether there are other types of waves besides these simple plane waves. In [35], the authors found so-called "ripple waves", modulated periodic solutions could bifurcate from the simple plane waves when the coupling kernel, $k_L(x)$ is positive for x near 0 and negative for x near $\pm L/2$ when the negative region gets sufficiently large. We conjecture that if $k_L(x) \geq 0$, then the plane waves are the only stable solutions.

Finally, it remains to be seen how much of this work could be extended beyond phase models. One intriguing approach is the use of so-called isostable reductions [70, 21], or higher order phase models [49]. Thus, in addition to Equation (37), there would be an additional amplitude equation (or multiple amplitude equations) that are coupled to the spatial phase. It is unclear whether the behavior in this extended case would be qualitatively different or richer than the simple phase models. Typically, the amplitude terms have little effect unless near bifurcations.

3.0 Pulse Coupling on Annulus

3.1 Model

In the previous chapter, we discussed traveling waves and dispersion relation of an non-local pulse coupling model on a one-dimensional ring domain. Here we extend our analysis to 2-dimensional space and investigate the non-local pulse coupling on the annulus domain. Thus the phase model of identical pulse coupled oscillators is written as:

$$\frac{\partial u(\mathbf{x},t)}{\partial t} = 1 + K\Delta(u(\mathbf{x},t)) \int_D W(|\mathbf{x}-\mathbf{x}'|)P(u(\mathbf{x}',t))\ d\mathbf{x}' \tag{57}$$

where $\mathbf{x} = (x, y)$ is a point in the 2-dimensional domain D, $u \in [0, 2\pi)$ is a phase variable, $\Delta(u)$ is the phase-resetting curve for the uncoupled oscillator, K is an overall coupling strength, $W(|X|)$ is the distance-dependent coupling strength, (typically, we assume that the integral of W is 1 when $D = \mathbb{R}^2$), and $P(u)$ is a pulsatile interaction function. If $0 < K \ll 1$, then we can use the theory of weak coupling to reduce this model as follows. Let $u(\mathbf{x},t) = t + v(\mathbf{x},t)$. Then after averaging

$$\frac{\partial V(\mathbf{x},t)}{\partial t} = K \int_D W(|\mathbf{x}-\mathbf{x}'|)H(V(\mathbf{x}',t) - V(\mathbf{x},t))\ d\mathbf{x}', \tag{58}$$

where

$$H(V) = \frac{1}{2\pi}\int_0^{2\pi} P(V+\xi)\Delta(\xi)\ d\xi.$$

When D is an annulus, [16] showed that this equation can admit N-armed rotating waves of the form:

$$V(r,\theta,t) = \Omega t + N\theta + f(r)$$

where we have introduced polar coordinates, $\mathbf{x} = (r\cos\theta, r\sin\theta)$ and $D = \{\mathbf{x} \in \mathbb{R}^2 | a < r < b\}$ is the annulus. In particular, it showed that if $H(V)$ is an odd periodic function, then $f(r) = 0$.

In this chapter, we will consider Equation (57) when $P(u)$ is a Dirac delta function and $\Delta(u) = -\sin(u)$. We numerically solve the rotating waves and then use perturbation theory to approximate the solutions. We show that pulse coupling makes $f(r)$ non-zero even if $\Delta(u)$ is an odd function.

3.2 Rotating waves

Let $\mathbf{x} = (r\cos\theta, r\sin\theta)$, $\mathbf{x}' = (s\cos\varphi, s\sin\varphi)$, the squared distance between them is

$$|\mathbf{x} - \mathbf{x}'|^2 = r^2 + s^2 - 2rs\cos(\varphi - \theta),$$

and the system Equation (57) in a polar coordinate can be written as,

$$\frac{\partial u(r,\theta,t)}{\partial t} = 1 + K\Delta(u(r,\theta,t)) \int_a^b s\ ds \int_0^{2\pi} W(r,s,\varphi-\theta)P(u(s,\varphi,t))\ d\varphi, \tag{59}$$

where a and b are inner and outer radii respectively.

We look for one-armed rotating waves thus write $u(r,\theta,t) = \xi - f(r)$ where the moving coordinates $\xi = \Omega t + \theta$, $\eta = \Omega t + \varphi$, then Equation (59) becomes

$$\Omega\frac{\partial u}{\partial \xi} = 1 + K\Delta(u(r,\xi)) \int_a^b s\ ds \int_0^{2\pi} W(r,s,\xi-\eta)P(u(s,\eta))\ d\eta. \tag{60}$$

Since u is a phase variable, it is required that $u(r,\xi+2\pi) = u(r,\xi) + 2\pi$, that is, u increases by 2π for each cycle.

Assume a spike is sent to coupled neurons when the phase variable of the neuron satisfies $u(r,\xi) = 0$. We consider the characteristic curve on the annulus such that $u(r,\xi) = 0$ where $\xi = f(r)$, so that convolution with Dirac delta function can be evaluated in Equation (60) which gives,

$$\Omega\frac{\partial u}{\partial \xi} = 1 + K\Delta(u(r,\xi)) \int_a^b s\,\mathrm{d}s \cdot \frac{W(r,s,\xi - f(s))}{\frac{\partial u}{\partial \xi}|_{\xi = f(s)}}. \tag{61}$$

In addition, we require $\Delta(0) = 0$, because the neuron does not respond to any inputs when it is itself spiking. It can be implied from Equation (61) that $\partial u/\partial\xi = 1/\Omega$ along the zero phase contour $\xi = f(r)$ where $\Delta(u) = \Delta(0) = 0$ (see Figure 8), which further reduces the resulting equation into

$$\Omega\frac{\partial u}{\partial \xi} = 1 + K\Omega\cdot\Delta(u(r,\xi)) \int_a^b s\ ds \cdot W(r,s,\xi - f(s)) \tag{62}$$

as well as boundary conditions,

$$\begin{aligned} u(r, f(r)) &= 0, \\ u(r, f(r) + 2\pi) &= 2\pi. \end{aligned} \tag{63}$$

We can reduce the dimension of freedom in boundary conditions by changing of variable that $\xi = \zeta + f(r)$, thus rewrite the system Equation (62) and Equation (63) as

$$\Omega \frac{\partial u}{\partial \zeta} = 1 + K\Omega \cdot \Delta(u(r,\zeta)) \int_a^b s\ ds \cdot W(r,s,\zeta + f(r) - f(s)) \tag{64}$$

along with

$$\begin{aligned} u(r{,}0) &= 0, \\ u(r{,}2\pi) &= 2\pi. \end{aligned} \tag{65}$$

In practice, we use PRC function $\Delta(u) = \sin(d) - \sin(u+d)$, where d is a parameter. Assume a symmetric Gaussian kernel $W(|\mathbf{x}|) = \exp(-|\mathbf{x}|^2)$, so that

$$W(r,s,\theta) = e^{-(r^2+s^2)} e^{2rs\cos\theta}. \tag{66}$$

For a fixed radius r, the boundary value problem Equation (64) can be solved in MATLAB or XPP. The resulting pattern with an odd PRC ($\Delta(u) = -\sin(u)$) is a twisted wave as shown in Figure 8.

3.2.1 Approximation for weak coupling

When the coupling strength K is small, we can reduce Equation (57) to a non-locally phase-difference coupled system discussed in [16] by weak coupling theory. Lemma 2.1 in [16] showed that there is a straight rotating wave solution to this system with an odd coupling function.

In this section, we apply the perturbation method directly to the pulse coupling system Equation (59) without reducing it to a phase-difference equation, and approximate the analytic solution when the coupling strength $K = \epsilon << 1$ is small. Thus the wave solution to Equation (59) is expended as a Taylor series in ϵ:

$$\begin{aligned} u &= u_0 + \epsilon u_1 + \epsilon^2 u_2, \\ \Omega &= \Omega_0 + \epsilon \Omega_1 + \epsilon^2 \Omega_2, \\ f &= f_0 + \epsilon f_1 + \epsilon^2 f_2. \end{aligned} \tag{67}$$

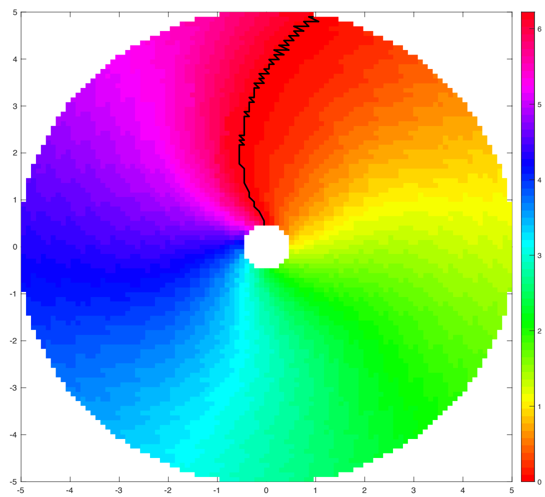

Figure 8: Rotating wave solution solved for pure sine coupling: K=1, $a = 0.5$, $b = 5$, $d = 0$. Black curve: characteristic curve calculating the rotating wave satisfies $f(r) = \xi$ or $u(r, \xi) = 0$. Colors indicate the phase of the oscillators.

Plugging Equation (67) into Equation (64), we obtain:

$$(\Omega_0+\epsilon\Omega_1+\epsilon^2\Omega)(\frac{\partial u_0}{\partial\zeta}+\epsilon\frac{\partial u_1}{\partial\zeta}+\epsilon^2\frac{\partial u_2}{\partial\zeta}\Big)=1+\epsilon\Delta(u_0+\epsilon u_1+\epsilon^2 u_2)\cdot(\Omega_0+\epsilon\Omega_1+\epsilon^2\Omega_2)\cdot$$
$$\int_a^b s\ ds\cdot W(r,s,\zeta+(f_0(r)-f_0(s))+\epsilon(f_1(r)-f_1(s))) \tag{68}$$

We can now solve Equation (68) by order in ϵ. At order 1 we find:

$$\Omega_0\frac{\partial u_0}{\partial\zeta}=1\Rightarrow\frac{\partial u_0}{\partial\zeta}=\frac{1}{\Omega_0},\quad u_0=\frac{\zeta}{\Omega_0}, \tag{69}$$

along with the boundary condition adapted from Equation (64):

$$\begin{aligned} u_0(r,0)&=0,\\ u_0(r,2\pi)&=2\pi. \end{aligned} \tag{70}$$

Hence we have $\Omega_0=1$, $u_0=\zeta$. It also implies that $f=O(\epsilon)$ where the twist of the rotating wave is a small quantity.

At order ϵ we have:

$$\Omega_0\frac{\partial u_1}{\partial\zeta}+\Omega_1\frac{\partial u_0}{\partial\zeta}=\Delta(u_0)\cdot\Omega_0\int_a^b s\ ds\cdot W(r,s,\zeta+f_0(r)-f_0(s)) \tag{71}$$

Let $f(a)=0$, thus $f_0\equiv 0$ in Equation (71):

$$\frac{\partial u_1}{\partial\zeta}+\Omega_1=\Delta(\zeta)\cdot\int_a^b s\ ds\cdot W(r,s,\zeta), \tag{72}$$

and boundary conditions on u_1 are:

$$\begin{aligned} u_1(r,0)&=0,\\ u_1(r,2\pi)&=0. \end{aligned} \tag{73}$$

Remember the PRC $\Delta(u)$ is a 2π periodic function, we can apply method of averaging to Equation (72) and take the integral over the angular domain $[0,2\pi)$, therefore we have an evaluation for Ω_1:

$$2\pi\Omega_1=\int_0^{2\pi}\Delta(\zeta)\ d\zeta\int_a^b s\ ds\cdot W(r,s,\zeta). \tag{74}$$

3.2.2 Odd coupling example

With odd PRC function $\Delta(u) = -\sin(u)$, and Gaussian kernel $W(|\mathbf{x}|) = \exp(-|\mathbf{x}|^2)$, we find Ω_1 vanishes because of the symmetry:

$$\begin{aligned}
2\pi\Omega_1 &= -\int_a^b s\ ds \int_0^{2\pi} \sin(\zeta)\cdot W(r,s,\zeta)\ d\zeta \\
&= -\int_a^b se^{-(r^2+s^2)}\ ds \int_0^{2\pi} \sin(\zeta)e^{2rs\cos(\zeta)}\ d\zeta \\
&= -\int_a^b se^{-(r^2+s^2)}\ ds \cdot 0 \\
&= 0.
\end{aligned} \tag{75}$$

Hence the frequency is approximated as $\Omega = 1 + \epsilon^2\Omega_2$. We then look at the order ϵ^2 equation of Equation (71) to get a higher order approximation:

$$\begin{aligned}
\Omega_0\frac{\partial u_2}{\partial\zeta} + \Omega_1\frac{\partial u_1}{\partial\zeta} + \Omega_2\frac{\partial u_0}{\partial\zeta} =& \Delta(u_0)\Omega_0\int_a^b s\ ds\cdot W'(r,s,\zeta+f_0(r)-f_0(s))\cdot(f_1(r)-f_1(s)) \\
&+\Delta(u_0)\Omega_1\int_a^b s\ ds\cdot W(r,s,\zeta+f_0(r)-f_0(s)) \\
&+\Delta'(u_0)u_1\Omega_0\int_a^b s\ ds\cdot W(r,s,\zeta+f_0(r)-f_0(s))
\end{aligned} \tag{76}$$

We plug in $f_0 = 0$ and evaluate the derivative of the kernel,

$$\begin{aligned}
W'(r,s,\zeta+f_0(r)-f_0(s)) =& \left.\frac{dW(r,s,\zeta+p)}{dp}\right|_{p=p_0} \\
&= -e^{-(r^2+s^2)}e^{2rs\cos(\zeta+p_0)}\cdot 2rs\sin(\zeta+p_0) \\
&= -2rs\cdot e^{-(r^2+s^2)}e^{2rs\cos(\zeta+p_0)}\cdot\sin(\zeta+p_0) \\
&= -2rs\cdot e^{-(r^2+s^2)}e^{2rs\cos\zeta}\cdot\sin\zeta
\end{aligned} \tag{77}$$

where $p = f(r) - f(s)$ and $p_0 = f_0(r) - f_0(s) = 0$.

Moreover, by plugging in $\Omega_1 = 0$, we can integrate Equation (72) to evaluate u_1:

$$\begin{aligned} u_1(r,\theta) =& \int_0^\theta \frac{\partial u_1}{\partial \zeta}\ d\zeta \\ =& -\int_a^b s\ ds \int_0^\theta \sin(\zeta)\cdot W(r,s,\zeta)\ d\zeta \\ =& \frac{\sqrt{\Pi}}{4r}\left[Erf(a-r) - Erf(b-r) + \right. \\ & \left. e^{-r^2\sin^2\theta}(-Erf(a-r\cos\theta) + Erf(b-r\cos\theta))\right] \end{aligned} \tag{78}$$

Following the computations above, we also obtain a simplified order ϵ^2 equation:

$$\begin{aligned} \frac{\partial u_2}{\partial \zeta} + \Omega_2 =& -\sin(\zeta)\int_a^b s\ ds \cdot W'(r,s,\zeta)\cdot(f_1(r) - f_1(s)) \\ & - \cos(\zeta)u_1(r,\zeta)\int_a^b s\ ds\cdot W(r,s,\zeta) \end{aligned} \tag{79}$$

along with

$$u_2(r,0) = u_2(r,2\pi) = 0. \tag{80}$$

Integration of Equation (79) through $[0, 2\pi)$ leads to:

$$\begin{aligned} 2\pi\Omega_2 =& -\int_a^b s\ ds\int_0^{2\pi} \sin\zeta\cdot W'(r,s,\zeta)\cdot[f_1(r) - f_1(s)]\ d\zeta \\ & -\int_a^b s\ ds\int_0^{2\pi}\cos\zeta\cdot W(r,s,\zeta)\cdot u_1(r,\zeta)\ d\zeta \\ :=& G_1 - GF_1 - G_2. \end{aligned} \tag{81}$$

We evaluate the separated double integrals on the right–hand side of equation by setting $W(r,s,\zeta) = e^{-(r^2+s^2)}\exp(2rs\cos\zeta)$, thus

$$\begin{aligned} G_1(r) =& f_1(r)\cdot\int_a^b 2rs^2\cdot e^{-(r^2+s^2)}\ ds\int_0^{2\pi}(\sin\zeta)^2\cdot e^{2rs\cos\zeta}\ d\zeta \\ =& f_1(r)\cdot 2\pi\cdot\int_a^b s\cdot e^{-(r^2+s^2)}\cdot I_1(2rs)\ ds. \end{aligned} \tag{82}$$

Note: $I_1(z)$ is the modified Bessel function of the first kind.

$$\begin{aligned} GF_1(r) =& \int_a^b 2rs^2\cdot e^{-(r^2+s^2)}\cdot f_1(s)\ ds\int_0^{2\pi}(\sin\zeta)^2\cdot e^{2rs\cos\zeta}\ d\zeta \\ =& 2\pi\int_a^b se^{-(r^2+s^2)}\cdot I_1(2rs)\cdot f_1(s)\ ds \end{aligned} \tag{83}$$

$$G_2(r) = \int_a^b \int_0^{2\pi} se^{-(r^2+s^2)} \cdot \cos\zeta \cdot e^{2rs\cos\zeta} \cdot u_1(r,\zeta)\,\mathrm{d}\zeta\,\mathrm{d}s \tag{84}$$

Incorporating this into Equation (81) yields

$$\Omega_2 + \tilde{G}_2(r) = \tilde{G}_1(r) - \tilde{GF}_1(r), \tag{85}$$

where $\tilde{G}_2 = G_2/(2\pi)$, $\tilde{G}_1(r) = G_1/(2\pi)$ and $\tilde{GF}_1 = GF_1/(2\pi)$.

We can then algebraically eliminate Ω_2 in Equation (85) by plugging in $r = a$, which gives

$$\tilde{G}_2(r) - \tilde{G}_2(a) = \tilde{G}_1(r) - \tilde{GF}_1(r) + \tilde{GF}_1(a). \tag{86}$$

To solve this numerically and obtain $f(r)$, we discretize the space domain $[a, b]$ into N equal size bins of size $h = (b-a)/N$ to get a system of N equations with N unknowns $f_{1i}(a+ih)$, where $i = 1, \cdots, N$ (since $f_1(a) = 0$). Following this, we can explicitly evaluate Ω_2 with the solved $f_1(r)$:

$$\Omega_2 = -\tilde{G}_2(a) - \tilde{GF}_1(a). \tag{87}$$

We look at the frequency $\Omega = 1 + \epsilon^2\Omega_2$, and the amount of wave "twist" $f(b) = \epsilon f_1(b)$ as the inner radius a varies between 0 and 4 in Figure 10. The results from the perturbation approximation are very close to the numerics. Recall that $f(r)$ indicates the "twist" in the spiral arm, the approximations even capture the negative region in function $f(r)$.

3.2.3 Smooth coupling

In the previous sections, we have focused on the coupling that is via a Dirac delta function. However, it is possible to numerically simulate neural networks with more physiologically accurate smooth coupling functions and often these results are qualitatively similar to those found for the Dirac delta coupling functions. It would be interesting to check if the rotating wave solution persists for smooth functions. For this reason, we consider a pulse-like coupling function:

$$P(u) = \frac{1}{N(\gamma)} \exp(-\gamma(1-\cos u)), \tag{88}$$

which it is normalized with $N(\gamma)$ such that $\int_0^{2\pi} P(u)\ du = 1$. This scalar term can be computed explicitly as $N(\gamma) = 2\pi \exp(-\gamma) I_0(\gamma)$, which gives $P(u) = 2\pi I_0(\gamma)/\exp(\gamma u)$.

$$\frac{du}{dt} = 1 + K\Delta(u(\mathbf{x}, t)) \int\int W(|\mathbf{x} - \mathbf{x}'|) P(u(\mathbf{x}', t))\ d\mathbf{x}' \tag{89}$$

We return back to the original system Equation (57) with substitution that $R(u) = P(u)$ which gives Equation (89), and simulate the dynamic with Gaussian kernel for a general PRC $\Delta(u) = \sin d - \sin(u + d)$. For the figures, the spatial grid is 101×101 points and an explicit Euler method is used to solve the equation. We get snapshots of the phase-locked patterns and video S11:smoothpulse.mp4 in Supplementary showing that waves rotate rigidly with a constant velocity. Parameter in the pulse-like function Equation (88) is $\gamma = 100$.

It turns out that rotating spiral waves are also solutions to smooth pulse coupling with pure sinusoidal PRC as shown in Figure 11. In addition, it indicates that the "twist" of the wave arm depends on the spatial domain and the parameter d in PRC. We find a larger outer radius b makes more "twists" in the waves and increasing d also increases the twist a little.

When the inner radius a decreases, we see the existence of **spiral chimeras** which consist of an incoherent core surrounded by coherent rotating spiral arms. Coherence or degree of synchrony can be measured by order parameter, more details will be discussed in Chapter 4 Section 4.3.3. The PRC $\Delta(u) = \sin(d) - \sin(u + d)$ has both negative and positive regions indicating different types of responses of neural oscillator stimuli (see Figure 12). Numerical simulations suggest the existence of dynamical patterns including chimera states and full synchronization. In addition to regular chimera as shown in Figure 13 (a) (c), there is chimera as Figure 13 (d) that is wobbling around the core. We find a negative d in PRC introduces instability and the rotating wave disappears and leads to full synchronization as d becomes more negative as in Figure 13 (e) (f). In contrast, when d is positive, rotating waves are more stable as in Figure 13 (b).

Both spatial domain and parameter d affect the behavior of the dynamic, however, the inner radius a for instability is too small compared to our 101×101 grid. We reduce the inner radius a to 0, and only vary parameter d to examine the behavior of spiral waves and chimeras on a disk of radius 5. Figure 14 shows simulations on disk domain of radius 5, and similar dynamics are found on the annulus as shown in Figure 13.

3.3 Discussion

In this chapter, we use perturbation theory and numerical simulations to study the existence of rotating spiral waves on an annulus in a non-locally pulse coupled model. We show that when the pulse coupling is sufficiently weak, it can be averaged to a phase-difference coupling, where the phase-response curve is replaced by the interaction function $H(u)$.

If the pulse coupling is via a Dirac delta function, and the coupling strength decays with respect to a Gaussian kernel, rotating wave solutions can be solved from the equilibria of the system. The entire solution is given by a family of characteristic curves indicating the "twist" of the spiral wave. In the weak coupling scenario, the resulting rotating wave is a straight armed wave if the parameter d in PRC is zero, one can also derive this from the order 0 equation of perturbation approximation. For odd PRC, we also approximate the solution with higher order perturbation terms, and find the function indicating the "twist" of the wave has a negative region.

As we say in the previous chapter, waves that occur in a ring lose stability as the length of the ring decreases. This suggests that there may be a limit to the size of the hole in the annulus such that the rotating waves are stable. To explore the pulse coupling on the 2-dimensional region, we simulate the system with a smooth pulse-like influence function and observe that both the geometry domain and the parameter in PRC affect the "twist" in the wave. In addition to regular rotating waves, we also observed the emergence of chimera states.

Nevertheless, from a mathematical perspective, very little analytical progress can be made with systems having smooth pulse coupling functions. To understand the origin of spiral wave chimeras, a practical attempt is to assume weak coupling $K \ll 1$ and reduce the system into a relatively easier representation as discussed at the beginning of this chapter which is a phase-difference system. This is what will be discussed in Chapter 4.

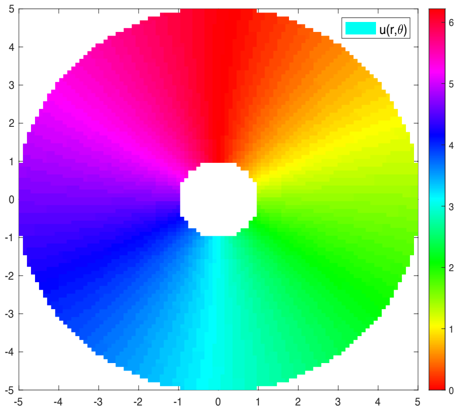

(a) $K = 0.1$, $a = 1$, $b = 5$, $d = 0$

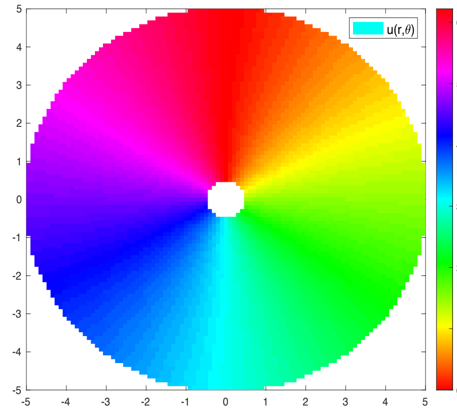

(b) $K = 0.1$, $a = 0.5$, $b = 5$, $d = 0$

(c) $K = 1$, $a = 0.5$, $b = 5$, $d = 0$

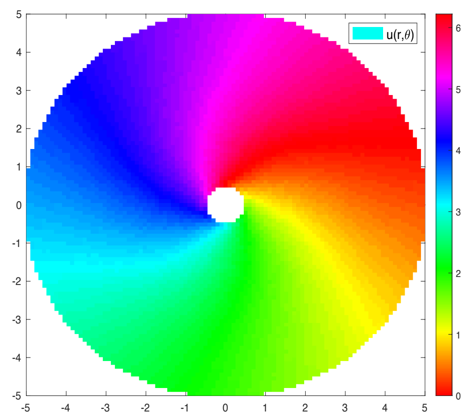

(d) $K = 0.1$, $a = 0.5$, $b = 5$, $d = 0.4$

Figure 9: Wave solutions with different parameters. Panel (a) and (b): straight wave due to weak coupling where the connecting strength is small; Panel (c) : twisted spiral wave when connecting strength is large; Panel (d): twisted spiral wave in weak coupling with a non-zero parameter $d = 0.4$.

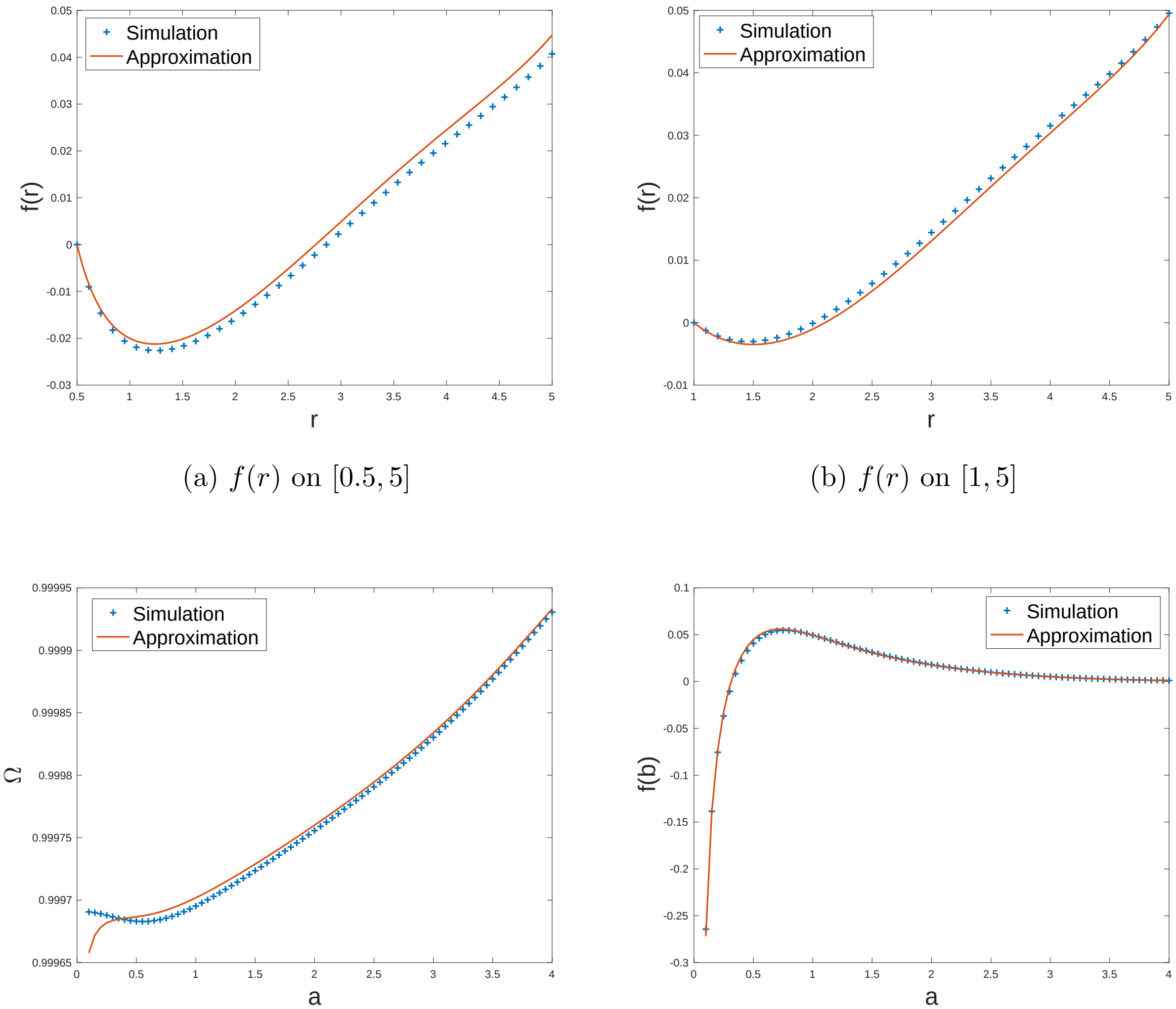

(a) $f(r)$ on $[0.5, 5]$

(b) $f(r)$ on $[1, 5]$

(c) Ω vs a

(d) $f(b)$ vs a

Figure 10: Comparison of the perturbation approximation (thin line) with the numerically solved Ω and $f(r)$ (crosses) using odd PRC $\Delta(u) = -\sin(u)$. (a) (b): $f(r) = \epsilon f_1(r)$ compared to directly solved solution from full system Equation (64); (c) (d): Fix the outer radius $b = 5$, vary a and compare approximated Ω and $f(b)$ to numerically solved results from Equation (86) and Equation (87).

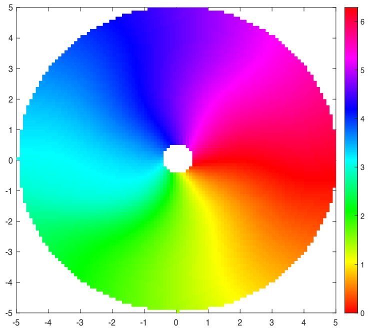

(a) $K = 1$, $a = 0.5$, $b = 5$, $d = 0$

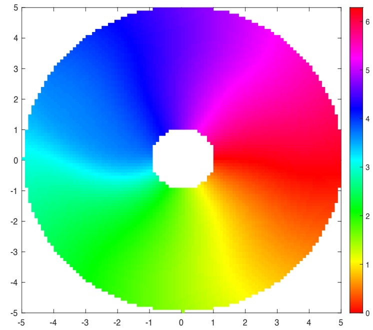

(b) $K = 1$, $a = 1$, $b = 5$, $d = 0$

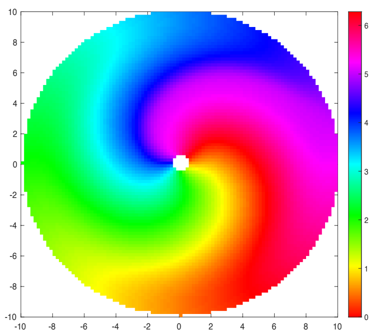

(c) $K = 1$, $a = 0.5$, $b = 10$, $d = 0$

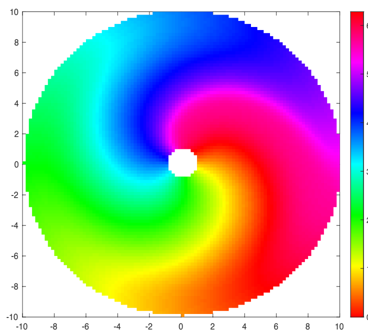

(d) $K = 1$, $a = 1$, $b = 10$, $d = 0$

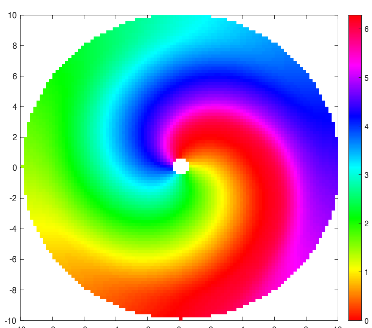

(e) $K = 1$, $a = 0.5$, $b = 10$, $d = 0.4$

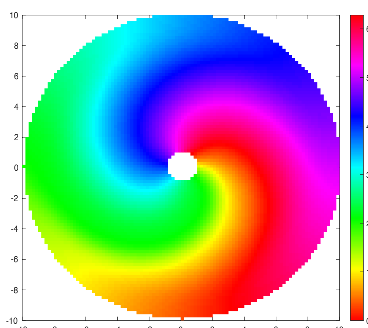

(f) $K = 1$, $a = 1$, $b = 10$, $d = 0.4$

Figure 11: Simulations of the full system with initial condition $u(r, \theta) = \theta$, which is the straight-armed wave. Panel (a) (b) (c) (d): Smooth pulse coupling with pure sinusoidal PRC on different domain region; Panel (e) (f) : Smoothing pulse coupling with non-zero d in PRC function.

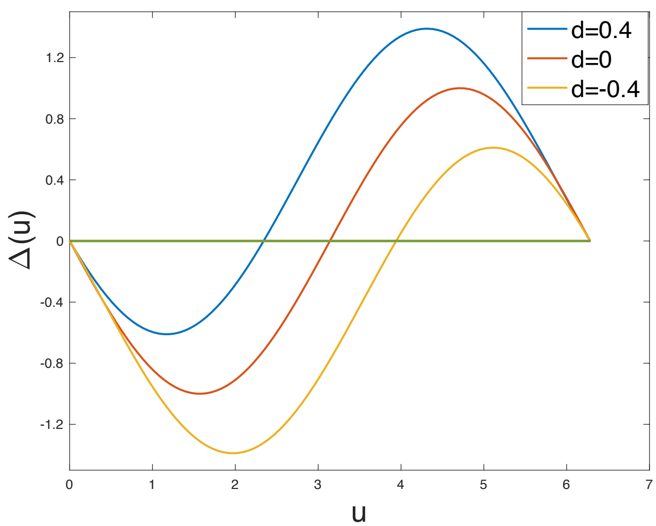

Figure 12: PRC $\Delta(u) = \sin(d) - \sin(u + d)$ with parameters $d = 0.4, 0, -0.4$. Negative d introduces more negative region of the PRC thus leads to instability.

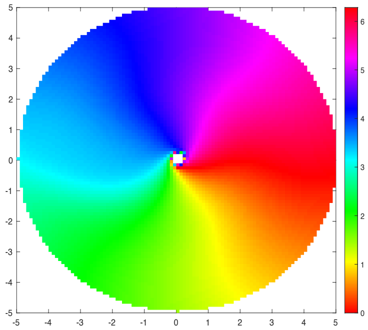

(a) $K = 1$, $a = 0.2$, $b = 5$, $d = 0$

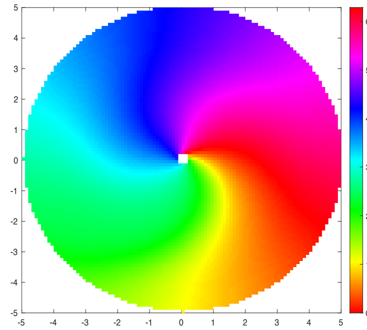

(b) $K = 1$, $a = 0.2$, $b = 5$, $d = 0.4$

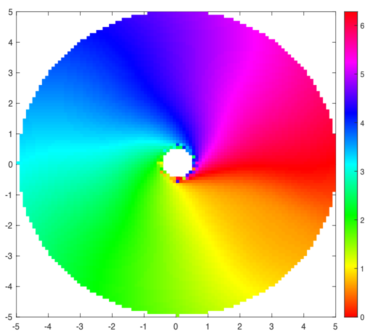

(c) $K = 1$, $a = 0.5$, $b = 5$, $d = -0.4$

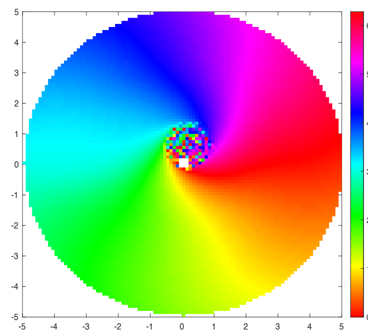

(d) $K = 1$, $a = 0.2$, $b = 5$, $d = -0.4$

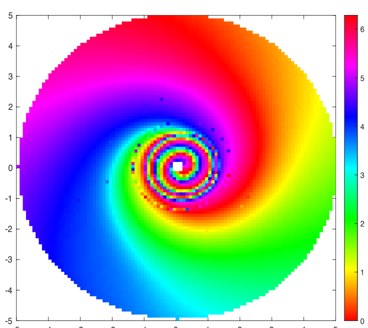

(e) $K = 1$, $a = 0.2$, $b = 5$, $d = -0.8$, earlier

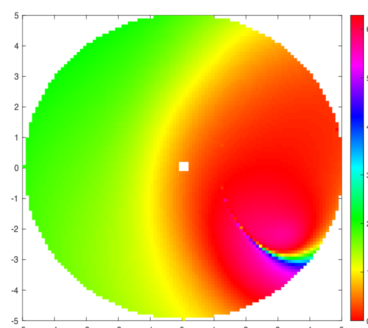

(f) $K = 1$, $a = 0.2$, $b = 5$, $d = -0.8$, later

Figure 13: Screenshots of spiral chimera and synchronization on the annulus. Panel (b): stable rotating spiral wave pattern; Panel (a) (c) (d): spiral chimera generated around the core; Panel (e) (f): loss of stability, rotating spiral wave breaks up to spiral chimera and finally goes to a fully synchronized state.

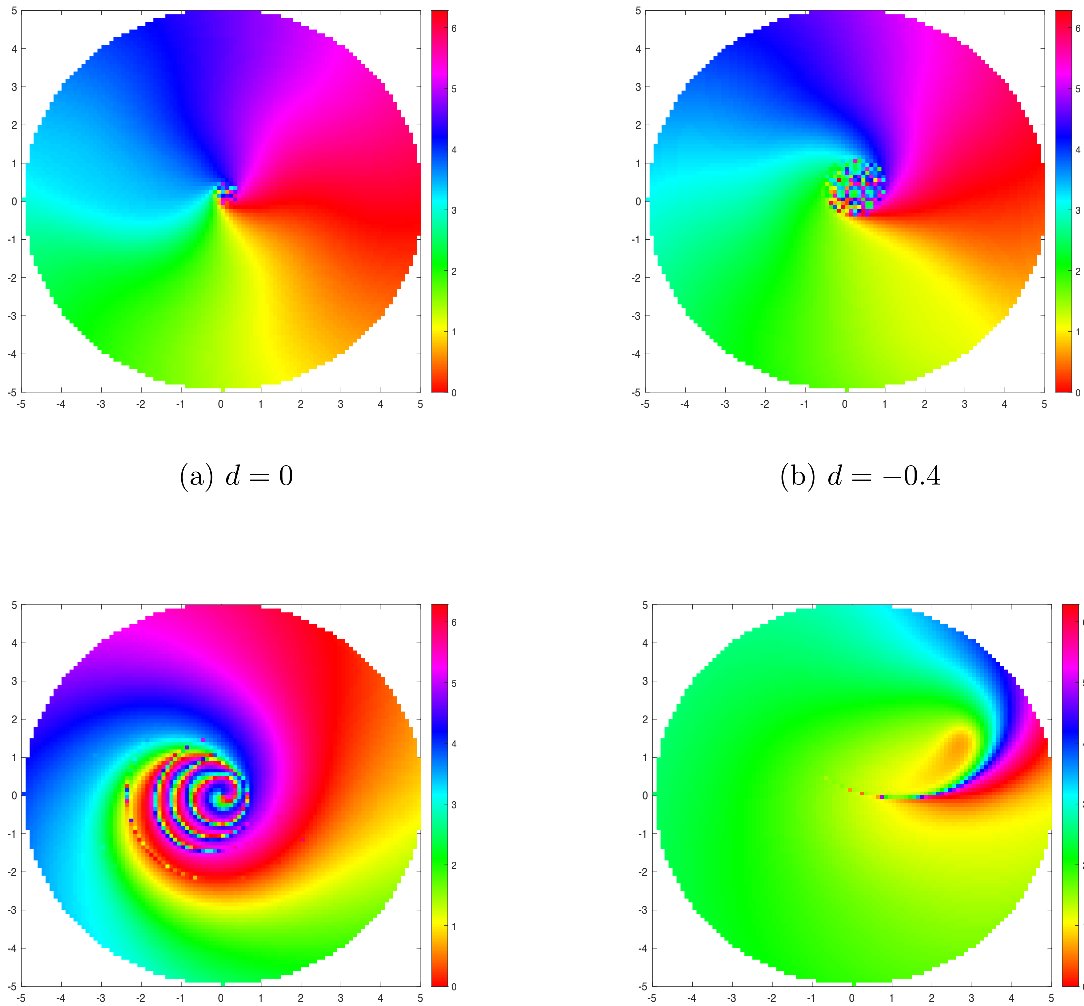

(a) $d = 0$

(b) $d = -0.4$

(c) $d = -0.8$, earlier stage

(d) $d = -0.8$, later stage

Figure 14: Screenshots of spiral chimera and synchronization on disk. Panel (a) (b) : spiral chimera generated around the core; Panel (c) (d) : loss of stability, rotating spiral wave breaks up to spiral chimera and finally goes to a fully synchronized state.

4.0 Phase-difference Coupling on Annulus

4.1 Derivation of Model Equations

Let A be some domain in the plane representing a part of the cortex and suppose that at each point in space there is a local circuit that is intrinsically oscillatory with period P. For the present chapter, we assume that the frequency is the same at every spatial point in A. For simplicity of exposition, we consider a single excitatory population of neurons that is intrinsically oscillatory:

$$\begin{aligned} C\frac{\partial V(\mathbf{x},t)}{\partial t} &= I_0 - I_{ion}(V(\mathbf{x},t), n(\mathbf{x},t)) - g_{syn}(\mathbf{x},t)(V(\mathbf{x},t) - V_{syn}) \\ \tau_n(V(\mathbf{x},t))\frac{\partial n(\mathbf{x},t)}{\partial t} &= n_\infty(V(\mathbf{x},t)) - n(\mathbf{x},t) \\ \tau_s(V(\mathbf{x},t))\frac{\partial s(\mathbf{x},t)}{\partial t} &= s_\infty(V(\mathbf{x},t)) - s(\mathbf{x},t) \end{aligned}$$

where $V(\mathbf{x},t)$ is the potential of the neuron at location $\mathbf{x}$, $n(\mathbf{x},t)$ is an ionic gating variable for the neuron at $\mathbf{x}$ (there can be many such variables and we only write one here for conciseness), and $s(\mathbf{x},t)$ is the synaptic gating variable for the neuron at $\mathbf{x}$. (See [22] for detailed descriptions of this type of model. For the present scenario, it suffices to know that if there is a sufficient drive, I_0, these models will typically generate limit cycle behavior.) The function $g_{syn}(\mathbf{x},t)$ governs the coupling and has the form:

$$g_{syn}(\mathbf{x},t) = G_{syn}\int_A W(|\mathbf{x}-\mathbf{x}'|^2)s(\mathbf{x}',t)\ d\mathbf{x}'$$

where the kernel $W(|\mathbf{x}|^2)$ describes the distance-dependent strength of interactions between neurons. We assume in isolation that each neuron is undergoing an asymptotically stable $P-$periodic orbit, $(V_0(t), n_0(t), s_0(t))$. For G_{syn} sufficiently small, we can formally reduce the network to a system of phase equations, where $V(\mathbf{x},t) = V_0(u(\mathbf{x},t))$ and $u(\mathbf{x},t)$ satisfies

$$H(u) = (G_{syn}/C)(1/P)\int_0^P Z_0(t')(V_{syn} - V_0(t'))s_0(t'+u)\ dt'.$$

The function $Z_0(t)$ is the voltage component infinitesimal phase-resetting curve (iPRC) of the isolated limit cycle [65]. The iPRC can be estimated experimentally [64] for single neurons and also can be readily computed by numerically solving an associated linear equation [65] for the particular model of interest. Once the iPRC is computed, the interaction function $H(u)$ is computed by convolving it with the synaptic profile. In order to assure that the coupling enforces stable synchronization, we assume that $H'(0) > 0$ (see Section 4.2.1). To avoid boundary effects, we also assume that $H(0) = 0$. Finally, we assume that the coupling kernel is non-negative, $W(|\mathbf{x}|^2) \geq 0$.

Equation (90) can be reduced to a phase equation of the form:

$$\frac{\partial u(\mathbf{x},t)}{\partial t} = \omega + \int_A W(|\mathbf{x}-\mathbf{x}'|^2)H(u(\mathbf{x}',t) - u(\mathbf{x},t))\ d\mathbf{x}', \tag{90}$$

where $u(\mathbf{x},t)$ is the phase of the oscillator at a point $\mathbf{x} \in A$, the annular domain. The function, $H(u)$ is $2\pi-$periodic and $W(|\mathbf{x}|^2)$ is a symmetric coupling kernel. We focus on the annulus as this symmetry enables us to reduce the dimensionality of the problem. As the inner radius of the annulus decreases, we will be left with a disk. (Note that for later notational reasons, we have written the kernel as a function of the distance squared. Thus, for example, $W(R) = e^{-R}$ is a Gaussian where $R = |\mathbf{x}|^2$.) If we regard the hole in the annulus as a region of tissue that has been excised, then, the connectivity across the hole will be disrupted making the analysis much more difficult. Instead, we regard hole as a region of tissue where the cells are less excited (non-oscillating), but the connections across the hole are still able to transmit signals.

4.2 General Theory and Derivations

4.2.1 Phase-locking and stability of synchrony

We say that there is a *phase-locked* solution to Equation (90) if there is a solution of the form:

$$u(\mathbf{x},t) = \Omega t + \Upsilon(\mathbf{x})$$

where

$$\Omega = \omega + \int_A W(|\mathbf{x}-\mathbf{x}'|^2)H(\Upsilon(\mathbf{x}') - \Upsilon(\mathbf{x}))\ d\mathbf{x}'.$$

Such a solution is never unique as one can always add a constant to $\Upsilon(\mathbf{x})$ and have it still solve the equation. Thus, one typically takes a specific point in the domain, $\mathbf{x}_0$, and sets $\Upsilon(\mathbf{x}_0) = 0$. Then, $\Upsilon(\mathbf{x})$ becomes the phase relative to the point $\mathbf{x}_0$. Clearly if $H(0) = 0$, then $u(\mathbf{x}, t) = \omega t$ (synchrony) is always a phase-locked solution to Equation (90). Since A is a finite annulus, points near the inner and outer radii will receive a different amount of input than points in the interior of the annulus. Thus, if $H(0)$ is nonzero, we cannot expect a homogeneous synchronous solution; hence we will assume $H(0) = 0$. The linearization about synchrony leads to the equation:

$$\frac{\partial v(\mathbf{x}, t)}{\partial t} = H'(0) \int_A W(|\mathbf{x} - \mathbf{x}'|^2)[v(\mathbf{x}', t) - v(\mathbf{x}, t)]\; d\mathbf{x}'.$$

Since $H'(0) > 0$ and $W(|\mathbf{x}|^2) > 0$, it follows immediately from Theorem 2.3 in [23] that synchrony is stable.

4.2.2 Rotating waves on annulus

We now turn to the main part of this chapter where we consider rotating waves in the annulus. If we write $\mathbf{x} = (x, y)$ and $\mathbf{x}' = (x', y')$ and convert to polar coordinates:

$$\begin{aligned} x &= r\cos(\theta), & x' &= s\cos(\theta + \phi), \\ y &= r\sin(\theta), & y' &= s\sin(\theta + \phi). \end{aligned}$$

The squared distance between them is

$$(x - x')^2 + (y - y')^2 = r^2 + s^2 - 2rs\cos\phi.$$

Since the kernel W is symmetric and only dependent on the distance of oscillators, we can write it as a function of r, s, and ϕ,

$$\begin{aligned} W(|\mathbf{x} - \mathbf{x}'|^2) &= W(r^2 + s^2 - 2rs\cos\phi) \\ &= W((r-s)^2 + 2rs(1 - \cos\phi)) \\ &= W((r-s)^2 + 4rs\sin^2(\phi/2)). \end{aligned}$$

We remark that the three different ways of writing the argument of the kernel are identical but will make some calculations simpler in what follows. We can now write Equation (90) as:

$$\frac{\partial u(r,\theta,t)}{\partial t} = \int_a^b s\,\mathrm{d}s \int_{-\pi}^{\pi} W(r^2+s^2-2rs\cos\phi)H(u(s,\theta+\phi,t)-u(r,\theta,t))\,\mathrm{d}\phi. \tag{91}$$

where a and b are the inner and outer radii of the annulus respectively and we have set $\omega = 0$ with no loss in generality. (We can just replace u in Equation (90) with $u + \omega t$ and thus remove ω.)

4.2.2.1 Rotating waves

In general, $N-$armed rotating waves have the form,

$$u(r,\theta,t) = U_N(r, \Omega_N t + N\theta),$$

where $N = 0, \pm 1, \pm 2, \ldots$ and $U_N(r,\xi)$ is a function of r and $\xi = \Omega_N t + N\theta$ satisfying:

$$\Omega_N \frac{\partial U_N}{\partial \xi} = \int_a^b s\,\mathrm{d}s \int_{-\pi}^{\pi} W(r^2+s^2-2rs\cos\phi)H(U_N(s,\xi+N\phi)-U_N(r,\xi))\,\mathrm{d}\phi. \tag{92}$$

Since U_N is a phase variable, we require that $U_N(r,\xi+2\pi) = U_N(r,\xi)+2\pi$, that is, U_N increases by 2π for each cycle when $N \neq 0$. Because of the simple form for phase models, we can reduce the dimension of this integro-differential equation further by seeking solutions of the form:

$$U_N(r,\xi) = \xi + f_N(r) = \Omega_N t + N\theta + f_N(r). \tag{93}$$

To set the phase, we additionally assume that $f_N(a) = 0$. The lines $\xi + f_N(r) = C$ are the lines of constant phase for the rotating wave. Such a solution satisfies

$$\Omega_N = \int_a^b s\ ds \hat{W}_N(r,s,f_N(s)-f_N(r)), \tag{94}$$

where

$$\hat{W}_N(r,s,\chi) = \int_{-\pi}^{\pi} W(r^2+s^2-2rs\cos\phi)H(N\phi+\chi)\ d\phi. \tag{95}$$

If we can explicitly find the function, $\hat{W}_N$, then Equation (94) is a nonlinear integral equation for $f_N(r)$ that can be solved numerically by discretizing in r. For the bulk of the chapter, we will assume that $N = 1$, so, for notational simplicity, if there is no subscript, N, then $N = 1$.

4.2.3 Stability of rotating waves

Recall the rotating wave solutions Equation (93) where $U_N(r,\theta,t) = \Omega_N t + N\theta + f_N(r)$. We can linearize Equation (91) about Equation (93) to formulate the stability problem:

$$\frac{\partial v}{\partial t} = \int_a^b sds \int_{-\pi}^{\pi} d\phi W(r^2+s^2-2rs\cos\phi)H'(f_N(s)-f_N(r)+N\phi)[v(s,\theta+\phi,t)-v(r,\theta,t)]. \tag{96}$$

Note that the equation for v is homogeneous in t and also a homogeneous convolution with respect to θ. Thus, we can look for solutions of the form:

$$v(r,\theta,t) = \exp(\lambda_m t)\exp(im\theta)\psi_m(r),\ m \in \mathbb{Z}, \tag{97}$$

which leads to the following linear integral equation:

$$\lambda_m \psi_m(r) = \int_a^b A_N^m(r,s)\psi_m(s)\ ds - \psi_m(r)\int_a^b A_N^0(r,s)\ ds, \tag{98}$$

$$A_N^m(r,s) = s\int_{-\pi}^{\pi} W(r^2+s^2-2rs\cos\theta)H'(f_N(s)-f_N(r)+\phi)e^{im\phi}\ d\phi. \tag{99}$$

We note that if $m = 0$, then $\lambda_0 = 0$ is an eigenvalue with eigenvector, $\psi(r) = 1$, corresponding to a rigid rotation of the radial wave. For each m, we can discretize the integrals and numerically estimate the eigenvalues for given choices for $H(u)$ and kernels, W which will be discussed later in Section 4.3. In that section, we derive some sufficient conditions on A_N^m for stability.

4.2.4 Odd coupling and linear stability of the radial rotating wave

When $H(u)$ is an odd periodic function, the solutions to Equation (94) are particularly simple, namely, $U_N(r,\xi) = N\xi$. We call these *radial* rotating waves since the contours of constant phase are just radial lines.

Lemma 4.2.1. *Suppose that $H(u)$ is an* odd *periodic function. Then $\Omega_N = 0$ and $f_N(r) = 0$.*

Proof. Since $H(u)$ is an odd function and $W(r^2 + s^2 - 2rs\cos\phi)$ is an even function of ϕ, $\hat{W}_N(r,s,0) = 0$. Thus, $\Omega_N = 0$ and the solution is a rotating wave: $u(r,\theta,t) = N\theta$. □

We *now* focus on the one-armed rotating wave; thus we will drop the subscripts since $N = 1$. We have shown that Equation (91) has a radial rotating solution, $u_0(r,\theta,t) = \theta + C$ when $H(u)$ is an odd periodic function, so it is natural to examine the stability. The linearized equation about u_0 is Equation (98) with $N = 1$, and according to Lemma 4.2.1, $A^m(r,s)$ in Equation (99) is equal to $sK_m(r,s)$ where:

$$K_m(r,s) = \int_{-\pi}^{\pi} W(r^2 + s^2 - 2rs\cos\theta)H'(\phi)\cos(m\phi)\ d\phi. \tag{100}$$

We note that since $H(u)$ is odd, this means that $H'(u)$ is even so that $W(r^2 + s^2 - 2rs\cos\theta)H'(\phi)\sin(m\phi)$ is an odd periodic function of ϕ and thus its integral over a period vanishes.

We now prove a sufficient condition for stability; we assume that $m > 0$.

Theorem 4.2.2. *Suppose*

$$|K_m(r,s)| < K_0(r,s), \quad \forall\ (r,s) \in [a,b] \times [a,b] \tag{101}$$

then $\Re(\lambda_m) < 0$.

Proof. To prove this, we use the idea from the Gershgorin circle theorem for matrices:

$$\begin{aligned} \textit{Equation } (98) \Leftrightarrow \left(\lambda_m + \int_a^b sK_0(r,s)\,\mathrm{d}s\right)\psi(r) &= \int_a^b s\,\mathrm{d}sK_m(r,s)\psi(s) \\ \implies \left|\lambda_m + \int_a^b sK_0(r,s)\,\mathrm{d}s\right| \cdot |\psi(r)| &= \left|\int_a^b s\,\mathrm{d}sK_m(r,s)\psi(s)\right| \\ &\le \int_a^b s|K_m(r,s)| \cdot |\psi(s)|\,\mathrm{d}s. \end{aligned}$$

Choose r such that $\psi(r) = \max_s |\psi(s)|$, so that

$$\left| \lambda_m + \int_a^b sK_0(r,s)\,\mathrm{d}s \right| \le \int_a^b s|K_m(r,s)|\,\mathrm{d}s, \qquad \forall r,$$

$0 \le |K_m(r,s)| < K_0(r,s) \;\Rightarrow\; \Re(\lambda_m) < 0.$ $\square$

Remarks

1. We can improve on this stability estimate by noting that the eigenvalues are actually bounded by the integrals. Thus, if

$$\int_a^b sK_0(r,s)\;ds > \int_a^b s|K_m(r,s)|\;ds, \quad \forall r \in (a,b), \tag{102}$$

then we can also conclude stability. However, in practice, these integrals cannot be explicitly found and we must evaluate them numerically, so that the condition in Theorem 4.2.2 is much easier to check.

2. Here we have addressed the point spectrum. However, one might ask about the continuous spectrum. Suppose that

$$\int_a^b sK_0(r,s)\;ds > 0,$$

then it follows from Lemma 2.4 in [23] that the continuous spectrum lies in the left-half complex plane.

Later in this section, we consider the narrow annulus assumption where $0 < b-a = \delta \ll 1$ and we derive:

$$\lambda_m = a\delta(K_m(a,a) - K_0(a,a)) + O(\delta^2). \tag{103}$$

λ_m will be negative when $K_0(a,a) > K_m(a,a)$ which is the same bound as Equation (101) applied at $r = s = a$.

Theorem 4.2.3. *Suppose that $W(0) > 0$, $H(u)$ is odd and $H'(0) > 0$. Then the rotating wave, $U(r,\theta,t) = \theta$ is unstable if a, b are sufficiently small.*

Proof. Since $H(u)$ is a periodic function we can write:

$$H(u) = \sum_{n=0}^{\infty} a_n \cos(nu) + b_n \sin(nu).$$

The assumption that $H'(0) > 0$ implies that there is at least one $n = p$ such that $b_p > 0$. By definition:

$$K_m(a,a) = \int_{-\pi}^{\pi} W(2a^2(1-\cos\phi))H'(\phi)\cos m\phi \; d\phi.$$

For a near 0, $W(2a^2(1-\cos\phi)) = W(0) + O(a^2)$, so that

$$K_0(a,a) = O(a^2)$$

and

$$K_p(a,a) = \frac{1}{2}W(0)b_p + O(a^2) > 0.$$

Thus a, δ can be chosen small enough so that $\lambda_p > 0$ in Equation (103) and we have shown instability. $\square$

This demonstrates that there are at least some annuli which do not admit stable rotating waves.

4.2.5 General coupling

Having established that there exists rotating wave solutions for odd coupling, we now prove that rotating waves can exist for general coupling. We will focus on the one-armed solutions, $N = 1$ to Equation (94). We show via continuation that we can find a solution in the general coupling case.

Theorem 4.2.4. *We write $H(u) = h(u,p)$ where p is a parameter and consider:*

$$\Omega = \int_a^b s \; ds \int_{-\pi}^{\pi} W(r^2 + s^2 - 2rs\cos\phi)h(f(s) - f(r) + \phi, p) \; d\phi. \tag{104}$$

Let $\Omega_0, p_0, f_0(r)$ be a solution to Equation (104) with $f_0(a) = 0$. Let $h_u(u,p)$ denote the derivative of h with respect to u and suppose that:

$$g_0(r,s) := \int_{-\pi}^{\pi} W(r^2 + s^2 - 2rs\cos\phi)h_u(\phi + f_0(s) - f_0(r), p_0) \; d\phi > 0$$

for all $(r,s) \in [a,b] \times [a,b]$. Then, there exists an interval $p_1 < p_0 < p_2$ such that there is a locally unique branch of solutions to Equation (94).

Proof. We wish to find $(f(r), \Omega)$ with $f(a) = 0$ such that:

$$\Omega = \int_a^b s\ ds \hat{W}(r, s, f(s) - f(r), p) \tag{105}$$

where

$$\hat{W}(r, s, \chi, p) = \int_{-\pi}^{\pi} W(r^2 + s^2 - 2rs\cos\phi) h(\phi + \chi, p)\ d\phi.$$

Since Ω is independent of r, we see that, in particular

$$\Omega = \int_a^b s\ ds \hat{W}(a, s, f(s), p)$$

since $f(a) = 0$. We rewrite Equation (105) as a nonlinear operator

$$Q(p, f(r)) := \int_a^b s\ ds[\hat{W}(r, s, f(s) - f(r), p) - \hat{W}(a, s, f(s))] = 0$$

in the Banach space of continuous functions $f(r)$ on $[a, b]$ with $f(a) = 0$. We assume that $Q(p_0, f_0(r)) = 0$. The Frechet derivative of Q with respect to f is:

$$(Lf)(r) := \int_a^b s g_0(r, s)[f(s) - f(r)]\ ds - \int_a^b s g_0(a, s) f(s)\ ds. \tag{106}$$

Since $g_0(r, s) > 0$ by hypothesis, it follows from Lemma 2.1 in [23] that the only solution to $Lf = 0$ satisfying $f(a) = 0$ is $f(r) = 0$ for all $r \in [a, b]$. Thus, we can apply the implicit function theorem from which the conclusion of the theorem holds. □

In particular, since we know that there is a solution to Equation (105), when $H(u)$ an odd function, namely, $u = \theta$, we can write:

$$h(u, p) = H_o(u) + pH_e(u),$$

where H_o and H_e are the odd and even parts of the general $H(u)$. If we assume

$$g(r, s) = \int_{-\pi}^{\pi} W(r^2 + s^2 - 2rs\cos\phi) H_o'(\phi)\ d\phi > 0,$$

then we immediately obtain the existence of solutions for $|p|$ sufficiently small. For example, if $W(z) = \exp(-z)$ and $H_o(u) = \sin(u)$, then

$$g(r, s) = 2\pi \exp(-r^2 - s^2) I_1(2rs),$$

which is positive for any $0 < a \le r, s \le b$. Thus, for $H(u) = \sin(u+d) - \sin(d)$, solutions exist for d sufficiently small.

As is often the case with the implicit function theorem, it suggests a linear approximation for small p. Let

$$\begin{aligned} g_o(r,s) &= \int_{-\pi}^{\pi} W(r^2+s^2-2rs\cos\phi)H_o'(\phi)\ d\phi, \\ F_e(r) &= \int_a^b s\ ds \int_{-\pi}^{\pi} W(r^2+s^2-2rs\cos\phi)H_e(\phi)\ d\phi. \end{aligned}$$

Then, we must solve the linear equation for $f(r)$ with $f(a) = 0$,

$$\int_a^b s[g_o(r,s) - g_o(a,s)]f(s)\ ds - f(r)\int_a^b sg_o(r,s)\ ds = F_e(a) - F_e(r). \tag{107}$$

The assumption that $g_o(r,s) > 0$ assures that this equation is invertible and that we can solve for $f(r)$. We additionally find:

$$\Omega \approx p\int_a^b sg_o(a,s)f(s)\ ds + F_e(a). \tag{108}$$

While the linear system is presumably easier to solve than the nonlinear integral Equation (94), it still must be done numerically, and still involves discretizing the integral equation. In the next two sections, we introduce two approximations that allow us to get a good handle on the dependence of Ω and $f(r)$ on parameters as well as the stability when $H(u)$ is not an odd function.

Recall the linearized equation Equation (96), we formulate the stability problem as Equation (98). Note that when H is odd and $f(r) = 0$, then $A^m(r,s) = sK_m(r,s)$ c.f. Equation (99). The proof of Theorem 4.2.2 can be mimicked to prove the following corollary which provides a sufficient condition for linear stability when $H(u)$ is not odd.

Corollary 4.2.4.1. *Suppose*

$$|A^m(r,s)| \le A^0(r,s), \quad \forall\ (r,s) \in [a,b]\times[a,b]$$

then $\Re\lambda_m < 0$.

These conditions are not terribly practical, but as we will see in the next section, they can be estimated.

4.2.6 Narrow annulus approximation

In the next two subsections (the "narrow annulus" Section 4.2.6, here, and the "big hole" Section 4.2.7 subsequently), we make some assumptions on the geometry of the annulus in order to gain some more analytic insight into both the form of the solutions and their stability.

Let $\delta = b - a$ denote the difference between the outer and inner radii of the annulus. Define:

$$\begin{aligned} B^0(r,s) &= s\int_{-\pi}^{\pi} W(r^2+s^2-2rs\cos\phi)H(\phi)\ d\phi, \\ B^1(r,s) &= s\int_{-\pi}^{\pi} W(r^2+s^2-2rs\cos\phi)H'(\phi)\ d\phi. \end{aligned} \tag{109}$$

Then

$$\Omega = \delta B^0(a,a) + \frac{\delta^2}{2}\left[B_s^0(a,a) + B_r^0(a,a)\right] + O(\delta^3), \tag{110}$$

$$f(r) = \frac{B_r^0(a,a)}{B^1(a,a)}(r-a) + O(\delta^2) \tag{111}$$

Additionally, if $H(u)$ is odd, then the eigenvalues for the linearized system are:

$$\lambda_m = \delta\left(\frac{bK_m(a,b)+aK_m(b,a)}{2} - \frac{bK_0(a,b)+aK_0(b,a)}{2}\right) + O(\delta^3) \tag{112}$$

where $K_m(r,s)$ is defined by Equation (100).

We now verify these approximations in detail by making a change of variables in which we rescale r by the parameter, $\delta = b-a$ which we assume to be small. We seek solutions to Equation (94) with $N=1$ (for simplicity). Let $r = a+\delta x$ and $s = a+\delta y$ and $B^0(r,s), B^1(r,s)$ be given by Equation (109). For a thin annulus ($\delta \ll 1$), we expect that $f(r) \equiv f(a+\delta x)$ will be $O(\delta)$ since $f(a)=0$ by convention. Thus, to order δ, we write $f(s)-f(r) = \delta f_1(y-x) + O(\delta^2)$ with f_1 an unknown constant. Then, $H(\phi + f(s) - f(r)) = H(\phi) + \delta H'(\phi) f_1(y-x) + O(\delta^2)$. With the rescaling of r, s, we also have:

$$B^0(r,s) = B^0(a,a) + \delta\left[B_r^0(a,a)x + B_s^0(a,a)y\right] + O(\delta^2),$$

where $B_z^0(a,a)$ means the partial derivative of $B^0(r,s)$ with respect to $z \in \{r,s\}$ evaluated at $r=s=a$. Let $\Omega = \delta\Omega_0 + \delta^2\Omega_1 + O(\delta^3)$. Then Equation (94) can be written as:

$$\begin{aligned} \delta\Omega_0 + \delta^2\Omega_1 &= \delta \int_0^1 B^0(a,a)\ dy \\ &+ \delta^2 \left[\int_0^1 B_r^0(a,a)x + B_s^0(a,a)y + B^1(a,a)f_1(y-x)\ dy \right] + O(\delta^3). \end{aligned}$$

Gathering terms of equal powers of δ, we obtain:

$$\Omega_0 = B^0(a,a) = a \int_{-\pi}^{\pi} W(2a^2(1-\cos\phi))H(\phi)\ d\phi. \tag{113}$$

For the next order:

$$\Omega_1 = xB_r^0(a,a) + \frac{1}{2}B_s^0(a,a) + B^1(a,a)f_1(\frac{1}{2}-x). \tag{114}$$

This expression must be true for all $x \in [0,1]$, so that we match the coefficients of x to get f_1:

$$f_1 = \frac{B_r^0(a,a)}{B^1(a,a)}. \tag{115}$$

This expression is well-defined as long as $B^1(a,a) \neq 0$. However, this requirement is exactly the assumption that we need to continue solutions from any starting solution (see Theorem 4.2.4). Since $f(r) = f(a) + f_1(r-a) + O(\delta^2)$ and $f(a) = 0$, we obtain the approximation, Equation (111). We obtain Ω_1 by setting $x = \frac{1}{2}$ in Equation (114):

$$\Omega_1 = \frac{1}{2}\left[B_s^0(a,a) + B_r^0(a,a)\right], \tag{116}$$

and thus:

$$\Omega = \delta B^0(a,a) + \frac{\delta^2}{2}\left[B_s^0(a,a) + B_r^0(a,a)\right] + O(\delta^3). \tag{117}$$

This is the result desired in Equation (110). If we define

$$\omega(a,b) = \frac{\delta}{2}\left[B^0(a,b) + B^0(b,a)\right], \tag{118}$$

we see that

$$\omega(a, a+\delta) = \Omega + O(\delta^3),$$

thus, Equation (118) is a convenient approximation for the frequency for $b-a$ small. This simple expression has the advantage of not requiring any differentiation. We emphasize that it is only good for $b-a$ small.

We now turn to the stability question. Recall the linearized eigenvalue problem with general coupling shown in Equation (96). Let $A_z^m(r,s)$ denote the partial derivative of $A^m(r,s)$ with respect to $z \in \{r,s\}$. We now make $\delta = b-a$ be a small positive number and again let $r = a+\delta x$, $s = a+\delta y$, and $\lambda_m = \delta\gamma$. Then Equation (98) can be written as:

$$\gamma\psi(r) = \int_0^1 A^m(r,s)\psi(s)\ dy - \psi(r)\int_0^1 A^0(r,s)\ dy, \tag{119}$$

where for simplicity of notation, we keep the r,s without yet expanding. We make the normalization assumption that $\psi(a)=1$ for the eigenvector. We expand $\gamma, \psi, A^m(r,s)$ in a series in δ:

$$\begin{aligned} \psi(r) &= 1+\delta\psi_1 x + O(\delta^2), \\ \gamma &= \gamma_0 + \delta\gamma_1 + O(\delta^2), \\ A^m(r,s) &= A^m(a,a) + \delta x A_r^m(a,a) + \delta y A_s^m(a,a) + O(\delta^2). \end{aligned}$$

To lowest order we obtain:

$$\gamma_0 = A^m(a,a) - A^0(a,a). \tag{120}$$

We note that $A^m(a,a) = aK_m(a,a)$ from Equation (99) when $f(r)=0$. To order δ, we obtain:

$$\begin{aligned} \gamma_0 x\psi_1 + \gamma_1 &= xA_r^m(a,a) + \frac{1}{2}A_s^m(a,a) + \frac{1}{2}A^m(a,a)\psi_1 \\ &- \left(xA_r^0(a,a) + \frac{1}{2}A_s^0(a,a) + x\psi_1 A^0(a,a)\right). \end{aligned}$$

This must be true for all $x \in [0,1]$, so that we find that:

$$\gamma_0\psi_1 = A_r^m(a,a) - A_r^0(a,a) - A^0(a,a)\psi_1.$$

Using the definition of γ_0, we obtain:

$$\psi_1 = \frac{A_r^m(a,a) - A_r^0(a,a)}{A^m(a,a)}. \tag{121}$$

From this, we readily get:

$$\gamma_1 = \frac{1}{2}\left(A_s^m(a,a) - A_s^0(a,a) + A_r^m(a,a) - A_r^0(a,a)\right). \tag{122}$$

Thus, we now have an expression for the eigenvalue for small δ:

$$\lambda_{TA} = \delta[A^m(a,a) - A^0(a,a)] + \frac{\delta^2}{2}\left(A_s^m(a,a) - A_s^0(a,a) + A_r^m(a,a) - A_r^0(a,a)\right) \tag{123}$$

We can write the eigenvalue compactly by defining the following quantity:

$$G(a,b) := \delta\left(\frac{A^m(a,b) + A^m(b,a)}{2} - \frac{A^0(a,b) + A^0(b,a)}{2}\right). \tag{124}$$

Setting $b = a + \delta$ and expanding G in a series in δ, we see that $G(a,b) = \lambda + O(\delta^3)$. So we now have an approximation for the eigenvalue that involves nothing more than the integral, $A^m(r,s)$. We remark that $G(a,b)$ is just the approximation for the eigenvalue that we would get if we discretize the integral with $dx = 1$ and use the trapezoidal rule. We emphasize that $G(a,b)$ is not a general formula for the eigenvalue for all b, but rather valid only when $b - a$ is close to zero. Since we are interested in stability, we want to use these expressions to find how the stability depends on, say, a and b. This will be done in the when we numerically analyze Equation (91) and the stability of solutions in Section 4.3.

4.2.7 Large "hole" or "fat" annulus approximation

Our next approximation is to allow the inner radius, a be large. This will allow us to reduce the integral equation, Equation (94) (for $N = 1$) to a simple nonlinear boundary value equation that is related the Burger's equation.

Suppose that $1 \ll a < b$, $H(u)$ is twice differentiable, and the following regularity assumptions on W:

$$c_{22} := \int_{-\infty}^{\infty}\int_{-\infty}^{\infty} W'(Z)\xi^2\eta^2 \; d\xi \; d\eta < \infty,$$
$$c_{20} := \int_{-\infty}^{\infty}\int_{-\infty}^{\infty} W(Z)\xi^2 d\xi \; d\eta < \infty,$$
$$\int_{-\infty}^{\infty}\int_{-\infty}^{\infty} W'(Z)|\xi||\eta|^3 d\xi \; d\eta < \infty,$$

where $Z = \xi^2 + \eta^2$. Let $b = r_1 a$ and $x = a/r$. Then, we find that:

$$\begin{aligned}
\Omega &= \frac{\Omega_2}{a^2} + O(1/a^3) \quad \text{where,} \\
\Omega_2 &= H'(0)\left[\frac{c_{20}}{2} f''(x) + \frac{c_{20}+c_{22}}{x} f'(x)\right] + H''(0)\left[\frac{c_{20}}{2x^2} + \frac{c_{20}}{2} f'(x)^2\right], \\
0 &= f'(1) = f'(r_1), \\
0 &= f(1).
\end{aligned} \tag{125}$$

That is, the equations for $\Omega, f(r)$ becomes a non-linear two-point boundary value problem on $a < r < r_1 a$.

We now turn to the verification of this result. Let $r = ax,\ s = ay,\ b = ar_1$ and $N = 1$ (single armed wave). Then, Equation (94) becomes:

$$\Omega = a^2 \int_1^{r_1} y\, dy \int_{-\pi}^{\pi} W(a^2(y-x)^2 + 4a^2 xy \sin^2(\phi/2)) H(\phi + f(y) - f(x))\, d\phi. \tag{126}$$

Note that we have used $1 - \cos\phi = 2\sin^2(\phi/2)$. Since $W(Z)$ decays for Z large, we see that the main contribution to the integral occurs when $y - x$ and ϕ are close to zero. Thus, we introduce the change in coordinates, $y = x + \xi/a$ and $\eta = 2ax\sin(\phi/2)$, which leads to the following equation:

$$\begin{aligned}
\Omega = \ & a \int_{a(1-x)}^{a(r_1-x)} (x + \xi/a)\, d\xi \int_{-2ax}^{2ax} W(\xi^2 + \eta^2 + \eta^2\xi/(ax)) \cdot \\
& H(2\arcsin(\eta/(2ax)) + f(x+\xi/a) - f(x)) \frac{\partial \phi}{\partial \eta}\, d\eta.
\end{aligned} \tag{127}$$

For a large, we use the usual approach in asymptotic series (see [41]) and note that the endpoints of the integrals can be replaced by $\pm\infty$ for $x \in (1, r_1)$. However, at $x = 1$ or $x = r_1$, the lower or upper endpoints of the outer integral will be 0 which is independent of a, so we have to be careful; these will provide boundary conditions. Our goal is to find equations for Ω and $f(x)$. Since a is large, we write:

$$
\begin{aligned}
f(x+\xi/a)-f(x) &= f'(x)\frac{\xi}{a}+f''(x)\frac{\xi^2}{2a^2}+O(\frac{1}{a^3}),\\
2\arcsin(\eta/(2ax)) &= \frac{\eta}{ax}+O(\frac{1}{a^3}),\\
W(Z+\eta^2\xi/(ax)) &= W(Z)+W'(Z)\frac{\eta^2\xi}{ax}+W''(Z)\frac{\eta^4\xi^2}{2a^2x^2}+O(\frac{1}{a^3}),\\
\text{where}\quad Z &= \xi^2+\eta^2,\\
H(\zeta) &= H'(0)\zeta+\frac{H''(0)}{2}\zeta^2+O(\zeta^3),\\
\text{where}\quad \zeta &= 2\arcsin(\eta/(2ax))+f(x+\xi/a)-f(x),\\
\frac{\partial\phi}{\partial\eta} &= \frac{1}{ax}+O(\frac{1}{a^3}),\\
\Omega &= \frac{\Omega_1}{a}+\frac{\Omega_2}{a^2}+O(\frac{1}{a^3}).
\end{aligned}
$$

We substitute these expansions into Equation (127) and equate powers of a. For notational simplicity, we write $\langle g(\xi,\eta)\rangle$ to mean the integral of g over R^2. To clarify dependencies on ξ,η, we explicitly write $Z(\xi,\eta)$ below. To order $1/a$, for $1<x<r_1$, we obtain:

$$\Omega_1 = H'(0)f'(x)\left\langle W(Z(\xi,\eta))\xi\right\rangle+\frac{H'(0)}{x}\left\langle W(Z(\xi,\eta))\eta\right\rangle.$$

Since W is an even function in ξ,η, both integrals vanish and therefore, $\Omega_1=0$. For $x=1$ or $x=r_1$, the integral with respect to ξ is only on the half line and will not vanish. Recall that we have assumed that $H'(0)>0$ in order to guarantee the stability of synchrony. So to maintain the equality at $x=1,r_1$, we must have:

$$f'(1)=f'(r_1)=0. \tag{128}$$

This provides the boundary conditions for $f(x)$. We next consider the $1/a^2$ terms:

$$
\begin{aligned}
\Omega_2 = {} & \frac{H'(0)f''(x)}{2}\left\langle W(Z(\xi,\eta))\xi^2\right\rangle\\
& +\frac{H''(0)}{2}\left(\frac{1}{x^2}\left\langle W(Z(\xi,\eta))\eta^2\right\rangle+f'(x)^2\left\langle W(Z(\xi,\eta))\xi^2\right\rangle+2\frac{f'(x)}{x}\left\langle W(Z(\xi,\eta))\xi\eta\right\rangle\right)\\
& +H'(0)\left(\frac{1}{x^2}\left[\left\langle W'(Z)\eta^3\xi\right\rangle+\left\langle W(Z(\xi,\eta))\eta\xi\right\rangle\right]+\frac{f'(x)}{x}\left[\left\langle W'(Z)\eta^2\xi^2\right\rangle+\left\langle W(Z(\xi,\eta))\xi^2\right\rangle\right]\right).
\end{aligned}
$$

Integrals with odd terms in η, ξ will vanish because of symmetry. Evaluating the remaining integrals and recalling the phase-normalization, $f(a) = 0$ leaves us with the boundary value problem:

$$
\begin{aligned}
\Omega_2 &= H'(0)\left[\frac{c_{20}}{2} f''(x) + \frac{c_{20}+c_{22}}{x} f'(x)\right] + H''(0)\left[\frac{c_{20}}{2x^2} + \frac{c_{20}}{2} f'(x)^2\right], \\
0 &= f'(1) = f'(r_1), \\
0 &= f(1), \\
c_{20} &= \left\langle W(Z(\xi,\eta))\eta^2 \right\rangle = \left\langle W(Z(\xi,\eta))\xi^2 \right\rangle, \quad c_{22} = \left\langle W'(Z(\xi,\eta))\xi^2\eta^2 \right\rangle.
\end{aligned}
\tag{129}
$$

This is the result in Equation (125). We have thus shown that for large a, solutions to Equation (126) are approximated by solutions to the nonlinear second order boundary value problem Equation (129) for a large. There are three boundary conditions for the second order equation, but Ω_2 is a free parameter, so the problem is not over-determined. One recognizes Equation (129) as being Burgers' equation in polar coordinates. As long as $H'(0) > 0$, there is a unique solution to Equation (129) with the given boundary conditions. If $H''(0) = 0$, then $f(x) = 0$ and $\Omega_2 = 0$ solves the linear BVP. When $H''(0) \neq 0$, the term c_{20}/x^2 provides a "driving force" that pushes $f(x)$ away from 0. If $H(u)$ is odd, then $H''(0) = 0$; indeed, as we have seen throughout this chapter, the even terms in the interaction function are what induce the twist in the rotating waves. For $H''(0) \neq 0$, we can find an exact solution expressed in terms of Modified Bessel functions of imaginary order; Ω_2 is determined by finding a zero of the derivative of the solution. As all of these calculations must be done numerically, we will simply directly solve the BVP via numerical shooting [20].

In sum, we have shown that if a, b are large, then Equation (126) can be transformed into a Burgers-type nonlinear eigenvalue problem. In particular, this theory suggests that $\Omega \sim 1/a^2$ and as a gets large, $f(r)$ approaches a fixed function $\hat{f}(r/a)$ that satisfies the non-linear BVP Equation (129).

We remark that, unlike the narrow annulus calculation, we have not computed the stability of the resulting waves. Based on our work on the purely odd case, we believe that any rotating waves with a large inner radius will be stable. We will see that is the case in the numerics section next.

4.3 Numerical Results, Comparison to Theory, and Generalizations

We now solve Equation (94) (for $N = 1$ unless otherwise noted) and compare the numerical solutions and their stability to the approximations in the last section. Before continuing, we briefly describe how we solve the equations and the stability of the solutions. By choosing $W(R) = \exp(-R)$ and $H(u)$ as a sum of sines and cosines, the integrals in Equation (95) can be evaluated exactly in terms of modified Bessel functions [1]. Then, to solve Equation (94), we discretize the interval $[a, b]$ into L bins and use the trapezoidal rule to approximate the integrals leading to a set of $L + 1$ nonlinear equations. We set $F_j = f(a + jD)$ where $j = 1, \ldots, L$ and $D = (b - a)/L$. We solve for the $L + 1$ unknowns, $\Omega, F_1, \ldots, F_L$ using the nonlinear equation solver in MATLAB or the solver in XPPAUT [20]. Typically, we use $L = 50, 100, 200$. Once we have F_j and Ω, we can plug these into the linearized equation Equation (96). When we discretize the resulting integrals, this is just a matrix whose eigenvalues we find using MATLAB. We sort them according to their real parts and thus determine stability.

4.3.1 Numerical results

For this section, we consider the kernel, $W(R) = \exp(-R)$ and $H(u) = \sin(u+d) - \sin(d)$. In this case, Equation (94) becomes (for $N = 1$):

$$\Omega = 2\pi \int_a^b s \exp(-r^2 - s^2) \left[I_1(2rs) \sin(f(s) - f(r) + d) - I_0(2rs) \sin(d)\right] \, ds, \tag{130}$$

where $I_n(z)$ is a modified Bessel function of the first kind. We numerically solve Equation (130) as follows. To approximate the integral, we discretize $f(r)$ into 201 bins, f_j where $j = 1 \ldots 201$. We discretize the kernel and use trigonometric identities to covert the right-hand side into several matrix-vector multiplications. We then solve for f_j by iteration with $f_1 = 0$. We compute Ω once the iteration has converged.

4.3.1.1 Stability for $d = 0$

Theorem 4.2.2 gives lower bounds for stability as a function of a, b and the perturbation mode m. For our choices of W, H in this section we find that integrals in Equation (100) are calculated to be:

$$\begin{aligned} K_0(r,s) &= 2\pi\exp(-r^2-s^2)I_1(2rs), \\ K_m(r,s) &= 2\pi\exp(-r^2-s^2)\frac{I_{m+1}(2rs)+I_{m-1}(2rs)}{2}. \end{aligned}$$

It is known that $I_m(x) < I_n(x)$ for any $x > 0$ and $0 \leq n < m$. Thus, $K_m(2rs) < K_0(2rs)$ for all $m > 1$ and we must only concentrate on $m = 1$. (As noted above, when $m = 0$, there is a zero eigenvalue corresponding to a constant phase shift of the solution.) We empirically (through the numerical stability) find that if the wave is stable on the annulus with the inner and outer radii of a, b_1 respectively, then it is stable for any $b > b_1$ as well. Thus, given b, we try to find the smallest a, $a_{crit}(b)$ that guarantees stability. We empirically find that if $a < a_{crit}(b)$, then the wave is unstable. When $d = 0$, the solution is $\Omega = 0$, $f(r) = 0$ and we can use Equation (101) and Equation (102) from Theorem 4.2.2 to compare our lower bounds on a that guarantee stability with the actual stability as numerically obtained. We also use the narrow annulus stability approximations of the eigenvalue from Equation (123) and Equation (124). Since $f(r) = 0$, $A^m(r,s) = sK_m(r,s)$. To find the critical value of a using Equation (123), for each value of δ, we find the value of a such that $\lambda_{TA} = 0$ using a numerical root finder. An extremely simple expression for the critical approximation can be found by using Equation (124). For $m = 1$,

$$G(a,b) = \frac{1}{2}\delta\pi(a+b)e^{-a^2-b^2}\left[I_2(2ab)+I_0(2ab)-2I_1(2ab)\right].$$

Let a_{GG} be the root of $I_2(x) + I_0(x) - 2I_1(x)$. Then, we see that $G(a,b) = 0$ when $a = a_{GG}/(2b)$. Figure 15 shows the results of the stability analysis. The curve labeled NU shows the numerically determined stability boundaries as determined using a discretized Jacobian matrix for $m = 1$ mode perturbations. We see that as b gets larger, the minimal inner radius decreases (roughly like $1/b^2$). This leads us to conjecture that *rotating waves are stable on the infinite disk.* In particular, we do not think that the waves will be stable on any finite disk; a small hole is needed. The dashed line labeled GG provides the sufficient condition for stability from Theorem 4.2.2, $a > a_{GG} \approx 0.8789$. It meets NU at a_{GG}, where $b = a$. The curve labeled IGG is the sufficient condition for stability from Equation (102). There is some improvement over the line GG. The line labeled TA comes from Equation (123). It is tangent to NU at a_{GG} but loses accuracy for larger b. Interestingly, the very simple curve, $a = a_{GG}/(2b)$, labeled TA2, obtained from the zeros of $G(a, b)$ appears to be much more accurate, even for larger b and, like NU, asymptotes to 0 as b increases. As with TA, it too is tangent to NU at a_{GG}.

4.3.1.2 Effects of higher harmonics for odd coupling

We turn now to the analysis of the effects of higher harmonics on odd coupling functions H. Unlike $H(u) = \sin(u)$, if there are higher harmonics, it may be necessary to compute the stability to modes $m > 1$ as a function of the inner and outer radii of the annulus. Figure 16 shows the results of stability analysis for $H(u) = \sin(u) + \rho \sin(2u)$. In order to assure that $H'(0) > 0$, $\rho > -0.5$. For the range, $-0.5 \leq \rho \leq 0.5$, according to Theorem 4.2.2, we find that stability to $m = 1$ perturbations implies stability to $m > 1$. (This is not true for all ρ; for ρ sufficiently large, $m = 2$ perturbations determine stability.) In the top panel, we see for $\rho = -0.25$ ($\rho = 0.25$) that for a given value of inner radius, a, the minimal outer radius for stability is smaller (resp. larger) than for $\rho = 0$. In the lower left we show $H'(u)$ for the three values of ρ. For $\rho < 0$ ($\rho > 0$), the region of u where $H'(u) > 0$ is larger (resp. smaller) than for $\rho = 0$, so that in a sense, greater (resp. lesser) phase-differences are tolerated for spatially nearby oscillators. Thus, the large phase-gradients that occur near the inner radius are more stable (less stable) for $\rho < 0$ ($\rho > 0$). We were not able to compute the stability curves for large b when $\rho \neq 0$, but we suspect that as $b \to \infty$, the minimal radius for stability goes to 0. Setting $G(a, b) = 0$ in Equation (124) defines the thin curves tangent to the numerically computed curves, (The $\rho = 0$ curve is omitted as it is in Figure 15.) In the bottom right panel, we plot a_{GG} as a function of ρ for $m = 1$ (upper curve) and $m = 2$, lower curve. Since a_{GG} for $m = 1$ is larger than that of $m = 2$, the $m = 1$ curve determines the sufficient condition. The filled circles correspond to the 3 curves shown in the top panel.

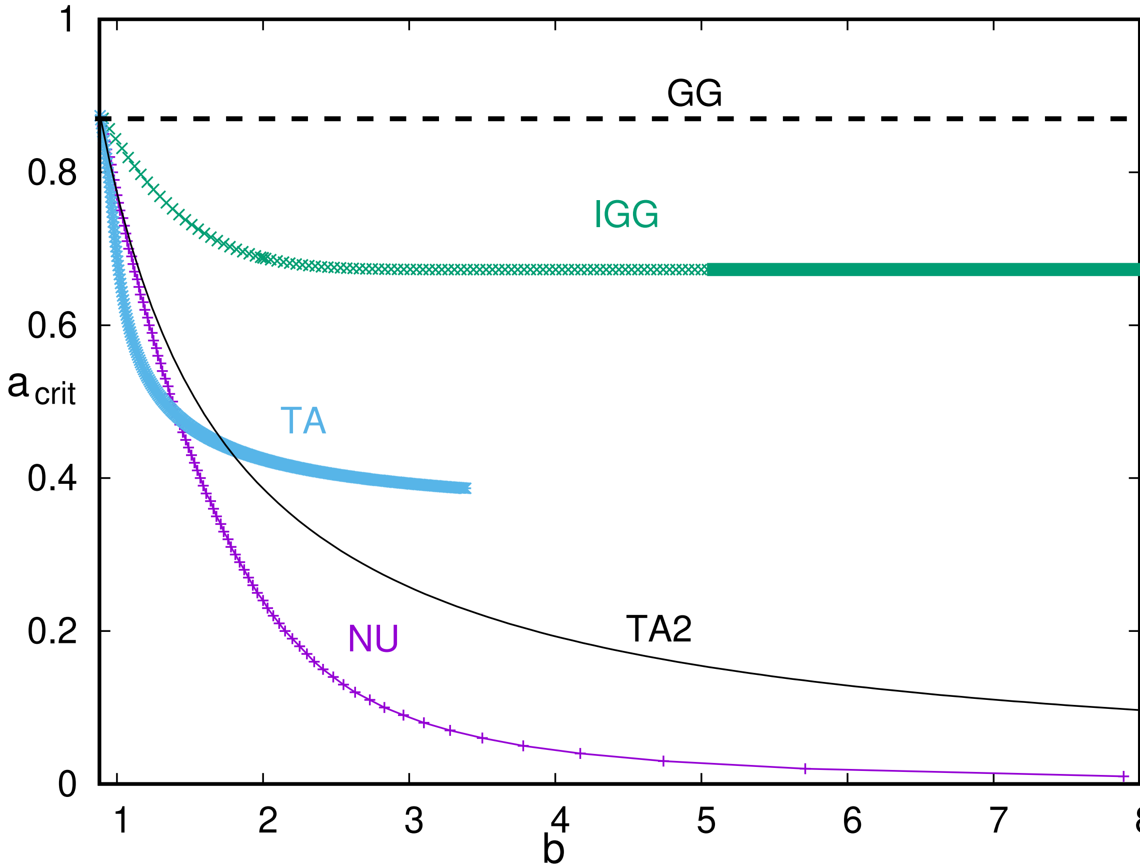

Figure 15: Stability boundaries for the radial rotating wave, $u = \theta$ for $H(u) = \sin(u)$ and $W(R) = \exp(-R)$. Regions above the curves will be stable. NU: Numerically determined from the discretized equations; GG: Bound for Equation (101); IGG: Bound from Equation (102); TA: Thin annulus approximation using Equation (123); TA2: The simple thin annulus approximation from setting Equation (124) to zero, $a = a_{GG}/(2b)$.

As ρ gets more negative, rotating waves with smaller radii are stably supported.

4.3.1.3 Multi-armed waves for odd coupling

For odd interaction functions, there exist multi-armed rotating waves to Equation (91) of the form $u(r, \theta, t) = \omega t + N\theta$ and their stability is determined, again, by linearization. As before we require that the eigenvalues for Equation (98) have negative real parts. For the simple case of $H(u) = \sin(u)$ and the Gaussian kernel,

$$\begin{aligned} A_N^m(r,s) &= 2\pi s e^{-r^2-s^2} \frac{I_{m+N}(2rs)+I_{m-N}(2rs)}{2}, \\ A_N^0(r,s) &= 2\pi s e^{-r^2-s^2} I_N(2rs). \end{aligned}$$

The estimate in Theorem 4.2.2 for the minimal requirements for stability can be applied for multi-armed spirals. For example, take $N = 2$, then we find that the minimal radius to be the root of $I_0(2a^2) + I_4(2a^2) - 2I_2(2a^2) = 0$, which is $a = 1.39753\ldots$. (Note that this root occurs from $m = 2$ mode perturbations). This minimal radius is close to twice the minimum found for the one-armed spiral. We have also numerically studied the stability of double armed waves (not shown); the minimal inner radius is always larger for larger N. Multi-arm rotating waves require large inner radii for stability; roughly scaling with N.

4.3.1.4 Non-odd coupling

We turn our attention to Equation (94) for the single-armed wave ($N = 1$), $W(R) = \exp(-R)$ and $H(u) = \sin(u + d) - \sin(d)$. Recall that the rotating wave has a solution, $u(r, \theta, t) = \Omega t + \theta + f(r)$ on $a \le r \le b$ with $f(a) = 0$. We must numerically solve Equation (130), which we do by discretizing the interval (a, b) into 100 bins. Figure 17 shows some example solutions as the radii of the annulus vary as well as the parameter, d which determines the magnitude of the even component of $H(u)$. In the top panels, we show $f(r)$ for each of three annuli, with $[a, b] = [1, 10], [2, 10], [2, 20]$. Below these panels, we depict the phase of the rotating wave on the corresponding annulus. Clearly, as d increases, the functions $f(r)$ increase in magnitude, and corresponding to this, the resulting twist in the waves increases. (We use the term "twist" to denote the deviation from a radial wave; that

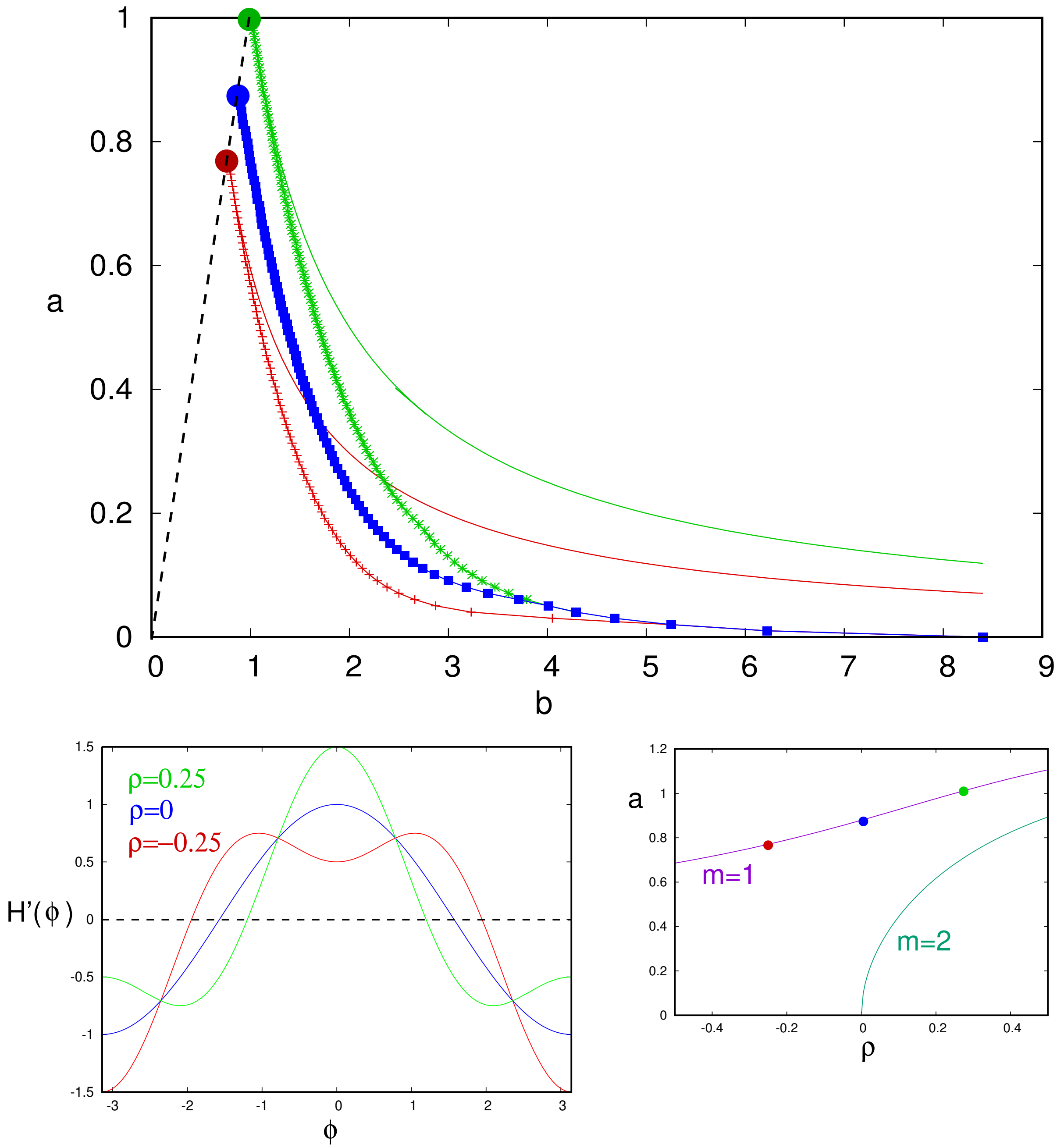

Figure 16: Effects of harmonics on the stability of the radial rotating wave. (Top) Numerically found stability boundaries for $H(u) = \sin(u) + \rho \sin(2u)$ for $\rho = -0.25, 0, 0.25$. Dashed line is $b = a$. Large filled circles are the a_{GG} from Theorem 4.2.2. Thin lines are from the narrow annulus approximation. Lower left shows corresponding $H'(u)$. Bottom right shows minimal value of a (a_{GG}) for stability from Theorem 4.2.2 at modes 1 (purple) and 2 (cyan). Filled circles are the values of ρ shown in the top panel.

is the magnitude of $f(r)$.) For a given d, the dimensions of the annulus clearly also have an effect: given b, the smaller the value of a the larger $f(b)$ will be. For a fixed a, as b increases, the relative magnitude of $f(r)$ also increases. Specifically, in panel B, the domain is $[2,10]$ and in panel C, $[2,20]$. In panel B, clearly the value of $f(10)$ is less than that value of $f(10)$ in panel C (indicated by the dashed line). Thus, the geometry of the annulus has a strong effect on the "twist" of the spiral (the magnitude of $f(r)$). The annuli with dimensions $[1,10]$ and $[2,20]$ are geometrically similar. However, $f(10)$ is almost twice as large as $f(20)$; the inner radius has a very strong effect on the twist of the rotating wave.

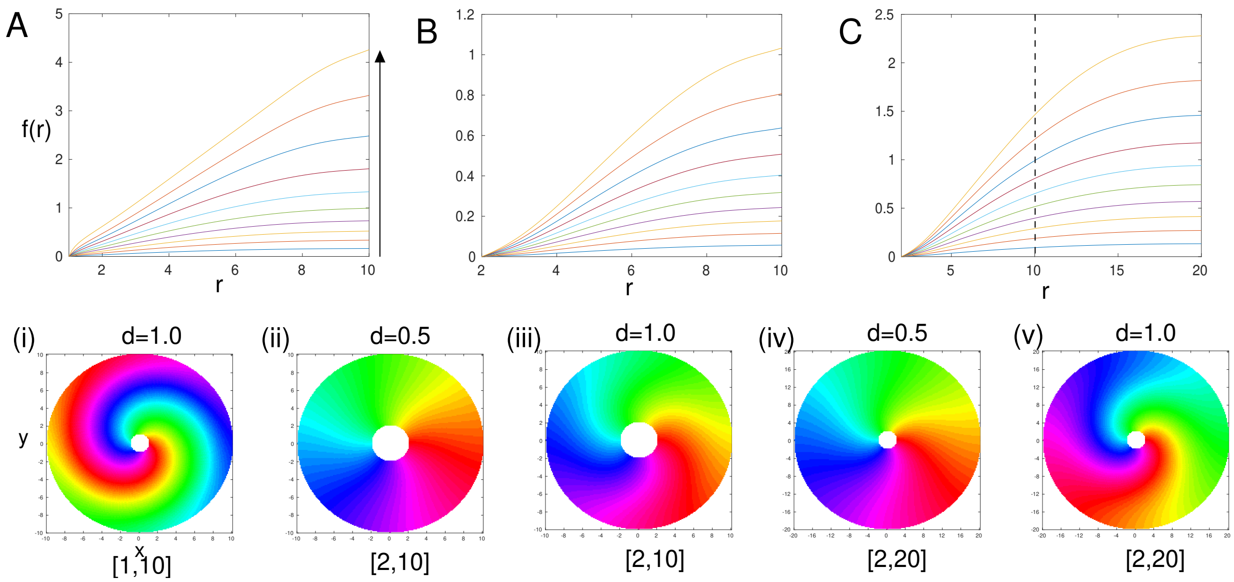

Figure 17: Solutions to Equation (90) for $W(R) = \exp(-R), H(u) = \sin(u+d) - \sin(d)$ on annuli of different radii. Top panels show $f(r)$ on $[a,b]$ as d increases from 0 to 1 (bottom to top). Bottom panels show the rotating wave on the annulus. Values of d, a, b are given on the images.

We explore these effects in more detail in Figure 18 where d, a are varied. In the left panel, we vary d holding a, b fixed at the values in Figure 17. The frequency Ω grows in magnitude with d, but for $a = 2$, these effects are weak. When $a = 1$, as d increases there is a sharp drop in Ω once d exceeds 0.5. Figure 17 showed a similar effect on the shapes of $f(r)$ as d varied. For fixed $b = 5$, $d = 0.5$, we look at $f(b)$, $-\Omega$ as a decreases from 4 to 0.5 on a log-log plot in the right panel of Figure 18. It appears that $f(b) \sim 1/a^2$ and $-\Omega \sim 1/a$

as $a \to 0$. Both the frequency and the twist are very sensitive to a as it decreases. There is some sensitivity to b (not shown) but less so. We remark that for fixed b, d, there is a minimal a below which solutions do not appear to exist as we will see next.

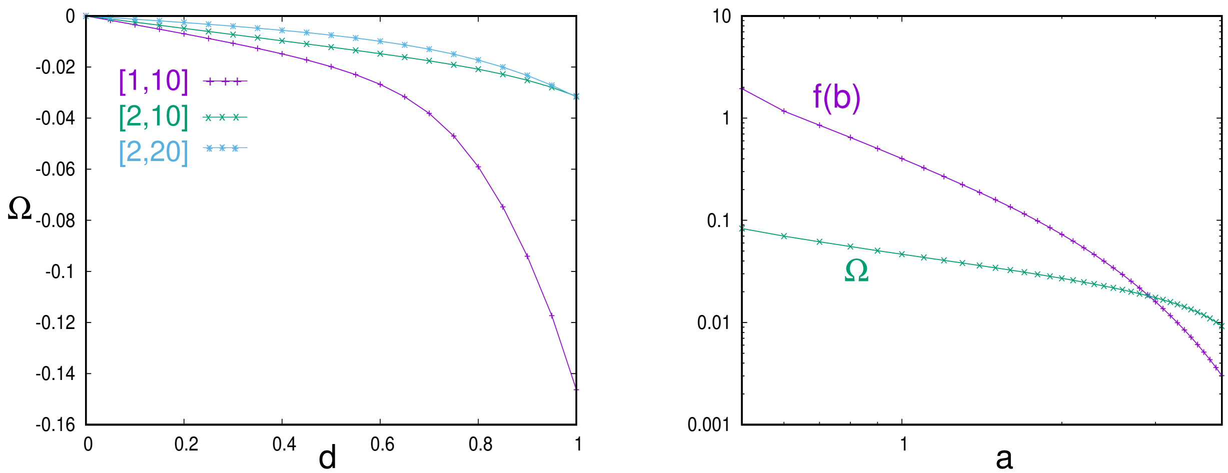

Figure 18: Effects of d, a on the rotating wave. (Left) Ω as a function of $d \in [0, 1]$ for the three examples in Figure 17; (Right) Ω and $f(5)$ as a function of a for $d = 0.5$ on the annulus $[a, 5]$ on a log-log plot.

Figure 15 provides boundaries for the stability of the rotating wave when $d = 0$ as a function of a, b. In the case where $d = 0$, that is, $H(u)$ is odd, we are guaranteed the existence of the waves since we have an explicit form for them. However, existence is not guaranteed for general coupling. Thus, we now explore the range of existence for various values of a, d when b is fixed. To get the range of existence, we fix a and then vary d until we can no longer find a solution to Equation (94); we call this value d^*. Figure 19 shows the results of this calculation for three values of b. (We were unable to use continuation to get smoother curves, so these values were computed manually.) For small a, solutions exist only for proportionally small values of d. (Indeed, the line $d^* = a$ is a very close fit and we know that $d^*(0) = 0$.) As a increases, it appears that d^* saturates at close to $\pi/2$. We note that the curves are all quite close. For a given d, the minimal value of a guarantees a solution is slightly smaller for smaller values of b. For a, b large enough, it appears that d can be any value in $(-\pi/2, \pi/2)$. (Recall that if $d < 0$, we change the sign of $f(r), \Omega$ and the result is equivalent to the case $d > 0$.) Our results in Section 4.2.7 show that solutions exist as long as $H'(0) > 0$ which, for our choice of $H(u)$, implies $d \in (-\pi/2, \pi/2)$.

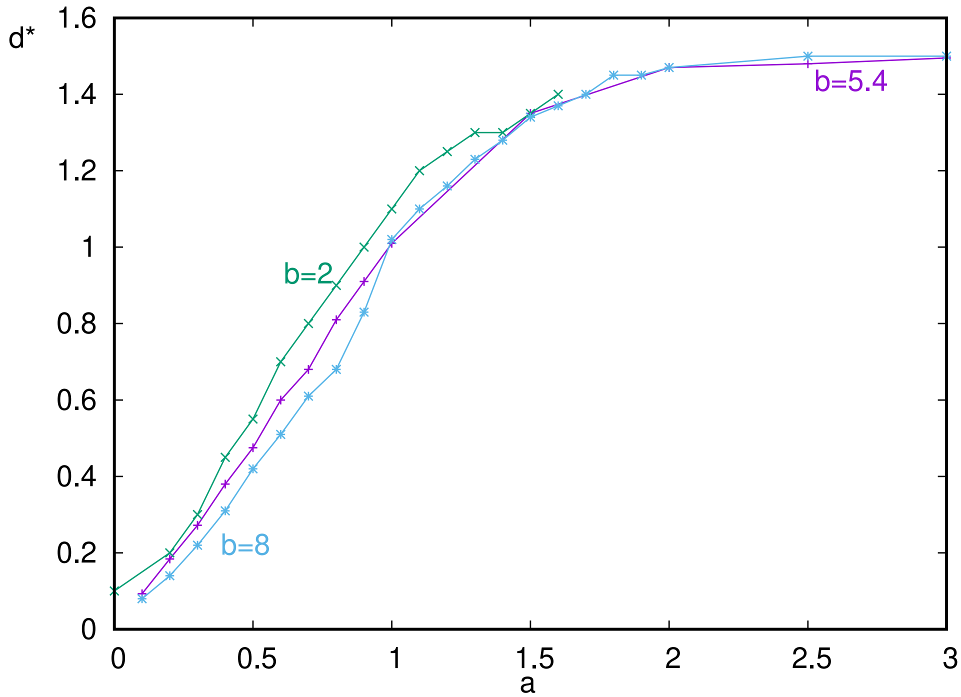

Figure 19: Critical value of d above which there is a solution to Equation (94) for $b = 2.0, 5.4, 8.0$.

4.3.2 Approximations and numerics

In Section 4.2.6 and Section 4.2.7 we developed approximations for quantities such as the frequency and "twist" of the spiral as well as the stability. In this section, we compare the approximations with the numerical examples.

4.3.2.1 Narrow annulus and friends

We now compare the results of the theory developed in Section 4.2.6 with the numerically computed solutions to Equation (94). Because the large radius approximations are general and apply to any outer radius, we will restrict the comparisons here to small a. We have already compared the approximate stability when $d = 0$ in Figure 15, so here, we focus on the formulas for Ω and $f(b)$. For Ω, we use Equation (117) and for $f(b)$, we use the linear approximation, $f(b) = f_1(b-a)$ where f_1 is given by Equation (115). The required integrals for these approximations are easy to evaluate for the Gaussian kernel and for $H(u) = \sin(u+d) - \sin(d)$. Figure 20 shows a comparison of the formulas for the narrow annulus approximations and the numerical simulations. In the first two panels, A,B, we fix $a, \delta = b - a$ and vary d and plot the frequency, Ω and the value of $f(b)$. Recall that larger values of $f(b)$ lead to more "twist" in the rotating waves. The theory captures the numerics even when $\delta = 1$. In the lower panels, C,D, we fix δ and $d = 1$ as we vary a the inner radius. As a gets larger the theory and simulations are much closer in agreement, but even for $a = 1$, the theory is close. It is very close over the whole range of a for $\delta = 0.1$ as expected for a perturbation theory.

4.3.2.2 Large "hole" or "fat" annulus approximation

The large a approximation, Equation (129) reduces the integral equation to the solution of a Burgers-type equation. To make this reduction, we supposed that the function $f(r)$ converged to a function of r/a as a increased. Thus, we first check this assumption. We fix $d = 0.5$ and $r_1 = b/a = 3$ and vary a in Figure 21. It is clear from this figure that the scaled $f(r)$ does not change much once $a \geq 2$. Other choices of d lead to a similar result (not shown). To compare the numerical results to the Burgers approximation, we numerically solve the boundary value problem Equation (129) on $(0, r_1)$. For our choice of $H(u)$ and the Gaussian kernel, we have $H'(0) = \cos(d)$, $H''(0) = -\sin(d)$, $c_{20} = \pi/2$, and $c_{22} = \pi/4$. The solid black line in Figure 21 depicts the solution to the Burgers equation for $r_1 = 3$. Thus, for this choice of parameters ($r_1 = 3, d = 0.5$), the agreement between theory and numerics is quite close.

To explore the theory more completely, we look at the scaled frequency, $\Omega_2 = a^2\Omega$, and $f(r_1 a)$ as d varies between 0 and 1 and $r_1 = 3, 5$ in Figure 22. Recall that $f(b) = f(r_1 a)$ quantifies the amount of "twist" in the spiral. Except for $a = 1$, the results from the Burgers approximation are very close to the numerics and even at $a = 1$, the curves are qualitatively correct. Curiously, when $r_1 = 5$, the approximation is close even when $a = 1$ as can be seen

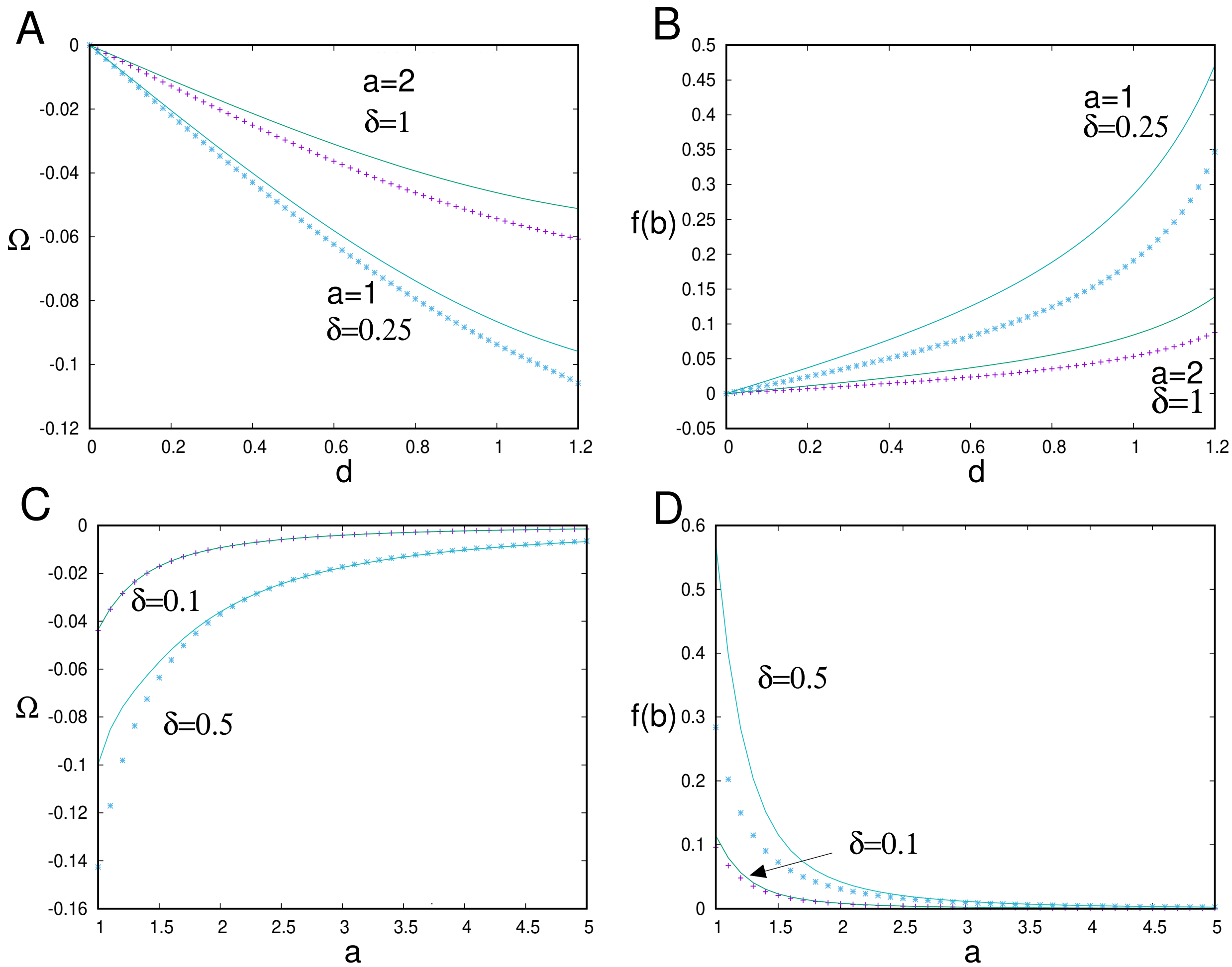

Figure 20: Narrow annulus theory compared to numerical simulations. (Lines are approximations, stars and crosses are numerical simulations.) (A) Ω vs d for two different values of a and $\delta = b - a$; (B) Same as A, but showing $f(b)$; (C) Ω vs a for $d = 1$ and $\delta = 0.1, 0.5$; (D) Same as C, but showing $f(b)$.

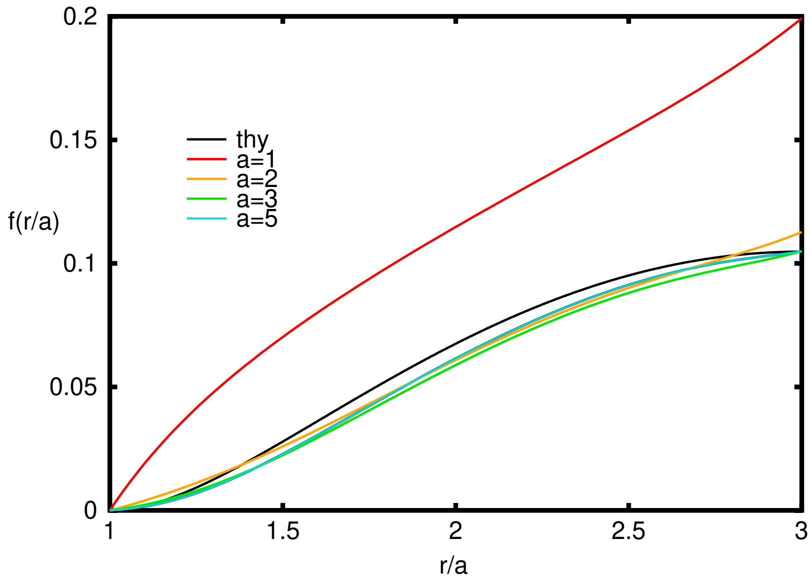

Figure 21: Scaled function $f(r)$ for $d = 0.5$ and $b = 3a$ as a increases. Black line is the Burger's approximation.

in panels C and D (especially the frequency, Ω_2.)

In this part of the paper, we have shown that there is good agreement between the full numerical solutions to Equation (94) and several different theoretical approximations. For $a \gtrsim 2$, the large "hole" approximation is quite good for different values of r_1, d. On the other hand, for smaller values of a, the narrow annulus approximation is good as long as $b - a$ is small. Neither of the theories in this part of the paper can explain the scaling of the stability in Figure 15 as $a \to 0$ and $b \to \infty$. This remains an open question.

4.3.3 Beyond rigid rotating waves: the birth of spiral chimeras

Our analysis has focused on the existence and stability of rigid rotating wave solutions to Equation (90) that satisfy, $U(r, \theta, t) = \Omega t + \theta + f(r)$ where $f(r), \Omega$ solve the integral equation Equation (94). As Figure 15 show, such solutions do not always exist, nor are they necessarily stable. Our Burgers approximation and Theorem 4.2.2 suggest that if the

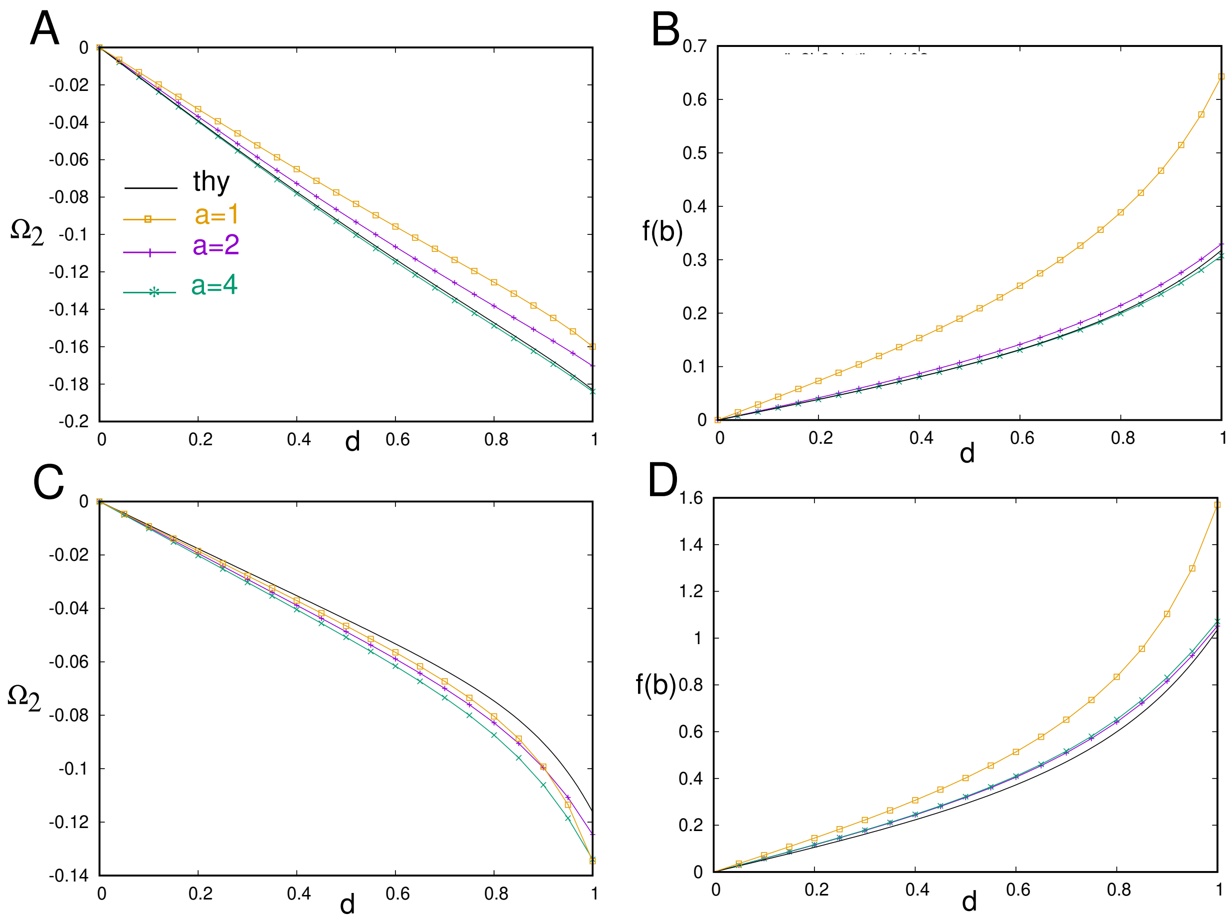

Figure 22: Comparison of Equation (129) to the numerical solutions to Equation (94) on the annulus $a < r < r_1 a$ for different values of d. (A) the scaled frequency, Ω_2 on $(a, 3a)$; (B) $f(3a)$; (C) Ω_2 on $(a, 5a)$; (D) $f(5a)$. Solid black line is the Burgers approximation.

annulus has a sufficiently large inner radius, then the rigid rotating waves exist and they are stable. In this section, we turn our attention to the case where a is small or d is large and explore the fate of these waves. To do this, we simulate the solutions to Equation (90) with Gaussian and other kernels for $H(u) = \sin(u + d) - \sin(d)$. We employ a rectangular grid (restricting to the annular region) that discretizes the region $[-b, b]^2$ into a 101×101 grid. We excise the set of points that have a radius less than a to represent the hole. To speed up the simulations (which are done in MATLAB), we unwrap the square into a vector and create a $(101 \times 101)^2$ matrix that encodes the coupling and the hole. Using trigonometric identities, we can convert the nonlinear integral equation into several matrix vector multiplications. We initialize $U(x, y, 0) = \text{atan2}(y, x) + \epsilon N(0, 1)$ where $\text{atan2}(y, x)$ is the argument of $x + iy$ and $N(0, 1)$ is a normal random variable with mean 0 and variance 1 to make a small perturbation away from the perfect rotating wave. We integrate the discretized system with Euler's method and a step size of 0.05, for 500 or more time steps. (We integrate for longer to check that steady states have been reached and to see the behavior when there are no steady solutions.) For plotting, we subtract $U((a + b)/2, 0, t)$ to set the 0 phase point. (We have also used finer discretizations as well to cross check the results.) We remind the reader that the synchronous solution, $U(r, \theta, t) = \Omega t$ always exists and is always stable so long as $W(R) \geq 0$ and $H'(0) > 0$.

We first consider the case $d = 0$ where the solution to Equation (91) is $U(r, \theta, t) = \theta$. Figure 15 shows that if a is small enough, then, the rotating wave will lose stability; for example if $b = 1.2$, then, $a \gtrsim 0.6$ for stability. Figure 24 (upper left) shows the results of a simulation where $a = 0.2$, well below the stability line. We stopped the simulation after 100 iterations in order to show how the synchronous solution "takes over" the annulus. Over time the red (synchrony) completely encroaches on the other phases leaving only a synchronous solution. In the supplemental files, we show a video of the evolution to synchrony (see Video S1: instab.mp4). Repeated simulations with different initial data eventually all seem to go to synchrony. We found that the loss of stability is through a zero eigenvalue and because of the odd symmetry, this implies that generically there will be a pitchfork bifurcation. Because we see no solutions other than synchrony when integrating the equations forward in time, we suspect that if there is indeed a pitchfork, it is subcritical.

The case where $d \neq 0$ is more interesting. In the remaining panels at Figure 24, we take $b = 5.4$ and vary a, d. Recall that Figure 19 was constructed by seeking fixed points to Equation (94) and increasing d until none could be found. These numerical results suggest that the loss of the rotating wave occurs through a saddle-node bifurcation as this is the generic means by which equilibria are lost. We remark that [46] found that rigid rotating waves lost stability through a *Hopf bifurcation* whereas we are suggesting it occurs via a saddle-node bifurcation. We believe that this difference is a consequence of our using a scalar phase model, while [46] uses a two-dimensional model for phase and amplitude. Figure 23 and Figure 24 (upper left) show the simulation of transition from a rotating wave to a synchrony. Figure 24 (upper right) shows a simulation with $d = 0.65$, $a = 0.5$, below the existence curve in Figure 19. See also Video S2: chimera.mp4.) We see that for $r \gtrsim 1$, there is a regular phase-locked spiral. However, near the hole in the annulus, the behavior is much more random. This phenomena was first described in [66] for nonlocally coupled Fitzhugh-Nagumo equations (with $a = 0$) and subsequently called a *spiral wave chimera* [51]. (The term *chimera* was used because the solution is a mixture of the regular rotating wave and the randomized asynchronous behavior near the center of the spiral.) Figure 25 shows the phase as a function of time for oscillators from the incoherent core and the coherent rotating wave region. Oscillator 1 and 2 are incoherent while oscillator 3 and 4 are phase-locked. Figure 26 shows the relative phase of one point along the $x-$axis near $x = 0.5$ over time. The dynamics of this point shows so-called phase-drift, a phenomenon that is typical in coupled oscillators when locking is lost via a saddle-node bifurcation. When d is increased to 0.75, the instability becomes more complicated: a chimera forms at the core and breaks off before returning to the core and repeating the cycle. (See Video S3: wanderchimera.mp4.) When the outer radius $b = 2$, a similar chimera is formed which drifts to the outer radius and becomes the synchronous solution. (See Video S4: transchimera.mp4.) Figure 19 shows that for $a = 0.5$, we need d to be less than 0.38 for a solution to exist; in Figure 24 (lower left) we thus reduce d to 0.35 and see that the rotating wave persists. However, if we shrink the inner radius to, say, $a = 0.2$, then, once again, the instability occurs and we get drift (simulation not shown). Holding $d = 0.65$ but setting $a = 0.8$ puts us in the stable region as shown in the lower right panel of Figure 24. Thus, we conjecture that spiral chimeras are formed when the rigid rotating wave on the annulus disappears through a saddle-node bifurcation as either d increases (the even terms in the interaction function) or a decreases past the critical existence curve in Figure 19. One can think of cutting a hole in the disk as a way of cutting out the asynchronous core and preventing the chimera. Comparing the two right panels, it is clear from the top panel that the asynchronous behavior extends to at least $r \approx 1$. However, in the lower panel, we only needed to give the hole a radius of 0.8 to revive the rigid spiral. We conclude with Figure 27 which shows snapshots of the dynamics when the domain is a disk of radius 5 (no hole, $a = 0$) and d takes on three values. (See Video S5 in the supplement.) For $d = 0.35$, the disorganized core (chimera) remains centered and has a small diameter. For $d = 0.60$, the disorganized core is bigger and begins to "wobble" off the center but appears to remain in the domain for all time. Finally for $d = 0.75$, the "wobble" is so large, that the disorganized central region moves off the edge and the solutions all tend to synchrony. Cutting a large enough hole in the disk allows us to avoid the chimera region and leads to a stable rigid rotating wave. One might ask if it is possible to choose an interaction function $H(u)$ such that the rigid wave is stable for $a = 0$. Based on the narrow annulus theory, we believe that as long as $H'(0) > 0$ (that is synchrony is stable), then this is not possible.

4.3.4 Other kernels

So far, we have considered the Gaussian kernel, mainly because the integrals needed to obtain in Equation (94) are easy to evaluate in this case. There are other kernels where the relevant functions $\hat{W}_N(r, s, \chi)$ can be computed. However, if we solve the full equations Equation (90), any kernels can be used.

4.3.4.1 Simple kernels

We fix $b = 8$, $a = 1$, $d = 0.65$ and consider four kernels: $W_{gaus}(|x|) = \exp(-|x|^2)$, $W_{exp}(|x|) = \exp(-|x|)$, $W_{Lor1}(|x|) = 1/(1 + |x|^2)$, $W_{Lor2}(|x|) = 1/(1 + |x|^4)$. The top part of Figure 28 illustrates the behavior over time for the initial condition $U = \theta$ in the annulus. There is a stable rigid spiral for the Gaussian kernel. However, for the exponential kernel

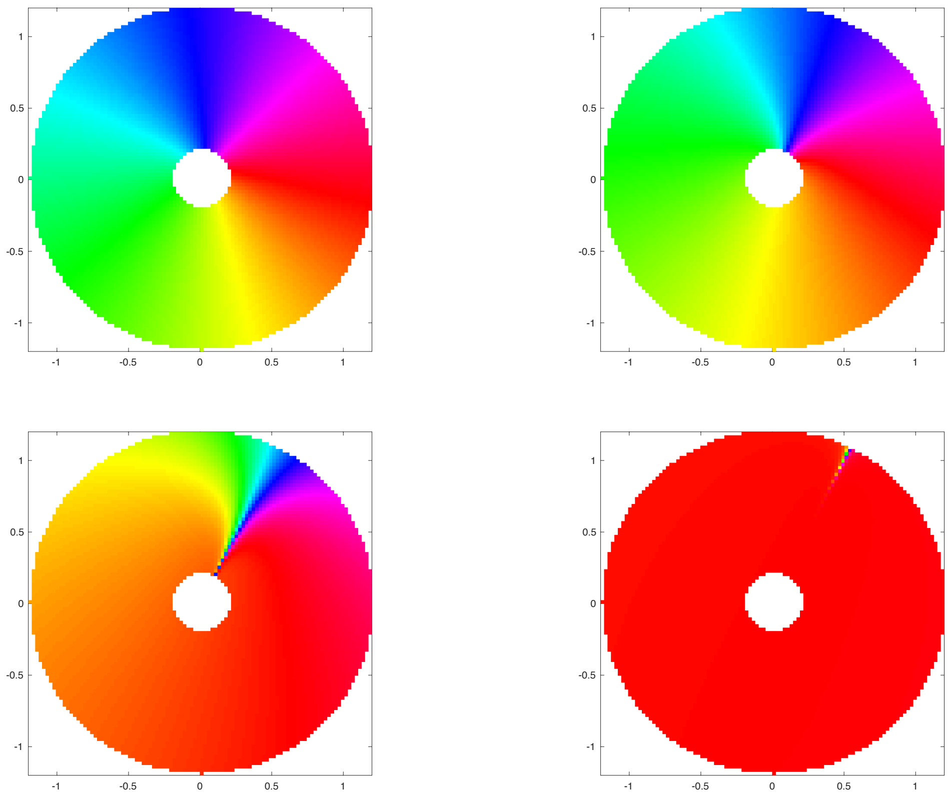

Figure 23: Temporal change from rotating wave to synchrony on annulus $a = 0.2,\ b = 1.2$: $t = 158,\ 162,\ 166, 170$.

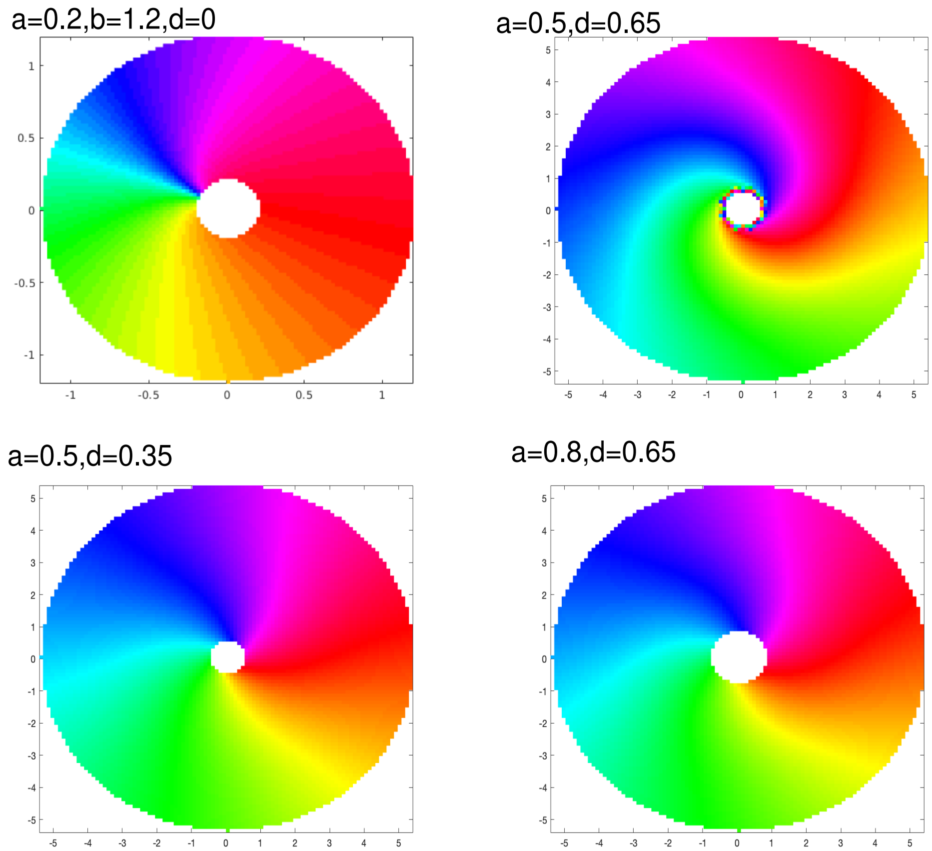

Figure 24: Simulations of Equation (94) on the annulus for various values of a, b, d and a Gaussian kernel. Domain $[-b, b]^2$ is discretized into a 101×101 grid. See text for explanations.

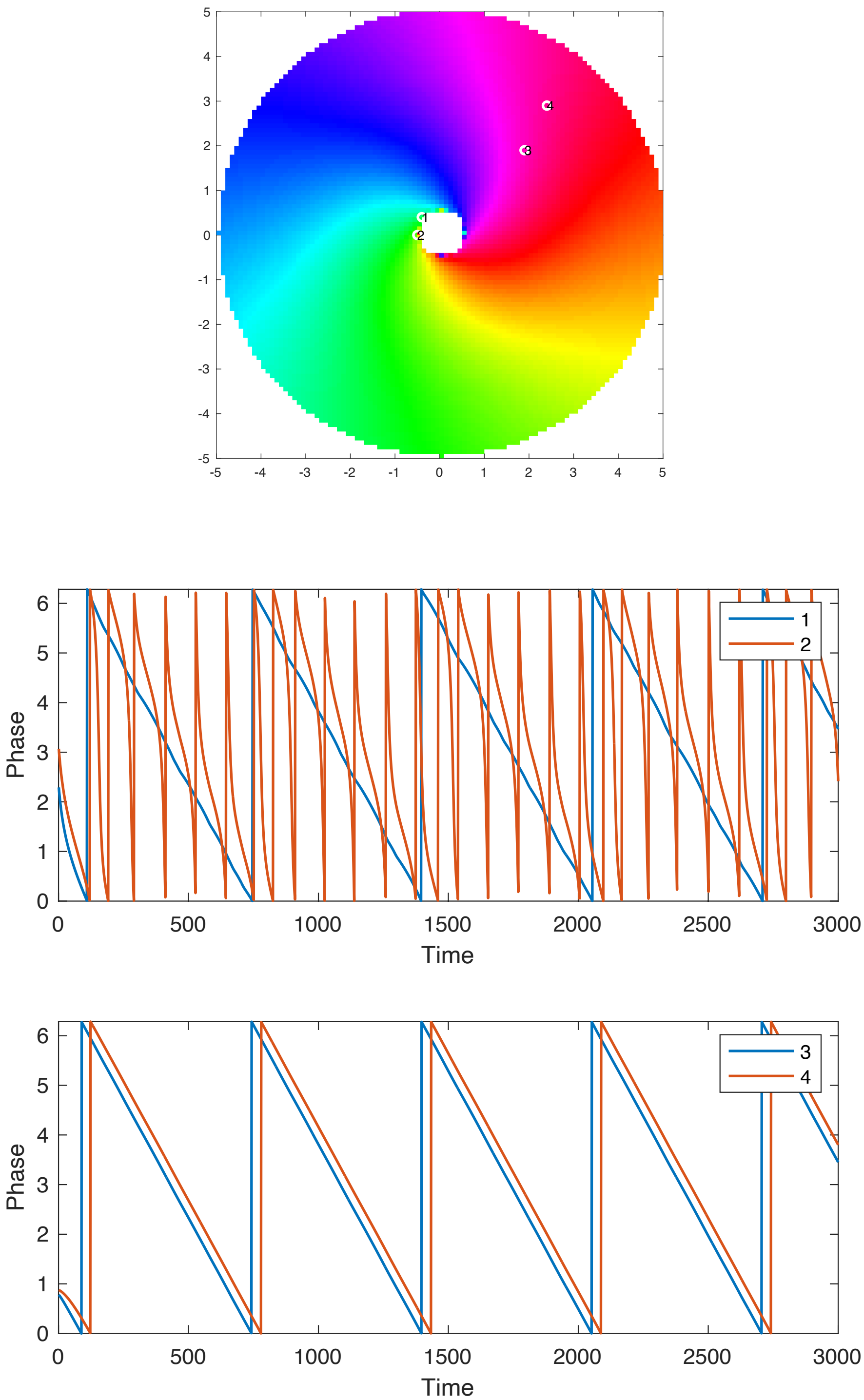

Figure 25: Incoherent and coherent oscillators in chimera. Oscillator 1 and 2 are taken from the incoherent core, 3 and 4 are taken from the coherent region (stable rotating wave). Lower panel shows phase as a function of time for each oscillator. Parameters for simulation are: $a = 0.5$, $b = 5$, $d = 0.55$.

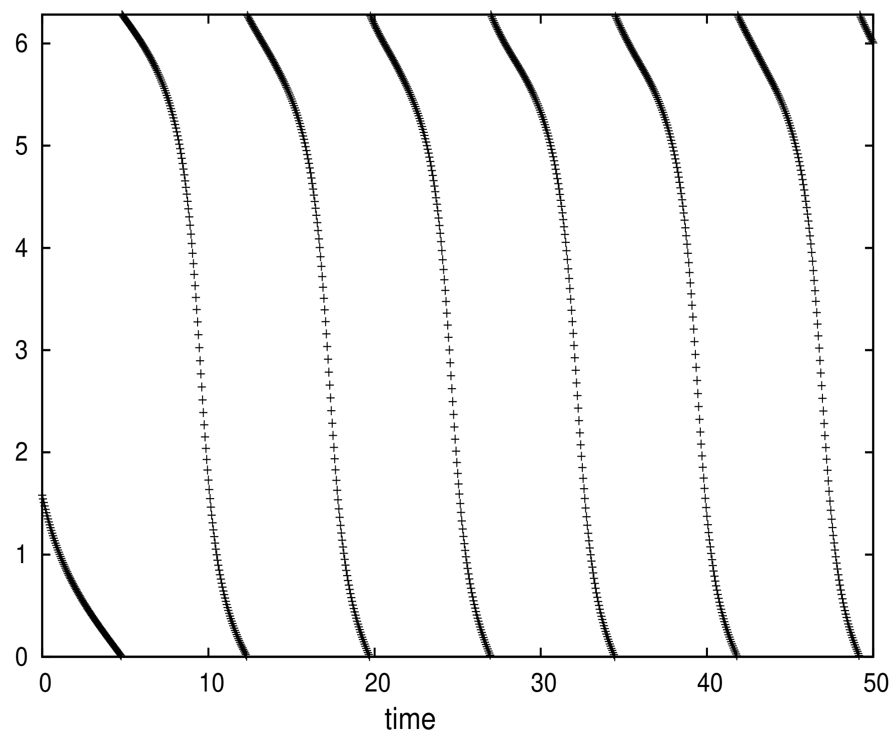

Figure 26: Relative phase of one point on the $x-$axis near $x = a$ for $a = 0.5,\ d = 0.75,\ b = 5.4$.

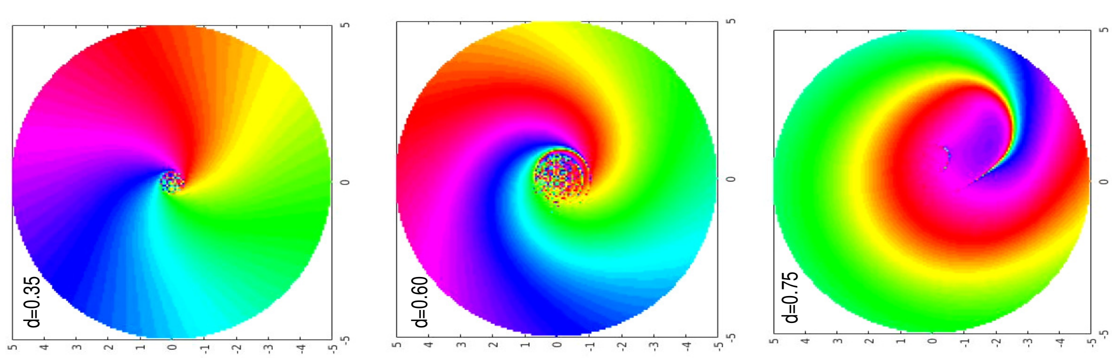

Figure 27: Dynamics on the disk for $d = 0.35,\ 0.60,\ 0.75$. In the case of $d = 0.75$, the wave hits the edge and the system becomes synchronized. Videos of these are available in the supplement (see Video S5).

with the same parameters, we observe the asynchrony near the hole associated with the saddle-node and phase-drift ("chimera" solution). The kernel that decays like $1/r^4$ also appears to maintain a stable rigid spiral while the kernel decaying more like $1/r^2$ shows a similar instability to the exponential kernel. In fact, if the simulation is run longer, the solution converges to synchrony for any d. We can get an intuitive idea of why rigid spirals do not exist for the kernels on the right panels. From Theorem 4.2.4, the existence of rigid rotating waves is guaranteed as long as

$$\int_{-\pi}^{\pi} W(r^2 + s^2 - 2rs\cos\phi)H'(\phi + f(s) - f(r))\ d\phi > 0$$

for all r, s. Since $H'(0) > 0$, this inequality will hold as long as the kernel decays quickly enough away from $\phi = 0$. The bottom panel of Figure 28 shows the four kernels at $r = s = a$ as functions of ϕ. Both W_{exp}, W_{Lor1} are quite large for $\phi \in (\pi/2, \pi)$. We suspect that the fact that these two kernels do not decay fast enough is why there is not a stable rigid rotating wave. Intuitively these kernels weight phase differences near $\phi = \pi$ too strongly and thus can cause instability or non-existence of the rigid spiral wave.

Theorem 4.2.2 provides a sufficient condition for stability of the rotating wave $U = \theta$ which exists for odd interaction functions, namely:

$$\left|\int_{-\pi}^{\pi} W(r^2 + s^2 - 2rs\cos\theta)H'(\phi)\cos(m\phi)\ d\phi\right| \le \int_{-\pi}^{\pi} W(r^2 + s^2 - 2rs\cos\theta)H'(\phi)\ d\phi$$

for all integers m, and $a \le r, s \le b$. These integrals can be computed for $H(u) = \sin(u)$ and $W(|x|) = 1/(1 + |x|^2)$. Setting $r = s = a$ and $m = 1$, we find that the inequality is *not* satisfied for any a. While this does not prove instability (except in the narrow annulus case), it also prevents us from concluding stability on *any* annular domain.

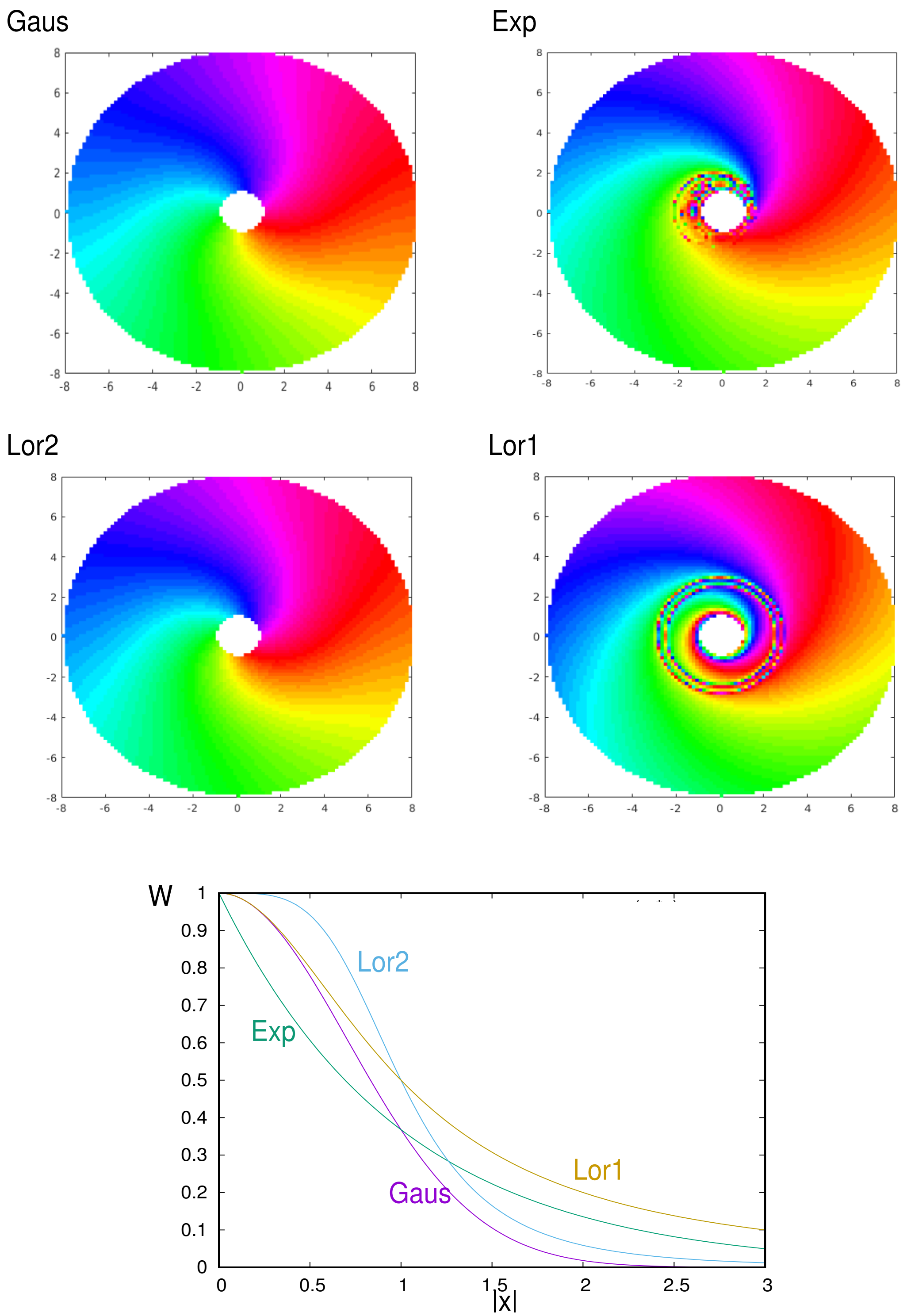

Figure 28: Top: Behavior of the full model on the annulus $1 < r < 8$ with $d = 0.65$, for four different kernels; Bottom: the four kernels.

4.3.4.2 Green's function kernel

Finally, we briefly discuss the Green's function kernel (inverse operator), $W_G(\mathbf{x})$ for the operator $LV = V - \nabla^2$ on the annulus with no-flux boundary conditions and $H(u) = \sin(u+d) - \sin(d)$. We can write the phase-locked solution to Equation (90) as

$$\begin{aligned}\Omega = \sin(-u(\mathbf{x})+d)\int_A W_G(\mathbf{x}-\mathbf{x}')\cos(u(\mathbf{x}'))\ d\mathbf{x}' \\ + \cos(-u(\mathbf{x})+d)\int_A W_G(\mathbf{x}-\mathbf{x}')\sin(u(\mathbf{x}'))\ d\mathbf{x}' \\ - \sin(d)\int_A W_G(\mathbf{x}-\mathbf{x}')\ d\mathbf{x}'.\end{aligned} \tag{131}$$

Let $k_c(\mathbf{x}),\ k_s(\mathbf{x}),\ k_1(\mathbf{x})$ denote the three respective integrals above. Since W_G is the inverse of the differential operator, we can express these integrals as partial differential equations (PDEs),

$$\begin{aligned}\nabla^2 k_c &= k_c - \cos u(\mathbf{x}),\\ \nabla^2 k_s &= k_s - \sin u(\mathbf{x}),\\ \nabla^2 k_1 &= k_1 - 1,\end{aligned} \tag{132}$$

with no-flux boundary conditions. That is, we can write the integral equation as a set of three PDEs and an algebraic condition:

$$\Omega = \sin(-u(\mathbf{x})+d)k_c(\mathbf{x}) + \cos(-u(\mathbf{x})+d)k_s(\mathbf{x}) - \sin d k_1(\mathbf{x}).$$

(See [47] for many examples of this technique applied to neural field equations.) We note that $k_1 = 1$ satisfies the PDE, so that we do not have to worry about it. We write $u(\mathbf{x}) = \theta + f(r)$ and

$$\begin{aligned}k_s(r,\theta) &= S(r)\cos\theta + C(r)\sin\theta,\\ k_c(r,\theta) &= C(r)\cos\theta - S(r)\sin\theta.\end{aligned}$$

Then we obtain the following differential-algebraic equations:

$$\begin{aligned}\Omega &= C\sin(-f+d) - S\cos(-f+d) - \sin(d),\\ S'' &= S - \sin(f(r)) - \frac{S'}{r} + \frac{S}{r^2},\\ C'' &= C - \cos(f(r)) - \frac{C'}{r} + \frac{C}{r^2},\end{aligned}$$

where the primes denote derivatives with respect to r, $a < r < b$ and the additional boundary conditions $C'(r) = S'(r) = 0$ at $r = a, b$. To remove the algebraic constraint, we differentiate it with respect to r and get

$$f'(r) = \frac{S'(r)\cos(f(r) - d) - C'(r)\sin(f(r) - d)}{C(r)\cos(f(r) - d) + S(r)\sin(f(r) - d)},$$

with $f(a) = 0$ as the boundary condition. Because $f(a) = 0$ we get

$$\Omega = \sin(d)(C(a) - 1) + S(a)\cos(d).$$

Thus, the integral equation becomes a 5-dimensional boundary value problem (BVP). We remark that when $d = 0$, $f(r) = \Omega = S(r) = 0$ as we expect.

Figure 29 shows the behavior of the BVP as we vary d on the annulus with $a = 2, b = 8$ as well as the comparison to the Gaussian kernel case. Panels A,B show the frequency, Ω and the "twist", $f(b)$ as the parameter d varies. The spiral wave can be found up to $d \approx 1.4$ for the Gaussian kernel (c.f. Figure 19), but only to $d \approx 1.2$ for the Green's kernel. Unlike with the integral equations, we are able to follow solutions to the BVP using AUTO [20] and, in fact, find that the solution ends at a saddle-node bifurcation as we hypothesized above. The frequency changes much more with the Green's kernel compared to the Gaussian kernel. The "twist", $f(b)$ (panel B) is quite similar in both cases up until $d \approx 1$ where the two diverge; again the Green's case is more sensitive. In panel C, we continue the fold in d and a in order to see the dependence on the inner radius. For small radii (roughly, $a < 1$) both the Gaussian and the Green's cases tolerate similar values of d. However, for larger a, rotating waves exist for larger values of d in the Gaussian versus the Green's case.

4.4 Discussion

In this chapter, we have used a combination of rigorous mathematical analysis, perturbation theory, and numerical simulations to study the existence, stability, and nature of rotating waves (spiral waves) on an annulus in a non-locally coupled phase model. Rotating waves have been observed in many experimental preparations where they are associated with

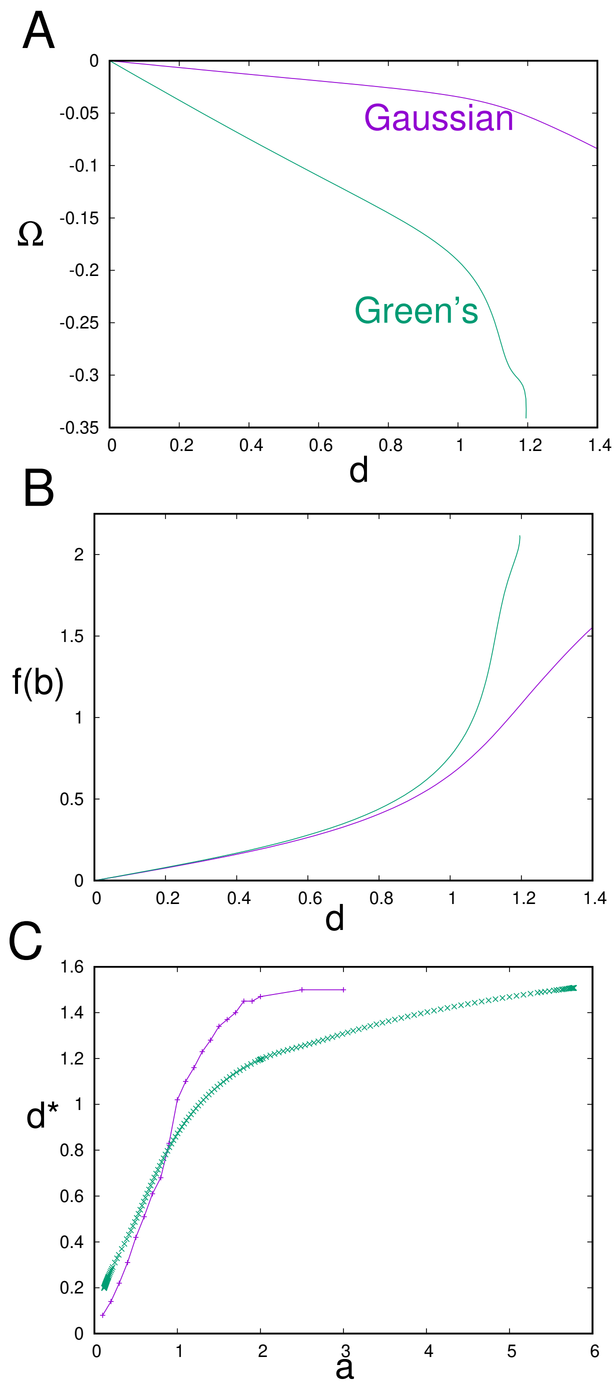

Figure 29: Solutions to Equation (94) on the annulus, $2 < r < 8$ with the Gaussian and Green's function kernels and $H(u) = \sin(u + d) - \sin(d)$. (A,B) behavior of $\Omega, f(b)$ as d varies. (C) Two-parameter continuation of the fold point as a changes. Compare this to Figure 19.

oscillatory electrical brain activity. There have been some papers on spiral waves in non-locally connected phase models, but these have been in the context of spiral chimeras (see Section 4.3.3) and have focused on the contrast between the regular rotating behavior and the complex dynamics in the center. In their analysis of the regular behavior, [51] derived an equation similar to Equation (94) for the Gaussian kernel and $H(u) = \sin(u + d)$ and then obtain an approximate solution for d small by numerically solving the linearized equation.

In [36], the authors numerically solve a non-locally coupled neural field equation when the local dynamics is excitable (as opposed to oscillatory) and find spiral waves. Existence and stability were not discussed beyond the numerical demonstration. Using the approach in [55], we can easily extend the present results to the excitable case by replacing ω in Equation (90) with $\epsilon(1 - \mu \cos(u(\mathbf{x}, t))) \equiv E(u(\mathbf{x}, t))$ where $\mu > 1$ and ϵ is a small positive number. In absence of the coupling, the local dynamics, $u_t = E(u)$ is an excitable system on the circle. In this case, the synchronous solution is then a fixed point, $u(\mathbf{x}, t) = -\arccos(1/\mu)$ and the rotating waves are perturbed to rotating waves in this excitable system.

The motivation for this chapter was to understand some patterns of activity that are observed in large scale brain recordings where rotating waves have been observed. We showed that in the weak coupling limit that conductance based models such as Equation (90) can be reduced to Equation (90) on any spatial domain. All our analysis was confined to some simple examples where $H(u)$ is a sum of only one or two Fourier components. However, in general the function $H(u)$ can have many components, and furthermore $H(0)$ will not generally be 0. It remains to be seen how these differences will affect the behavior of the rotating waves. Additionally, cortical oscillations arise through populations of excitatory and inhibitory neurons; the connections between these neurons can vary in the spatial extent of their "footprint," so another biologically relevant question is how this changes the coupling and the resulting waves. Neural information is communicated at finite speeds, thus there is the possibility of distance-dependent delays in the coupling. These delays are manifested as distance-dependent phase-shifts in the interaction function [14, 38]. Not only do we expect the stability to be affected, but even existence could be altered. In all of the examples we have explored, synchrony is also an attractor. Thus, we can ask how are the spiral waves formed? Can they arise from random initial conditions? What is their basin of attraction?

Wiley et al [69] have addressed this in a ring of discrete oscillators so it is likely that the latter question can be solved if the annulus is narrow. In the supplemental videos, we show an example of a wave emerging from phase randomized initial conditions (see Video S6: randics.mp4) on an annulus with $2 \leq r \leq 10$.

5.0 Local Coupling on Discrete Lattices

5.1 Model

We consider the following spatially discrete dynamical system of locally coupled oscillators,

$$\frac{\partial u_{i,j}}{dt} = H(u_{i,j+1} - u_{i,j}) + H(u_{i,j-1} - u_{i,j}) + H(u_{i+1,j} - u_{i,j}) + H(u_{i-1,j} - u_{i,j}), \qquad 0 \le i, j \le N \tag{133}$$

where $u_{i,j} = u_{i,j}(t) \in [0, 2\pi)$ is a phase oscillator located at the position $(i, j) \in \mathbb{Z}^2$ in a two-dimensional finite square lattice with side lengths N. $H(u)$ is a general 2π periodic nonlinear coupling function or interaction function. Throughout this chapter we make the natural assumption that $H(0) = 0$ for the interaction function $H(u)$. It is a diffusion-like coupling in the sense that if two neighboring oscillators have the same phase, then the coupling term between them is zero and they do not influence each other. Each oscillator is coupled to its 4 neighbors: $u_{i+1,j}$, $u_{i-1,j}$, $u_{i,j+1}$, $u_{i,j-1}$, except for those on the boundary having no interaction with neighbors outside the domain. A no-flux boundary condition is the most appropriate one for this finite size system.

Coupling in the system is referred to as the **nearest-neighbour** coupling with respect to the lattice $\mathbb{Z}^2$. Instead of using more complicated connection topologies, we embed the $2-$dimensional lattice into the real Euclidean plane $\mathbb{R}^2$, where $(x, y) = \{(i/n, j/n)\} : -n \le i, j \le n\}$. So that the embedded point (x, y) lies in a square domain $[-1, 1]^2$, $N = 2n + 1$.

The difference between two nearby oscillators, for example $u_{i+1,j} - u_{i,j}$ is approximated by the Taylor expansion at $u_{i,j} = u(x, y)$, where

$$\begin{aligned} u_{i+1,j} - u_{i,j} &= u((i+1)/n, j/n) - u(i/n, j/n) \\ &= u(x + 1/n, y) - u(x, y) \\ &= \frac{1}{n} u_x + \frac{1}{2n^2} u_{xx} + O(\frac{1}{n^3}), \end{aligned} \tag{134}$$

where u_x, u_{xx} are the first, second partial derivative of u with respect to x. We can get rid of higher order term $O(1/n^3)$ when n is large enough. (The distance $1/n$ between two oscillators is small enough.) Then the discrete model Equation (133) in $\mathbb{R}^2$ is written as

$$\begin{aligned}\frac{\partial u}{\partial t} =& H(\frac{1}{n}u_x + \frac{1}{2n^2}u_{xx}) + H(-\frac{1}{n}u_x + \frac{1}{2n^2}u_{xx}) \\ &+ H(\frac{1}{n}u_y + \frac{1}{2n^2}u_{yy}) + H(-\frac{1}{n}u_y + \frac{1}{2n^2}u_{yy}).\end{aligned} \tag{135}$$

The interaction function $H(u)$ can also be expanded in the Taylor series considering phase differences in u is relatively small compared to other parameters, therefore

$$H(\Delta u) = \alpha \Delta u + \frac{\beta}{2}(\Delta u)^2 + O((\Delta u)^3), \tag{136}$$

where $\alpha = H'(0)$, $\beta = H''(0)$. With this approximation, Equation (135) is further reduced to a reaction-diffusion system of the form

$$\frac{\partial u}{\partial t} = \frac{1}{n^2}\left[\alpha(u_{xx} + u_{yy}) + \beta(u_x^2 + u_y^2)\right], \tag{137}$$

where higher order terms in $O(1/n^4)$ are dropped.

We cut out a unit disk from the square, which is $D = \{(x, y) : x^2 + y^2 <= 1\}$. This restriction to a circular domain reduces the dimensionality of the system thus allows us to explore the rotational symmetry and the spiral wave solution. Under the change of variable $(x, y) = (r\cos\theta, r\sin\theta)$, Equation (137) in polar coordinate is written as

$$\frac{\partial u}{\partial t} = \frac{1}{n^2}\left[\alpha(u_{rr} + \frac{1}{r}u_r + \frac{1}{r^2}u_{\theta\theta}) + \beta(u_r^2 + \frac{1}{r^2}u_\theta^2)\right]. \tag{138}$$

where the disk domain $D = \{(r, \theta) : r \in [0, 1],\ \theta \in [0, 2\pi)\}$.

5.2 Rotating Wave Solutions and Analysis

5.2.1 Continuum equation

We seek for one-armed rotating spiral wave solutions in the polar coordinate of the form:

$$u(r, \theta) = \Omega t + \theta + f(r), \tag{139}$$

where Ω is the collective frequency, and $f(r)$ is the radial phase shift. It is a phase-locked solution in the sense that all solutions have a time-independent phase-lag $\Upsilon(r, \theta) = \theta + f(r)$.

We define the scaled frequency $\omega := n^2\Omega$ which is a constant for a fixed sized square lattice, and it satisfies the following ODE when plugging the phase-lock u (Equation (139)) into the PDE system Equation (138),

$$\omega := n^2\Omega = \alpha(u_{rr} + \frac{1}{r}u_r) + \beta(u_r^2 + \frac{1}{r^2}). \tag{140}$$

In the present Section 5.2, and the simulations in Section 5.3 subsequently, for simplicity, parameter α is set to be 1, otherwise we can divide both sides of Equation (140) by α and study the resulting equation with another frequency ω/α.

Let us denote $v = u_r$, $v' = u_{rr}$, Equation (140) is reduced to a first order ODE where

$$\omega = (v' + \frac{1}{r}v) + \beta(v^2 + \frac{1}{r^2}), \tag{141}$$

along with boundary conditions $v(r_0) = 0,\ v(1) = 0$, where r_0 represents the "core" of the spiral wave. It should be noted that, when taking the inner boundary to zero radius, one encounters a singularity in Equation (141) with Neumann boundary conditions. We have to derive and implement the correct boundary conditions at the core in order to obtain a bounded diffusion term u_r. In this way, we are able to compute the spiral waves on a full disk, as opposed to considering an annulus with a small hole around the core.

We start with an annulus domain and then reduce the inner radius to explore dynamics around the "core". This allows us to avoid the phase-singularity at the "core" of the spiral and still be able to get rotating spiral waves in a spatially continuous phase model. The boundary condition near the "core" is more clear in this case where r_0 is the inner radius of the annulus. Thus the smallest ring in the middle of the square lattice acts as the equivalent of a spiral core in continuous media.

5.2.2 Bessel function solution

In this subsection, we find an analytical approach to this boundary value problem by letting r_0 be sufficiently small. This ODE system Equation (141) can be transferred into a *Bessel equation* by several changes of variables. Let $r = r_0 y$, rewrite Equation (141) as

$$\omega = \frac{1}{r_0} v' + \frac{1}{r_0} \frac{v}{y} + \beta(v^2 + \frac{1}{{r_0}^2 y^2}), \tag{142}$$

then let $z = r_0 v$, it is further reduced to

$$\tilde{\omega} := {r_0}^2 \omega = z' + \frac{z}{y} + \beta(z^2 + \frac{1}{y^2}), \tag{143}$$

along with $z(1) = 0$, $z(1/r_0) = 0$. If we make a *Riccati transformation* by letting $z = \frac{1}{\beta}\frac{\varphi'}{\varphi}$, quadratic terms in Equation (143) are cancelled and the equation is written as

$$y^2\varphi'' + y\varphi' + (\beta^2 - \beta\tilde{\omega}y^2)\varphi = 0, \tag{144}$$

with boundary conditions $\varphi'(1) = 0$, $\varphi'(1/r_0) = 0$. Make another change of variable that $x = \sqrt{\tilde{\omega}\beta}y$, Equation (144) can be simplified to a *modified Bessel equation*:

$$x^2\varphi'' + x\varphi' + (\beta^2 - x^2)\varphi = 0, \tag{145}$$

with boundary conditions $\varphi'(\sqrt{\tilde{\omega}\beta}) = 0$, $\varphi'(\sqrt{\tilde{\omega}\beta}/r_0) = 0$.

It has an equivalent form

$$x^2\varphi'' + x\varphi' - (x^2 + \alpha^2)\varphi = 0, \tag{146}$$

where $\alpha = \beta\mathrm{i}$.

There is an analytical solution to Equation (145), which is a linear combination of two *modified Bessel functions* $I_{\beta\mathrm{i}}$ and $K_{\beta\mathrm{i}}$,

$$\varphi(x) = c_1 I_{\beta\mathrm{i}}(x) + c_2 K_{\beta\mathrm{i}}(x), \tag{147}$$

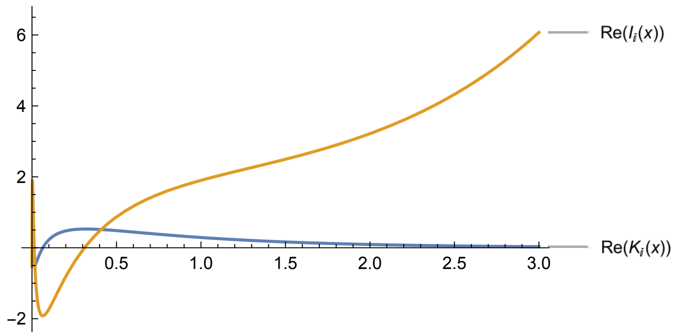

Figure 30: Real parts of modified Bessel functions: $\Re[I_{\mathrm{i}}(x)]$, $\Re[K_{\mathrm{i}}(x)]$. $\beta = 1$.

where c_1 and c_2 are two constants.

Only real solutions will be considered in the biological systems, therefore we plot the real parts of two modified Bessel functions in Figure 30. Note that we use $\beta = 1$ for this plot, but any positive or negative β gives a similar shape. In order to fit the boundary condition $\varphi'(\sqrt{\tilde{\omega}\beta}/r_0) = 0$ for small r_0, we use the dominate *Bessel K* function to approximate the solution, therefore

$$\varphi(x) = \Re[K_{\beta\mathrm{i}}(x)]. \tag{148}$$

Let x_0 be a root such that $\varphi'(x_0) = 0$, which corresponding to the inner boundary condition that $\varphi'(\sqrt{\tilde{\omega}\beta}) = 0$. We can solve for ω using $x_0 = \sqrt{\tilde{\omega}\beta}$, thus

$$\omega = \frac{\tilde{\omega}}{r_0^2} = \frac{x_0^2/\beta}{r_0^2}. \tag{149}$$

As an example, we take $\beta = 0.4$ in the interaction function H. Since $x_0 = 0.0235$ is a zero of φ' as defined in Equation (148), frequency from the Bessel solution satisfies $\omega = 0.00138/r_0^2$. It can be compared to the numerically solved ω from the BVP Equation (141) with the "shooting" method, as shown in Figure 31. The Bessel solution is a good approximation to the actual BVP Equation (141) when the inner radius r_0 is a small quantity.

Furthermore, we can integrate φ to calculate z in Equation (143), where $z = \frac{1}{\beta}g$, thus

$$g(x) = \int_{x_0}^{x} \frac{\varphi'(x)}{\varphi(x)}\, dx = \ln \frac{\varphi(x)}{\varphi(x_0)}, \tag{150}$$

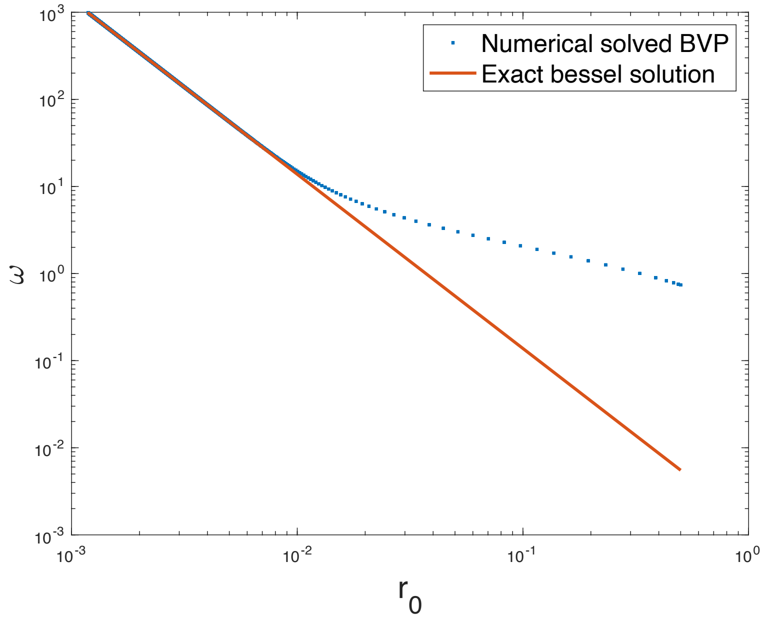

Figure 31: Log-log plot of ω vs r_0 when $\beta = 0.4$: Blue dots: numerical solved BVP; Red line: Bessel solution approximation, given by Equation (149).

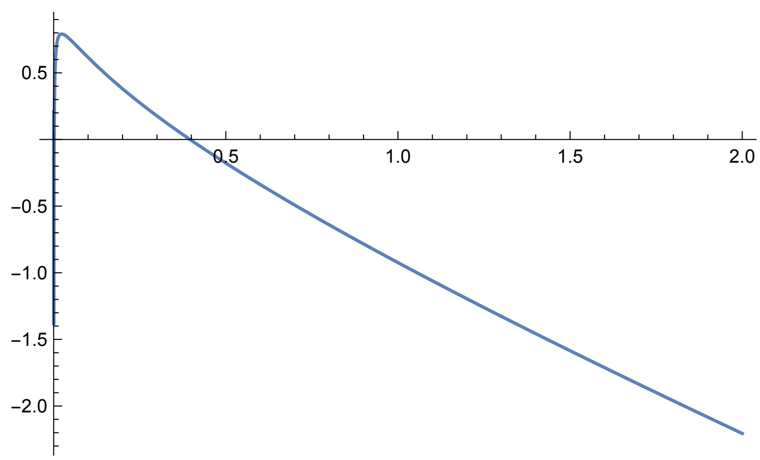

Figure 32: The function $g(x)$ defined in Equation (150) (when $\beta = 0.4$), which is a multiple of diffusion term u_r.

The function g is almost linear in x according to the plot Figure 32, as well as z and the diffusion term u_r.

5.3 Simulation

The next question is, how does the system on continuous spatial domain compare to the original discrete lattice domain? For simulations of the discrete system Equation (133), we use a general periodic interaction function H represented by its first two Fourier modes in the following form:

$$H(u) = b_1(1 - \cos(u)) + b_2(1 - \cos(2u)) + a_1 \sin(u) + a_2 \sin(2u). \tag{151}$$

According to the study on discrete system [19], for odd interaction function $H(u)$ ($b_1 = 0$ and $b_2 = 0$), there is a synchronous solution $u \equiv 0$ and it is asymptotically stable provided that $H'(0) > 0$. Moreover, there is a "straight-armed" radical wave solution satisfies $u_{ij} = \text{atan2}(j, i)$. Because of this, we initialize u from the "straight-armed" wave $u = \theta$ with small noise, and let $u(i, j, 0) = \text{atan2}(j, i) + \epsilon N(0, 1)$, where (i, j) is the position on the square lattice, and $N(0, 1)$ is a normal random variable. Then integrate the discretized system Equation (133) with Euler's method for longer enough time steps until steady states have been reached. The effect of even part of interaction function $H(u)$ gives the spiral waves their "twist" as shown in Figure 33.

5.3.1 Discrete cores

For simulations on the **annulus** domain, we introduce RS as the squared inner radius on the lattice grid and it is truncated to be an integer. Since some values of RS give the same cores on the lattice, (for example, $RS = 3$ and 4; $RS = 5$ and 6,) we skip some natural numbers and simulate the discrete ODE Equation (133) with $RS = 0,\ 1,\ 2,\ 3,\ 5,\ 7,\ 9$. Cores on a square lattice of different sizes are shown in Figure 34. We use the odd value N, which makes it easier to locate the center of the core. For even N, cores are looking differently,

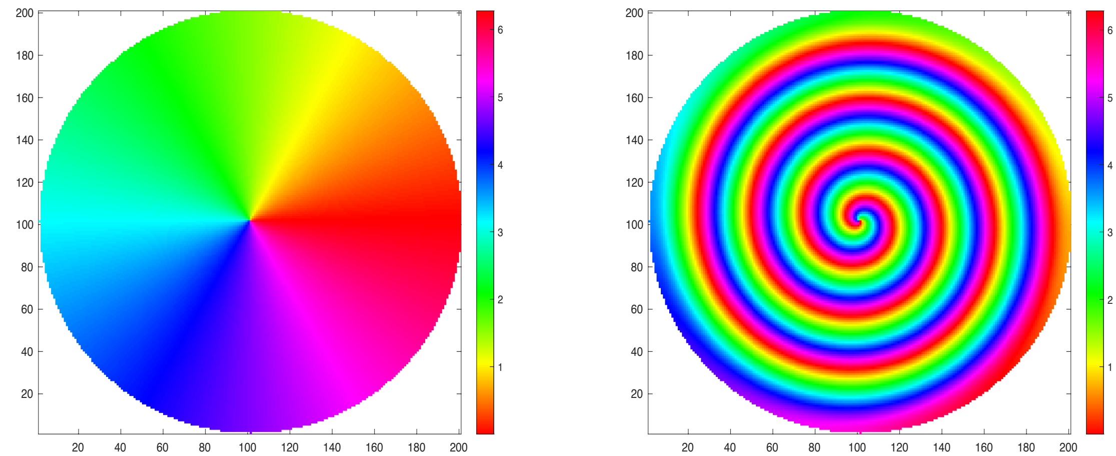

Figure 33: Spiral wave from simulations of Equation (133) on a disk domain cut from a 201×201 square lattice. Parameters in interaction function are left (odd interaction function $H(u)$): $b_1 = 0,\ b_2 = 0,\ a_1 = 1,\ a_2 = 0$; right ($H(u)$ with even component): $b_1 = 0.4,\ b_2 = 0,\ a_1 = 1,\ a_2 = 0$.

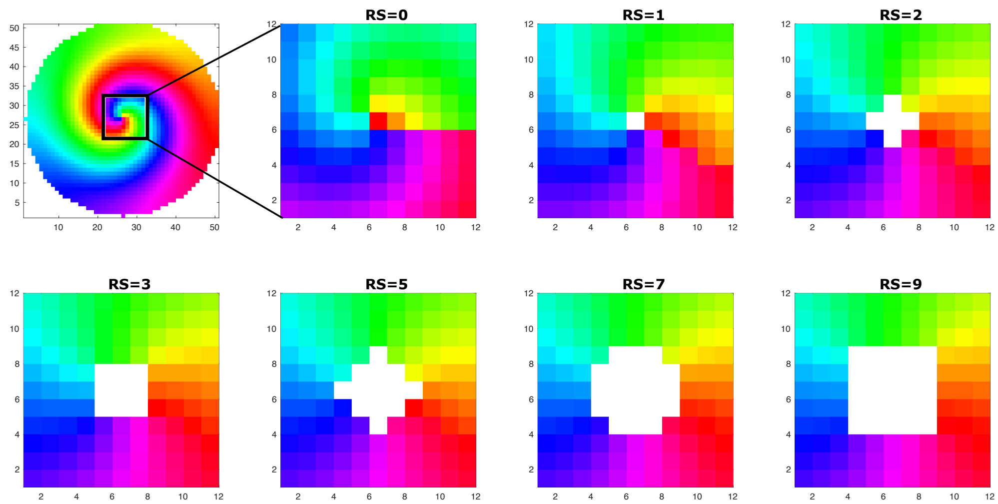

Figure 34: Cores of different sizes from 51×51 square lattice grid.

while the simulation results of the frequency Ω and the phase-shift $f(r)$ are similar, and give similar spiral wave patterns.

Spiral wave simulation results in Figure 35 show that the smaller the “hole” is, the more “twist” the wave has. There are two ways to make a smaller “hole”: one is increasing the lattice size, making finer mesh, such as (a), (b), (c) in Figure 35; the other one is changing the “hole” size, cutting out less points around the core, such as (c), (e), (f) in Figure 35. If we remove the “hole” (Figure 35 (d)), the resulting spiral is drastically different from what it looks with only one “hole” (Figure 35 (c)). This suggests that phase singularity also exists in the discrete system.

As far as phase variable u is concerned, we are now looking at other related quantities in detail. In Figure 36, the collective frequency Ω and total increment f_d in phase-lag term f are plotted with $n = 25, 50, 100, 200$. If the “hole” size RS is fixed, frequency Ω is convergent as n increasing. The increment f_d doubles in size as n doubled which is indicated by the linear log plot on the left of Figure 36.

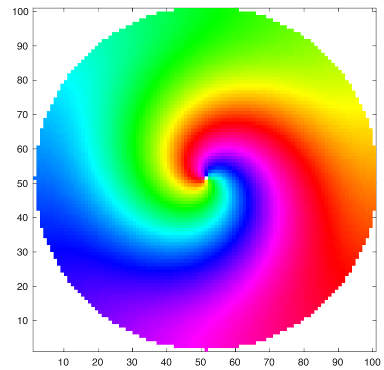

(a) 101×101 lattice with 1 hole.

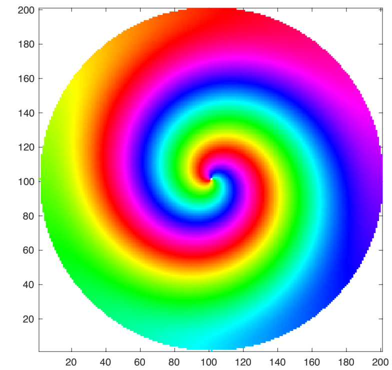

(b) 201×201 lattice with 1 hole.

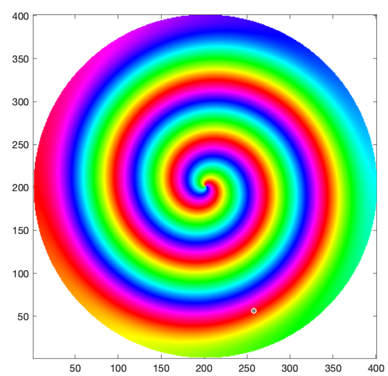

(c) 401×401 lattice with 1 hole.

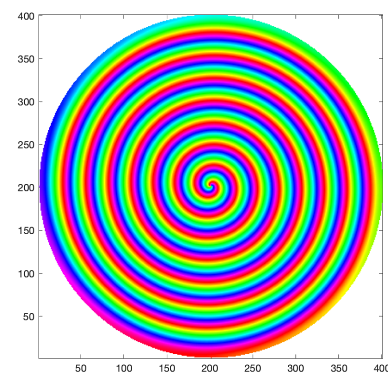

(d) 401×401 lattice with no hole.

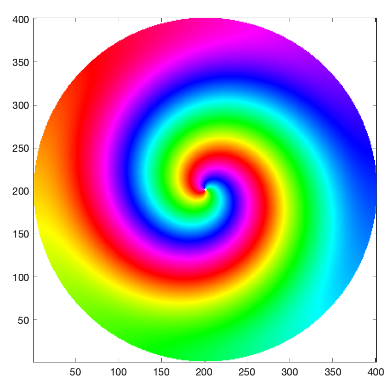

(e) 401×401 lattice with $RS = 2$.

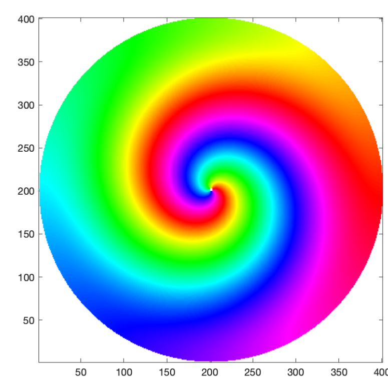

(f) 401×401 lattice with $RS = 3$.

Figure 35: Spiral waves in different sizesquare lattice of different sizes and holes.

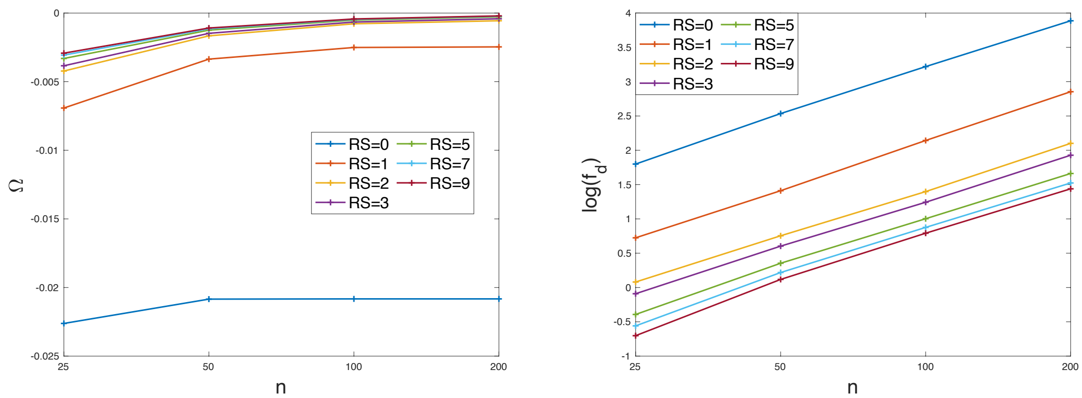

Figure 36: Discrete simulations on lattice. Left: frequency Ω vs lattice size n; Right: increment in phase-lag $\log(f_d)$ vs lattice size n.

5.3.2 Matching and scaling

Here we attempt to investigate the relationship between the discrete system and the continuous system. Remember there is a undetermined parameter which is the inner boundary r_0 in the continuous Equation (141). For the annulus domain, r_0 is the inner radius. It is proportional to the distance between two adjacent oscillator, $1/n$, and it also depends on the size of the "hole" in the discrete lattice. For the disk domain, r_0 cannot be 0 because of the phase singularity as discussed in Section 5.2.1. However, simulations in Section 5.3 show that spiral wave solutions do exist for disk domain of the discrete system Equation (133). It is because the middle 4 oscillators in the "core" of the square lattice have large phase differences ($\geq \pi/2$). That forms a chain of 4 oscillators which can be regarded as a virtual "hole" in the disk and r_0 should be the radius of this virtual "hole" (see Figure 37 left panel).

Using the interaction function $H(u)$ defined in Equation (151), parameters in the boundary value problem Equation (141) are satisfying $\alpha = a_1 + 4a_2$, $\beta = b_1 + 4b_2$. The numerical results of the boundary value problem Equation (141) solved from XPP AUTO are compared to the discrete simulations. We vary inner radius r_0 in its boundary conditions to obtain $\omega(r_0)$, and integrate u_r to get $f(r)$ (where $f' = u_r$ and $f(r_0) = 0$). For discrete simulations of Equation (133), the increment in the phase-lag term f is defined as

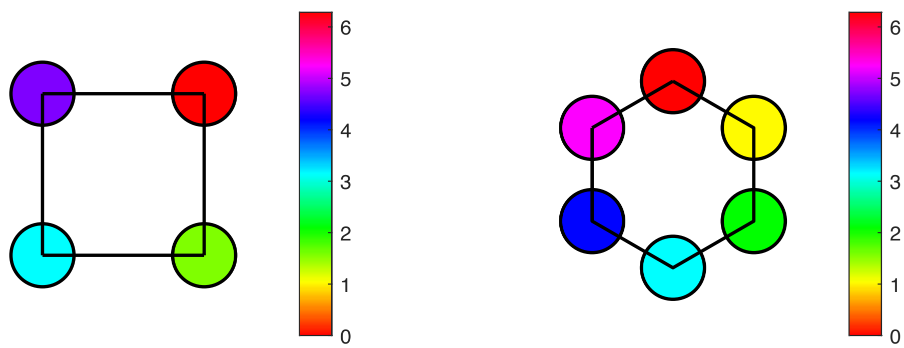

Figure 37: The virtual "hole" in discrete lattices. Colors indicate the phase of the oscillator. Left: middle 4 oscillators in the square lattice, phase differences between two adjacent oscillators are $\pi/2$. Right: middle 6 oscillators in the hexagonal lattice (will be discussed in Section 5.4), phase differences between two adjacent oscillators are $\pi/3$.

$f_d := f(2n+1) - f(n+1+\lfloor m \rfloor)$. We let $m = \sqrt{RS+1}$ be the starting point from the core. Then for a disk, $m = 1$, for an annulus with one hole $RS = 1$, $m = \sqrt{2}$, for the squared inner radius $RS = 4$, $m = 2$. The number of points which been removed from the core is not a constant increment, therefore m can be a non-integer. We match f and f_d from both methods, and regard them as referring to the same system, as demonstrated by Figure 38. Inner radius in continuous BVP is r_0 versus in discrete ode is m and the collective frequency should have the relation $\omega = n^2\Omega$ as suggested in Equation (140). The hypothesis is for any fixed domain, r_0 proportional to $1/n$, and depends on the size of the "hole", $r_0 = cm/n$, where c is a scaling factor. We find through comparisons in Table 1, Table 2 and Table 3: for annulus domain (where $RS >= 2$), the ratio $c = (nr0)/m \approx 1$; for annulus with one single hole where $RS = 1$, $c = (nr0)/\sqrt{2} \approx 0.5$, for no hole (disk domain), $c = nr0 \approx 0.25$. These tables contain data from both discrete simulations (yellow part) and numerical solution of continuous ODE (blue part), and indicates their relation by calculating the scale factor c (red part).

Changes with respect to the increasing lattice size n in scaling factor c are shown in Figure 39, c converges to 1 as the lattice grows. We also investigate the system with interaction function $H(u)$ with higher mode even term where $b_1 = 0$ and $b_2 \neq 0$. The parameter is selected such that it is referring to the same system in the continuous equation thus $b_1 = 4b_2$. From Table 4 and right panel in Figure 39, we found the scaling factor $c \approx 0.5$ for no "hole" lattice and converges to 1 after $NS = 2$.

5.4 Hexagonal Lattice

The hexagon is a different shape that may be used to tessellate the plane, and this naturally produces a network with exactly three vertices at each node (apart from the outside boundary). It would be useful at this stage to consider locally coupled oscillators on a hexagonal lattice.

There are two types of coupling in a hexagonal lattice as shown in Figure 40, those are, red connection: an oscillator is connecting to its upper, lower left and lower right; blue

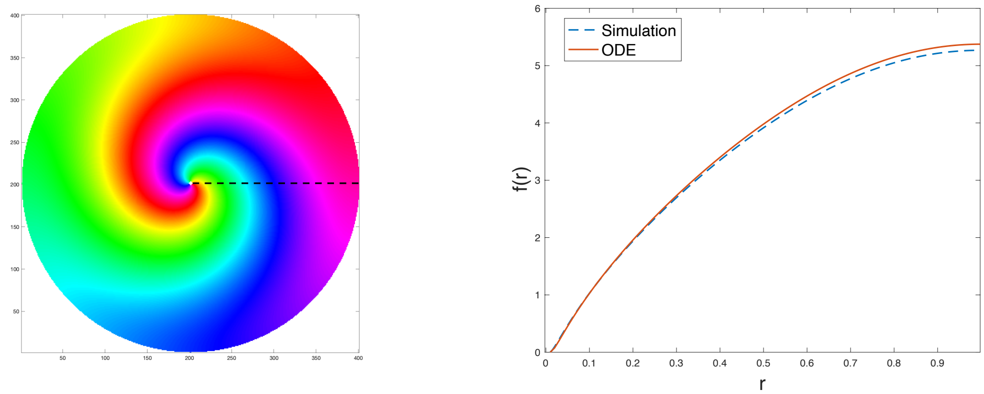

Figure 38: Left: simulation from discrete system with $n = 200$, $RS = 5$, $b_1 = 0.4$, phase-lag $f(r)$ is calculated on the dotted line. Right: compare $f(r)$ on black dash line at the left with numerical solved ODE using inner radius $r_0 = 0.012$.

n	RS	Ω	f_d	f	$r0$	ω	$n^2\Omega$	c
50	0	0.020847	12.618624	12.6319	0.00521865	50.815498	52.1175	0.2609325
50	1	0.003356	4.099006	4.05835	0.0158939	7.8376298	8.39	0.561934223
50	2	0.00166	2.125106	2.15589	0.0315047	4.1856999	4.15	0.909462351
50	3	0.001476	1.82749	1.88092	0.0365189	3.76648	3.69	0.9129725
50	5	0.001246	1.424349	1.45453	0.0478973	3.15171	3.115	0.977699542
50	7	0.001144	1.243998	1.22172	0.0571502	2.8285999	2.86	1.010282349
50	9	0.001089	1.124932	1.09892	0.0633979	2.65995	2.7225	1.002408814

Table 1: Comparison of discrete and continuous system with parameters: $n = 50$; $a_1 = 1$; $a_2 = 0$; $b_1 = 0.4$; $b_2 = 0$.

n	RS	Ω	f_d	f	$r0$	ω	$n^2\Omega$	c
100	0	0.02083	25.015826	25.0171	0.00259318	205.57001	208.3	0.259318
100	1	0.002508	8.521684	8.56003	0.00761818	24.2904	25.08	0.538686674
100	2	0.000782	4.045906	4.05835	0.0158939	7.8376298	7.82	0.917634744
100	3	0.000654	3.464216	3.47982	0.0187067	6.5647998	6.54	0.935335
100	5	0.000513	2.724958	2.6609	0.0250308	5.0157599	5.13	1.021878131
100	7	0.000458	2.40093	2.47938	0.0270431	4.7076001	4.58	0.95611797
100	9	0.00043	2.206331	2.15589	0.0315047	4.1856999	4.3	0.99626609

Table 2: Comparison of discrete and continuous system with parameters: $n = 100$; $a_1 = 1$; $a_2 = 0$; $b_1 = 0.4$; $b_2 = 0$.

n	RS	Ω	f_d	f	$r0$	ω	$n^2\Omega$	c
200	0	0.02083	48.785053	48.7879	0.00129139	828.914	833.2	0.258278
200	1	0.002465	17.347083	17.3554	0.00378575	96.4571	98.6	0.535385899
200	2	0.00056	8.173516	8.16953	0.00796556	22.350599	22.4	0.919783642
200	3	0.000416	6.874697	6.8588	0.00941426	16.582899	16.64	0.941426
200	5	0.000277	5.267872	5.23699	0.0122491	10.9623	11.08	1.000134827
200	7	0.000229	4.588308	4.59036	0.0139922	9.15518	9.16	0.98939795
200	9	0.000206	4.213737	4.24059	0.0151827	8.2724705	8.24	0.960238261

Table 3: Comparison of discrete and continuous system with parameters: $n = 200$; $a_1 = 1$; $a_2 = 0$; $b_1 = 0.4$; $b_2 = 0$.

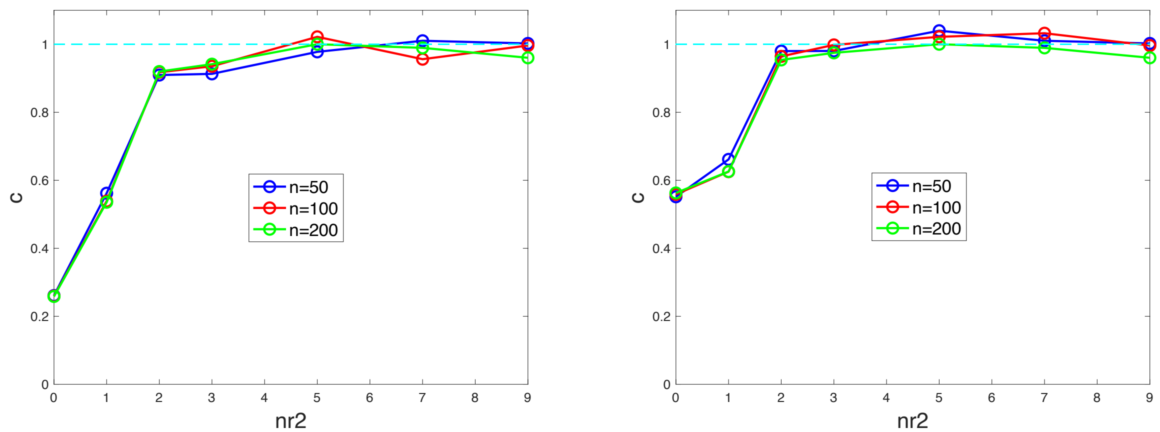

Figure 39: left: $b_1 = 0.4$, $b_2 = 0$; Right $b_1 = 0$, $b_2 = 0.1$ $N = 50$ (blue); 100 (red); 200 (green); dash line $c = 1$.

n	RS	Ω	f_d	f	$r0$	ω	$n^2\Omega$	c
100	0	0.004267	11.824701	11.7931	0.00558579	44.396198	42.67	0.558579
100	1	0.001877	7.271137	7.32263	0.00884261	18.494699	18.77	0.625266949
100	2	0.00075	3.913241	3.87093	0.0167033	7.4077401	7.5	0.964365475
100	3	0.000634	3.377576	3.27583	0.0199625	6.1528101	6.34	0.998125
100	5	0.000506	2.688423	2.6609	0.0250308	5.0157599	5.06	1.021878131
100	7	0.000453	2.375869	2.31124	0.029202	4.4321799	4.53	1.032446611
100	9	0.000426	2.185676	2.15589	0.0315047	4.1856999	4.26	0.99626609

Table 4: Comparison of discrete and continuous system with parameters: $n = 200$; $b_1 = 0$; $b_2 = 0.1$.

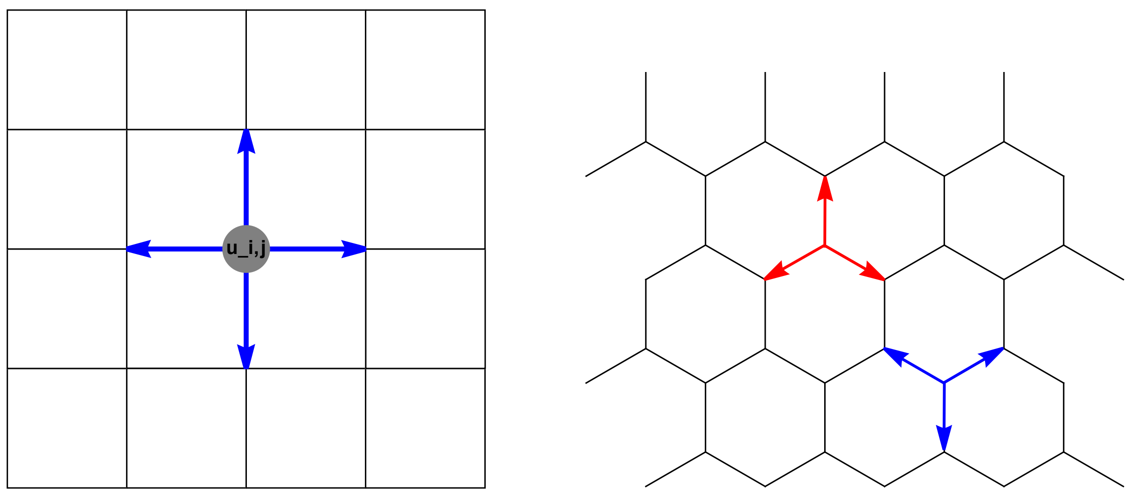

Figure 40: Left: connections on square lattice; Right: connections on hexagonal lattice

connection: an oscillator is connecting to its lower, upper left and upper right. Therefore the dynamics of oscillators are governed by the following two differential equations,

$$\begin{aligned}
\frac{\partial u_{i,j}}{dt} &= H(u_{i,j+1} - u_{i,j}) + H(u_{i,j-1} - u_{i,j}) + H(u_{i+1,j} - u_{i,j}), \quad \text{(blue connection)} \\
\frac{\partial u_{i,j}}{dt} &= H(u_{i,j+1} - u_{i,j}) + H(u_{i,j-1} - u_{i,j}) + H(u_{i-1,j} - u_{i,j}), \quad \text{(red connection)} \\
& \qquad -n \leq i, j \leq n,
\end{aligned} \tag{152}$$

where $u_{i-1,j}$, $u_{i+1,j}$ represent the upper neighbor in red connection and lower neighbor in blue connection, $u_{i,j-1}$, $u_{i,j+1}$ represent the left neighbor and the right neighbor in both connections. Since the number of red connections and blue connections are the same on a large symmetric hexagonal lattice. Chances of getting each type of connection for any random oscillator in the lattice is 1/2, thus Equation (152) can be approximated by,

$$\begin{aligned}
\frac{\partial u_{i,j}}{dt} &= H(u_{i,j+1} - u_{i,j}) + H(u_{i,j-1} - u_{i,j}) + \frac{1}{2}H(u_{i+1,j} - u_{i,j}) + \frac{1}{2}H(u_{i-1,j} - u_{i,j}), \\
& \qquad -n \leq i, j \leq n.
\end{aligned} \tag{153}$$

The hexagonal lattice can also be mapped into a regular Euclidian space $\mathbb{R}^2$, thus Taylor expansion is applied to Equation (153), the corresponding system in a spatially continuous domain is

$$\frac{\partial u}{\partial t} = \frac{1}{n^2}\left[\alpha(u_{xx} + \frac{1}{2}u_{yy}) + \beta(u_x^2 + \frac{1}{2}u_y^2)\right]. \tag{154}$$

Immediately, one could notice that Equation (154) is the same as the continuum equation Equation (137) derived from square lattice with one change of variable $\hat{y} = \sqrt{2}y$.

5.4.1 Simulations on hexagonal lattice

Simulation for hexagonal lattice is similar to the square lattice case. We distinguish between the points by red connection or blue connection depending on their position on the lattice domain. The numbering scheme for vertices of the hexagonal lattice is shown in Figure 41. We employ a $N \times N$ (where $N = 2n + 1$) grid, since horizontal numbers are more dense than the vertical numbers on hexagonal lattice, it ends up being a rectangular region with side-to-side ratio $\sqrt{3} : 1$ (vertical : horizontal) as illustrated in Figure 42. As before, we cut out a disk region, start with a straight-armed initial condition and integrate the discretized ODE system with Euler's method.

We compare simulations of hexagonal lattices to square lattices. Since they are both approximated by the continuous system Equation (141), their solutions should be similar. Use parameters $b_1 = 0.4$ and $b_2 = 0$ for the interaction function, and the size of the mesh is $N = 101$. The size of the spiral formed from a hexagonal lattice is almost half the size of it on a square lattice. If we zoom in on the square lattice spiral, and compare it to the hexagonal lattice spiral side-by-side, they are almost the same as illustrated in Figure 43. We make a horizontal cut from the disk and calculate the phase-lag term f. The original f_i ($i = 1 \ldots 50$) are shown in lines in Figure 44. If the whole hexagonal $f(r)$ is compared to the first half of square $f(r)$ which is indicated by the dotted line $f(2r)$, they are matching pretty well.

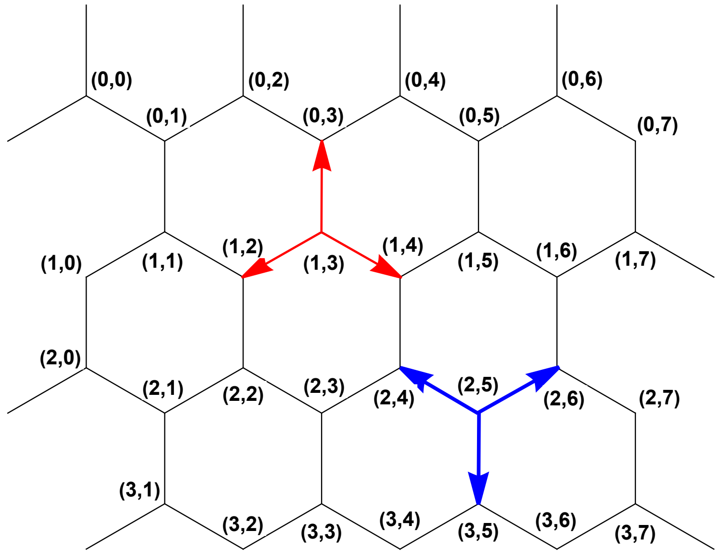

Figure 41: Numbering scheme and two types of connections.

5.5 Discussion

In previous chapters, we were focusing on wave patterns generated from non-locally coupled oscillators. In the spatial locally coupled case this generally involves systems of reaction-diffusion equations. The existence of rotating waves has been proved in [55] for an oscillatory reaction-diffusion equation with Neumann boundary conditions. In order to avoid the phase-singularity at the core of spirals, many research has been carried out in Lambda-Omega systems [56, 10]. There are some other approaches to phase equations, for example, implementing alternative boundary conditions that allow for continuing the inner radius to zero [34]; obtaining the phase components in the anti-continuum limit [8]. We approximate the rotating wave on an annulus with a small inner radius while keeping the Neumann boundary condition.

In the continuum limit, we show the local coupling on the lattice can be interpreted as a finite difference discretization of the partial differential equation (PDE) for reaction-diffusion systems. For rotating wave solutions in an annular region, this equation is reduced

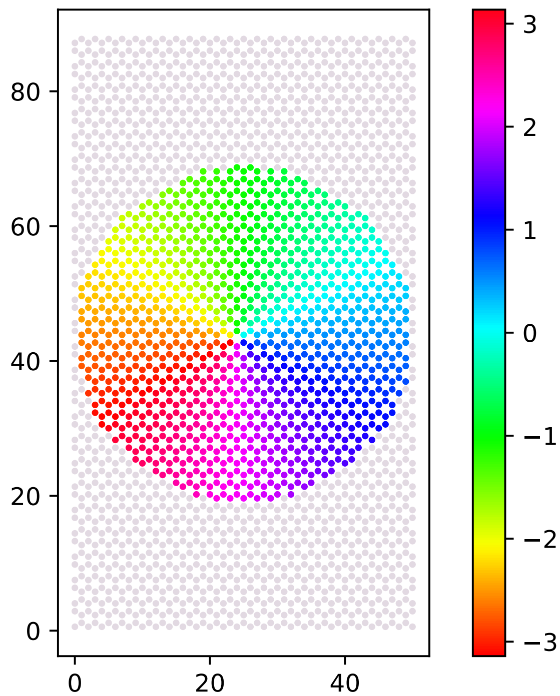

Figure 42: Straight-armed wave solution on 51×51 hexagonal lattice grid. Side-to-side ratio of the domain is $\sqrt{3} : 1$.

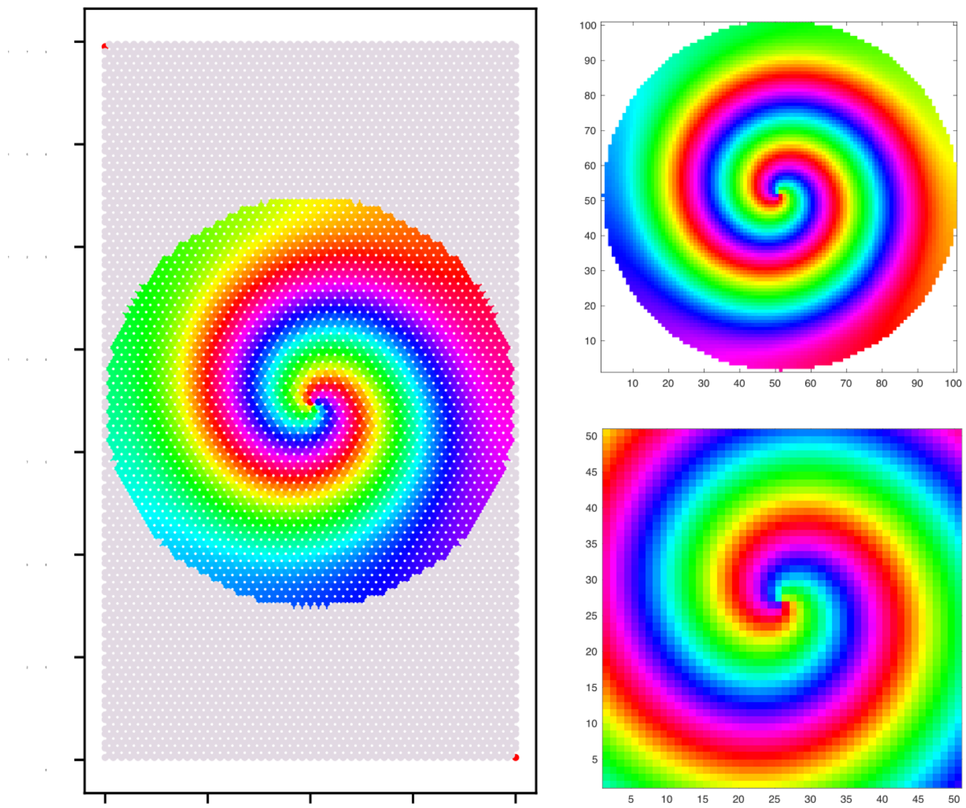

Figure 43: Comparison between square lattice and hexagonal lattice. Left: spiral wave on a hexagonal lattice. Upper right: spiral wave on a square lattice. Lower right: zoom in on the spiral wave on a square lattice. Interaction function: $H(u) = \sin u + 0.4(1 - \cos u)$. Lattice size: $n = 50$.

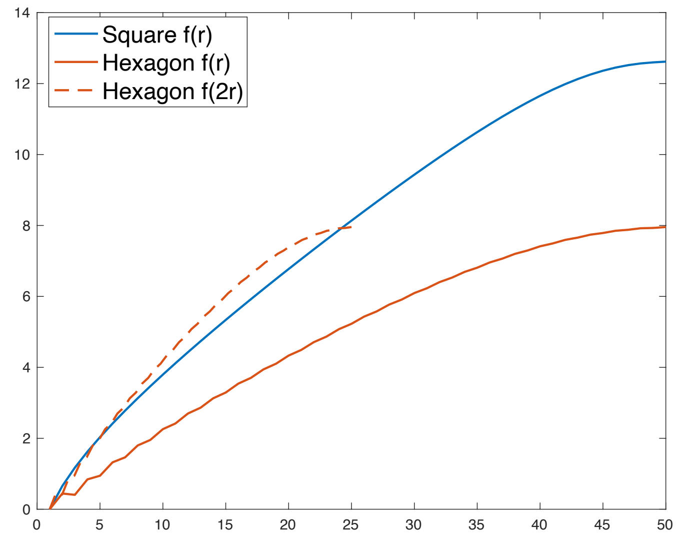

Figure 44: Phase-lag term $f(r)$ obtained from simulations. Blue line: square lattice; red line: hexagonal lattice; red dash line: hexagonal lattice with the scaled domain.

to a boundary value problem (BVP) of an ordinary differential equation (ODE). As inner radius $r_0 \to 0$, we find an exact solution to the BVP in the form of the Bessel function.

In the discrete framework, both square lattice and hexagonal lattice are considered for the coupled system. Our numerical simulation results showed that continuum approximation describes the solutions of the discrete system under the condition that there is a hole in the middle of the spiral "core". While in the continuous media the smallest rings of oscillators in an annulus domain can be regarded as a spiral core, they are not equivalent due to the differences in topology.

The goal of this chapter is to understand the rotating waves occurring in a locally coupled system of phase oscillators on annular domains. It should be notice that based on the local coupling setting, those arguments in continuum limit are more realistic in reaction-diffusion systems. However, a challenging task is to locate and determine the inner boundary of the spiral "core". Future research could continue to explore conditions that are suitable for this kind of system.

In sum, we study the locally coupled oscillators on discrete lattices. Simulation shows that for the square lattice with $N \times N$ grids, twisted-armed rotating waves emerge when the coupling includes non-odd components; spiral waves blows up at the core. As $N \to \infty$, the system can be described by Bessel equation on an annulus with an inner radius proportional to $1/N$. We provide a way to calculate spiral waves in the full disk while avoiding phase-singularity in the continuum limit.

6.0 Conclusions and Future Work

6.1 Conclusions

In Chapter 2, we have shown that a continuum network of non-locally coupled oscillators that show stable synchrony is able to additionally support stable traveling waves on rings that are sufficiently long. Traveling phase waves have been shown to occur in the cortex and our work shows that such behavior is expected whenever are intrinsically oscillatory dynamics and synchronizing coupling.

In Chapter 3 and 4, we have demonstrated the existence of rotating waves on the annulus for non-locally coupled oscillators. Most interestingly we saw that even terms in the phase interaction function are responsible for the amount of "twist" in the waves for phase-difference coupling while not necessary for pulse coupling. Shrinking the inner radius or extending the outer radius are both supposed to amplify this "twist" but having different forces in between phase-difference coupling and pulse coupling. Moreover, the simulation results found that as the inner radius of the hole shrinks, we can expect to see instabilities or complex behavior at the center (spiral chimeras) due to the loss of the existence of the rotating wave through a saddle-node bifurcation. Using perturbation arguments, approximations, and numerics, we characterized both the form and the stability of rotating waves in non-locally coupled phase oscillators on annular domains.

Finally, in Chapter 5, we investigated a discrete system of locally coupled phase oscillators on $N \times N$ lattice grids and showed that when the coupling includes non-odd components, twisted-armed rotating waves emerge. As $N \to \infty$ that the dynamics can be understood by a Bessel equation on an annulus with an inner radius proportional to $1/N$. We also provided a method to calculate rotating waves in the full disk while avoiding phase-singularity in the continuum limit.

6.2 Future Work

6.2.1 Amplitude-phase model

Depending on the choices of the coupling kernel and the interaction function, we have found that the existence and stability of rigid rotating waves are generally limited to annuli that have a finite inner radius. A natural question is whether this fact is a consequence of our restricting the dynamics to lie on a circle, e.g. a phase model. We first note that spiral chimeras (which we saw are a consequence of the central core of the annulus shrinking) have been found in the Fitzhugh-Nagumo model [31] which is not a phase model but includes amplitude. Thus, we can ask whether the additional degree of freedom conferred by amplitude allows rotating waves in oscillatory media to exist as the inner radius goes to zero. A simple model which maps onto our present example is the non-locally coupled normal form near a Hopf bifurcation:

$$z_t(\mathbf{x}, t) = zg(|z|) + K \int_A W(|\mathbf{x} - \mathbf{x}'|^2)[z(\mathbf{x}', t) - z(\mathbf{x}, t)]\ d\mathbf{x}', \tag{155}$$

where $g(|z|) = (1 + iq)(1 - |z|^2)$. Following [32], one looks for rotating wave solutions that have the form: $z(\mathbf{x}, t) = \rho(r) \exp(i[\Omega t + \theta + f(r)])$ leading to a pair of integral equations for $\rho(r), f(r)$. [39] derives a normal form for general oscillatory media with non-local coupling and proves that solutions exist to these equations on the whole plane and $W(R) = w(R/\epsilon^2)/\epsilon^2$ for sufficiently small ϵ. We remark that in this limit, the resulting integral equations become a Burger's type BVP [25].

6.2.2 Robustness of waves

So far we have only studied the local stability of the wave patterns. A natural question is to ask how robust the wave is? Or a qualitative question would be what is the size of basin of waves? Wiley et al [69] first brought up this type of question, and have provided an example on the ring model of identical phase oscillators. The basin of attractions of chimera states [17] or other patterns [3] have been addressed in oscillatory systems. All their approaches have

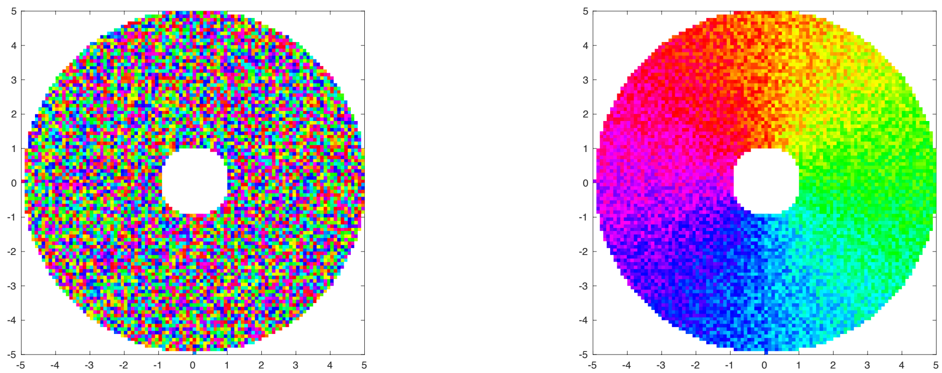

Figure 45: Initial conditions on the annulus with radii $[1, 5]$. Left: random initial condition $u = 2\pi\mathcal{N}(0, 1)$; Right: perturbed straight arm wave initial condition $u = \theta + 2\pi\epsilon\mathcal{N}(0, 1)$ where $\epsilon = 0.1$. $\mathcal{N}$ is the Normal distribution.

included numerical simulations to measure the size of basin. Our simulations in the phase-difference coupled oscillators (the model in Chapter 4) illustrated that different coupling strengths might be relevant: starting from a random initial condition on the same annulus region, coupling strength $K = 1$ forms a wave solution while weaker coupling $K = 0.2$ leads to synchrony (see Video S7: wave_phase.mp4, Video S8: sync_phase.mp4 in Supplementary). We also noticed that it is harder to find a wave pattern with the random initial condition for pulse coupled oscillators (discussed in Chapter 3), besides the synchrony states (see Video S9: sync_pulse.mp4), it could reach a rest state which is known as oscillator death [27] when the coupling strength is getting larger (see Video S10: rantodeath.mp4, wavetodeath.mp4).

6.2.3 Heterogeneity of natural frequencies

It is important to consider the effect of heterogeneities in the dynamics. The intrinsic frequency of the oscillator may change due to the heterogeneous medium. A recent study [40] showed the robustness of the stability of the planar wave against the heterogeneity of natural frequencies. Instead of identical oscillators, pacemaker oscillators can be used in the phase model by submitting the constant frequency term with a Mexican hat function $\omega(\mathbf{x})$:

$$\frac{du}{dt} = \omega(\mathbf{x}) + \int_D W(|\mathbf{x} - \mathbf{x}'|)H(u(\mathbf{x}') - u(\mathbf{x}))d\mathbf{x}. \tag{156}$$

At this stage of understanding, we believe that the singular perturbation method could be applied to this equation and gives us analytical insight. As an example, we remark that Equation (156) in one-dimensional ring domain $x \in [0, L)$ with frequency distribution $\omega(x) = \kappa x$ admits the relation $\Omega \propto \kappa$, where Ω is the collective frequency of the oscillators.

6.2.4 Asymmetric coupling

In [6] asymmetric couplings were exploited to find traveling chimera states in a system of phase oscillators. It would be interesting to see the effect of asymmetric coupling in wave patterns. Our simulations in discrete coupled oscillators suggested that changing the connection weights can change the stability of solutions. In the square lattice model, when changing connection weight in one direction, the core of the rotating wave drifts away and makes all the oscillators synchronized. However, if the changes are made in two (opposite) directions, waves are stretched or squeezed if the difference in connection weight is not too large. Simulation results are shown in Figure 46 when the locally coupled system Equation (133) is equipped with a connection weight k at the horizontal direction:

$$\frac{\partial u_{i,j}}{dt} = kH(u_{i,j+1} - u_{i,j}) + kH(u_{i,j-1} - u_{i,j}) + H(u_{i+1,j} - u_{i,j}) + H(u_{i-1,j} - u_{i,j}). \tag{157}$$

Future investigation should consider the analytical aspect of those observations and find an asymmetric coupling kernel in the continuum limit.

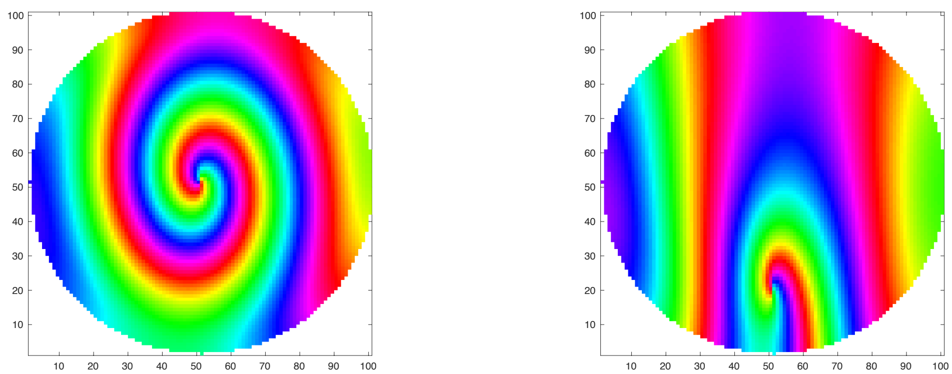

Figure 46: Simulation result on square lattice of size $N = 101$. Left: connection weight $k = 0.5$, spiral wave is squeezed horizontally; Right: connection weight $k = 0.2$, this is a middle state, solution finally goes to synchrony.

Appendix Supplemental Information

Supplemental Information includes 13 videos. Codes to generate videos can be found online at https://github.com/jjjoyce/phsosc.

S1: instab.mp4 shows the evolution of a radial wave when $d = 0$, $a = 0.2$ and $b = 2.0$.

S2: chimera.mp4 shows a chimera develop around the core of the annulus and then break off, drift to the outer radius and become the synchronous solution. $d = 0.75, a = 0.5, b = 2.0$.

S3: wanderchim.mp4 shows a chimera form at the core and breaking off before returning to the core and repeating the cycle. $d = 0.75, a = 0.5, b = 5.4$.

S4: transchim.mp4 shows a chimera develop around the core of the annulus and then break off, drift to the outer radius and become the synchronous solution. $d = 0.75, a = 0.5, b = 2.0$

S5: ap00.mp4, ap00d60l.mp4, ap00d75 show the behavior on the disk $0 \leq 5$ for $d = 0.35, 0.60, 0.75$.

S6: randics.mp4 shows the evolution of random initial conditions on the annulus, $2 \leq r \leq 5$.

S7: wave_phase.mp4 shows the evolution from random initial conditions to a rotating wave on the annulus. $K = 1, d = 0, a = 1, b = 5$.

S8: sync_phase.mp4 shows the evolution from random initial conditions to synchrony on the annulus. $K = 0.2, d = 0, a = 1, b = 5$.

S9: sync_pulse.mp4 shows the evolution from random initial conditions to synchrony on the annulus for pulse coupling. $K = 1, d = 0.4, a = 1, b = 5$.

S10: rantodeath.mp4, wavetodeath.mp4 shows the evolution from random initial conditions or perturbed straight armed rotating wave initial conditions to oscillator death on the annulus for pulse coupling. $K = 2, d = 0.4, a = 1, b = 5$.

S11: smoothpulse.mp4 shows the behavior on the annulus for smooth pulse coupling with odd PRC. $K = 1, d = 0, a = 1, b = 10$.

Bibliography

[1] Milton Abramowitz, Irene A Stegun, and Robert H Romer. Handbook of mathematical functions with formulas, graphs, and mathematical tables, 1988.

[2] Daniel M Abrams and Steven H Strogatz. Chimera states for coupled oscillators. *Physical review letters*, 93(17):174102, 2004.

[3] B Ambrosio and MA Aziz-Alaoui. Basin of attraction of solutions with pattern formation in slow–fast reaction–diffusion systems. *Acta biotheoretica*, 64(4):311–325, 2016.

[4] Joel T Ariaratnam and Steven H Strogatz. Phase diagram for the winfree model of coupled nonlinear oscillators. *Physical Review Letters*, 86(19):4278, 2001.

[5] Peter Ashwin, Stephen Coombes, and Rachel Nicks. Mathematical frameworks for oscillatory network dynamics in neuroscience. *The Journal of Mathematical Neuroscience*, 6(1):2, 2016.

[6] Martin Bataille-Gonzalez, Marcel G Clerc, and E Omel'chenko. Moving spiral wave chimeras. *Physical Review E*, 104(2):L022203, 2021.

[7] Christian Bick, Marc Goodfellow, Carlo R Laing, and Erik A Martens. Understanding the dynamics of biological and neural oscillator networks through exact mean-field reductions: a review. *The Journal of Mathematical Neuroscience*, 10(1):1–43, 2020.

[8] Jason J Bramburger. Rotating wave solutions to lattice dynamical systems i: the anti-continuum limit. *Journal of Dynamics and Differential Equations*, 31(1):469–498, 2019.

[9] Jason J Bramburger. Rotating wave solutions to lattice dynamical systems ii: Persistence results. *Journal of Dynamics and Differential Equations*, 31(1):499–536, 2019.

[10] Jason J. Bramburger. Stable periodic solutions to lambda-omega lattice dynamical systems. *Journal of Differential Equations*, 268(7):3201–3254, 2020.

[11] Shawn D Burton, G Bard Ermentrout, and Nathaniel N Urban. Intrinsic heterogeneity in oscillatory dynamics limits correlation-induced neural synchronization. *Journal of neurophysiology*, 108(8):2115–2133, 2012.

[12] Xinfu Chen and Bard Ermentrout. Traveling pulses in a nonlocal equation arising near a saddle-node infinite cycle bifurcation. *SIAM Journal on Applied Mathematics*, 77(4):1204–1229, 2017.

[13] Stephen Coombes. Waves, bumps, and patterns in neural field theories. *Biological cybernetics*, 93(2):91–108, 2005.

[14] Sharon M. Crook, G Bard Ermentrout, Michael C. Vanier, and James M. Bower. The role of axonal delay in the synchronization of networks of coupled cortical oscillators. *Journal of computational neuroscience*, 4(2):161–172, 1997.

[15] Lee DeVille and Bard Ermentrout. Phase-locked patterns of the kuramoto model on 3-regular graphs. *Chaos: An Interdisciplinary Journal of Nonlinear Science*, 26(9):094820, 2016.

[16] Yujie Ding and Bard Ermentrout. Rotating waves of nonlocally coupled oscillators on the annulus. *SIAM Journal on Applied Dynamical Systems*, 21(3):2047–2079, 2022.

[17] Vagner Dos Santos, Fernando S Borges, Kelly C Iarosz, Iberê L Caldas, Jose Danilo Szezech, Ricardo L Viana, Murilo S Baptista, and Antonio M Batista. Basin of attraction for chimera states in a network of rössler oscillators. *Chaos: An Interdisciplinary Journal of Nonlinear Science*, 30(8):083115, 2020.

[18] RO Dror, Carmen C Canavier, Robert J Butera, John W Clark, and John H Byrne. A mathematical criterion based on phase response curves for stability in a ring of coupled oscillators. *Biological cybernetics*, 80(1):11–23, 1999.

[19] Bard Ermentrout. A heuristic description of spiral wave instability in discrete media. *Physica D: Nonlinear Phenomena*, 82(1-2):154–164, 1995.

[20] Bard Ermentrout. *Simulating, Analyzing, and Animating Dynamical Systems*. Society for Industrial and Applied Mathematics, 2002.

[21] Bard Ermentrout, Youngmin Park, and Dan Wilson. Recent advances in coupled oscillator theory. *Philosophical Transactions of the Royal Society A*, 377(2160):20190092, 2019.

[22] Bard Ermentrout and David Terman. *The Mathematical Foundations of Neuroscience*, volume Vol. 35. 07 2010.

[23] G Bard Ermentrout. Stable periodic solutions to discrete and continuum arrays of weakly coupled nonlinear oscillators. *SIAM Journal on Applied Mathematics*, 52(6):1665–1687, 1992.

[24] G Bard Ermentrout and David Kleinfeld. Traveling electrical waves in cortex: insights from phase dynamics and speculation on a computational role. *Neuron*, 29(1):33–44, 2001.

[25] GB Ermentrout. Competition and cooperation in neural nets ed ma arbib and s amari, 1982.

[26] GB Ermentrout. The behavior of rings of coupled oscillators. *Journal of mathematical biology*, 23(1):55–74, 1985.

[27] GB Ermentrout and N Kopell. Oscillator death in systems of coupled neural oscillators. *SIAM Journal on Applied Mathematics*, 50(1):125–146, 1990.

[28] Xinling Geng and Jian-Young Wu. 'blue'voltage-sensitive dyes for studying spatiotemporal dynamics in the brain: visualizing cortical waves. *Neurophotonics*, 4(3):031207, 2017.

[29] Pranay Goel and Bard Ermentrout. Synchrony, stability, and firing patterns in pulse-coupled oscillators. *Physica D: Nonlinear Phenomena*, 163(3-4):191–216, 2002.

[30] John Guckenheimer. Isochrons and phaseless sets. *Journal of Mathematical Biology*, 1:259–273, 09 1975.

[31] Shuangjian Guo, Qionglin Dai, Hongyan Cheng, Haihong Li, Fagen Xie, and Junzhong Yang. Spiral wave chimera in two-dimensional nonlocally coupled fitzhugh–nagumo systems. *Chaos, Solitons & Fractals*, 114:394–399, 2018.

[32] Patrick S Hagan. Spiral waves in reaction-diffusion equations. *SIAM journal on applied mathematics*, 42(4):762–786, 1982.

[33] Milan Halgren, István Ulbert, Hélène Bastuji, Dániel Fabó, Lorand Erőss, Marc Rey, Orrin Devinsky, Werner K Doyle, Rachel Mak-McCully, Eric Halgren, et al. The generation and propagation of the human alpha rhythm. *Proceedings of the National Academy of Sciences*, 116(47):23772–23782, 2019.

[34] Cris R Hasan, Hinke M Osinga, Claire M Postlethwaite, and Alastair M Rucklidge. Numerical continuation of spiral waves in heteroclinic networks of cyclic dominance. *IMA Journal of Applied Mathematics*, 86(5):1141–1163, 2021.

[35] Stewart Heitmann and G Bard Ermentrout. Synchrony, waves and ripple in spatially coupled kuramoto oscillators with mexican hat connectivity. *Biological cybernetics*, 109(3):333–347, 2015.

[36] Xiaoying Huang, William C Troy, Qian Yang, Hongtao Ma, Carlo R Laing, Steven J Schiff, and Jian-Young Wu. Spiral waves in disinhibited mammalian neocortex. *Journal of Neuroscience*, 24(44):9897–9902, 2004.

[37] Xiaoying Huang, Weifeng Xu, Jianmin Liang, Kentaroh Takagaki, Xin Gao, and Jian-young Wu. Spiral wave dynamics in neocortex. *Neuron*, 68(5):978–990, 2010.

[38] Eugene M Izhikevich. Phase models with explicit time delays. *Physical Review E*, 58(1):905, 1998.

[39] Gabriela Jaramillo. Rotating waves in oscillatory media with nonlocal interactions and their normal form. *arXiv preprint arXiv:2103.14940*, 2021.

[40] Yoji Kawamura. Stable plane waves in nonlocally coupled phase oscillators. *AIP Advances*, 11(1):015304, 2021.

[41] James P Keener. *Principles of applied mathematics: transformation and approximation*. CRC Press, 2018.

[42] N Kopell and LN Howard. Target pattern and spiral solutions to reaction-diffusion equations with more than one space dimension. *Advances in Applied Mathematics*, 2(4):417–449, 1981.

[43] Y. Kuramoto. *Chemical Oscillations, Waves, and Turbulence*. Dover Books on Chemistry Series. Dover Publications, 2003.

[44] Carlo R Laing. Derivation of a neural field model from a network of theta neurons. *Physical Review E*, 90(1):010901, 2014.

[45] Carlo R Laing. Travelling waves in arrays of delay-coupled phase oscillators. *Chaos: An Interdisciplinary Journal of Nonlinear Science*, 26(9):094802, 2016.

[46] Carlo R. Laing. Chimeras in Two-Dimensional Domains: Heterogeneity and the Continuum Limit. *SIAM Journal on Applied Dynamical Systems*, 16(2):974–1014, January 2017.

[47] Carlo R Laing and William C Troy. Pde methods for nonlocal models. *SIAM Journal on Applied Dynamical Systems*, 2(3):487–516, 2003.

[48] Roland Lauter, Christian Brendel, Steven JM Habraken, and Florian Marquardt. Pattern phase diagram for two-dimensional arrays of coupled limit-cycle oscillators. *Physical Review E*, 92(1):012902, 2015.

[49] Iván León and Diego Pazó. Phase reduction beyond the first order: The case of the mean-field complex ginzburg-landau equation. *Physical Review E*, 100(1):012211, 2019.

[50] Tanushree B Luke, Ernest Barreto, and Paul So. Complete classification of the macroscopic behavior of a heterogeneous network of theta neurons. *Neural computation*, 25(12):3207–3234, 2013.

[51] Erik A Martens, Carlo R Laing, and Steven H Strogatz. Solvable model of spiral wave chimeras. *Physical review letters*, 104(4):044101, 2010.

[52] Lyle Muller, Frédéric Chavane, John Reynolds, and Terrence J Sejnowski. Cortical travelling waves: mechanisms and computational principles. *Nature Reviews Neuroscience*, 19(5):255–268, 2018.

[53] Lyle Muller, Giovanni Piantoni, Dominik Koller, Sydney S Cash, Eric Halgren, and Terrence J Sejnowski. Rotating waves during human sleep spindles organize global patterns of activity that repeat precisely through the night. *Elife*, 5:e17267, 2016.

[54] O E Omel'chenko. The mathematics behind chimera states. *Nonlinearity*, 31(5):R121–R164, May 2018.

[55] Joseph E Paullet and G Bard Ermentrout. Stable rotating waves in two-dimensional discrete active media. *SIAM Journal on Applied Mathematics*, 54(6):1720–1744, 1994.

[56] Joseph E Paullet and G Bard Ermentrout. Spiral waves in spatially discrete λ-ω systems. *International Journal of Bifurcation and Chaos*, 8(01):33–40, 1998.

[57] H Petsche, O Prohaska, P Rappelsberger, R Vollmer, and A Kaiser. Cortical seizure patterns in multidimensional view: the information content of equipotential maps. *Epilepsia*, 15(4):439–463, 1974.

[58] Liwei Ren and G Bard Ermentrout. Monotonicity of phaselocked solutions in chains and arrays of nearest-neighbor coupled oscillators. *SIAM journal on mathematical analysis*, 29(1):208–234, 1998.

[59] James A Roberts, Leonardo L Gollo, Romesh G Abeysuriya, Gloria Roberts, Philip B Mitchell, Mark W Woolrich, and Michael Breakspear. Metastable brain waves. *Nature communications*, 10(1):1–17, 2019.

[60] Michael E Rule, David Schnoerr, Matthias H Hennig, and Guido Sanguinetti. Neural field models for latent state inference: Application to large-scale neuronal recordings. *PLOS Computational Biology*, 15(11):e1007442, 2019.

[61] Michael E Rule, Carlos Vargas-Irwin, John P Donoghue, and Wilson Truccolo. Phase reorganization leads to transient β-lfp spatial wave patterns in motor cortex during steady-state movement preparation. *Journal of neurophysiology*, 119(6):2212–2228, 2018.

[62] Hidetsugu Sakaguchi, Shigeru Shinomoto, and Yoshiki Kuramoto. Mutual entrainment in oscillator lattices with nonvariational type interaction. *Progress of theoretical physics*, 79(5):1069–1079, 1988.

[63] Steven J Schiff, Xiaoying Huang, and Jian-Young Wu. Dynamical evolution of spatiotemporal patterns in mammalian middle cortex. *Physical review letters*, 98(17):178102, 2007.

[64] Nathan W Schultheiss, Astrid A Prinz, and Robert J Butera. *Phase response curves in neuroscience*. Springer, 2012.

[65] Michael A Schwemmer and Timothy J Lewis. The theory of weakly coupled oscillators. In *Phase response curves in neuroscience*, pages 3–31. Springer, 2012.

[66] Shin-ichiro Shima and Yoshiki Kuramoto. Rotating spiral waves with phase-randomized core in nonlocally coupled oscillators. *Physical Review E*, 69(3):036213, 2004.

[67] Rory G Townsend and Pulin Gong. Detection and analysis of spatiotemporal patterns in brain activity. *PLoS computational biology*, 14(12):e1006643, 2018.

[68] Rory G Townsend, Selina S Solomon, Spencer C Chen, Alexander NJ Pietersen, Paul R Martin, Samuel G Solomon, and Pulin Gong. Emergence of complex wave patterns in primate cerebral cortex. *Journal of Neuroscience*, 35(11):4657–4662, 2015.

[69] Daniel A Wiley, Steven H Strogatz, and Michelle Girvan. The size of the sync basin. *Chaos: An Interdisciplinary Journal of Nonlinear Science*, 16(1):015103, 2006.

[70] Dan Wilson and Bard Ermentrout. Augmented phase reduction of (not so) weakly perturbed coupled oscillators. *SIAM Review*, 61(2):277–315, 2019.

[71] Arthur T. Winfree. Biological rhythms and the behavior of populations of coupled oscillators. *Journal of Theoretical Biology*, 16(1):15–42, 1967.

[72] Matthias Wolfrum, Svetlana V Gurevich, and Oleh E Omel'chenko. Turbulence in the ott–antonsen equation for arrays of coupled phase oscillators. *Nonlinearity*, 29(2):257, 2016.

[73] Honghui Zhang, Andrew J Watrous, Ansh Patel, and Joshua Jacobs. Theta and alpha oscillations are traveling waves in the human neocortex. *Neuron*, 98(6):1269–1281, 2018.